A Thesis Submitted for the Degree of PhD at the University of Warwick

Permanent WRAP URL:

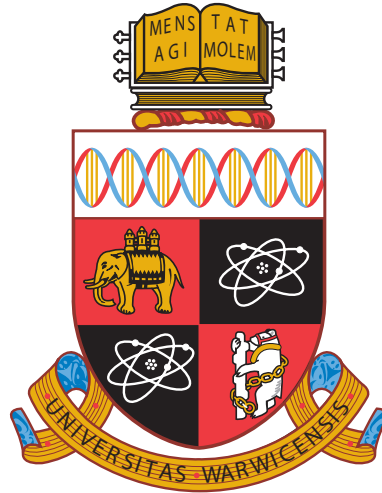http://wrap.warwick.ac.uk/185325

warwick.ac.uk/lib-publications

Electronic structure measurements of twisted graphene and 2D magnetic systems

by

James Edward Nunn

Thesis

Submitted to the University of Warwick

for the degree of

Doctor of Philosophy in Physics

Department of Physics

September 2023

THE UNIVERSITY OF
WARWICK

Contents

List of Tables

List of Figures

Acknowledgments

This thesis is the culmination of four years of work, and I owe a great deal of thanks to the many people who have had a hand in its completion. Firstly, I would like to thank my supervisors Neil Wilson and Cephise Cacho, who have both provided continued guidance and mentorship over the duration of my PhD – the success of which is a direct result of their support.

I'd also like to thank my colleagues at Diamond Light Source, especially Matthew Watson, who I have worked with closely over the past few years and hold in high regard. His advice concerning experiments, data analysis, academic writing and presentations has been invaluable, and helped me to become a better researcher and critical thinker.

Similarly, thank you to the members of the Microscopy group at Warwick, in particular, Abi Graham, who welcomed me to the group and accompanied me on many synchrotron trips, Xue Xia, who taught me the basics of sample fabrication, and Laxman Nagi-Reddy, who has helped me with many of my recent beamtimes.

Thank you also to my collaborators at the National Graphene Institute. Notable mentions to Astrid Weston for providing outstanding twisted graphene samples and Andrew McEllistrim for his hard work on the theory calculations. Additional thanks to Marcin Mucha-Kruczynski for the insightful discussions on moiré physics.

Finally, I'd like to give a huge thanks to the many friends I've made during the PhD, who have made the experience all that more enjoyable, my family, who continue to support my professional decisions even if they do not understand what it is I do, and my girlfriend Henrietta, who has supported me and helped keep me grounded during a time of considerable change and stress.

Declarations

I declare that this thesis contains an account of my research work carried out at the Department of Physics, University of Warwick, and Diamond Light Source, between October 2019 and September 2023 under the supervision of Professor Neil R. Wilson and Dr Cephise Cacho. The research reported here has not been previously submitted, wholly or in part, at this or any other academic institution for admission to a higher degree.

Parts of this thesis that have been published by the author between October 2019 and September 2023:

- Nunn, J. E., McEllistrim, A., Weston, A., Garcia-Ruiz, A., Watson, M. D., Mucha-Kruczynski, M., Cacho, C., Gorbachev, R. V., Fal'ko, V. I., Wilson, N. R. ARPES signatures of few-layer twistronic graphenes. *Nano Letters* **23**, 5201–5208 (2023).

Parts of this thesis in preparation to be submitted for publication:

- Nunn, J. Watson, M. D., Cacho, C., Nagi-Reddy, L., Wilson, N. R., *et al.* Electronic signatures of magnetic phase transitions in CrSBr.

All the work presented here was completed by myself, except for the following:

- Aligned and twisted graphene samples were fabricated by Astrid Weston as part of Roman Gorbachev's group at the National Graphene Institute, University of Manchester.

- µARPES data was acquired with the help of Matthew Watson at the I05 beamline of Diamond Light Source, with additional beamtime support from

Abigail Graham, Laxman Nagi-Reddy (University of Warwick), Amy Carl and Elisa Castanon (National Graphene Institute).

- Tight-binding/HkpTB calculations and ARPES simulations were performed by Andrew McEllistrim, with support from Aitor Garcia-Ruiz, as part of Vladimir Fal'ko's group at the National Graphene Institute, University of Manchester.

- LEED data was acquired by Brice Sarpi and Francesco Maccherozzi at the I06 beamline of Diamond Light Source.

- Gold-on-mica and gold-on-silicon templates were prepared by Laxman Nagi-Reddy at the University of Warwick.

- CrSBr band dispersions plotted in Fig. 5.9 were extracted by Cephise Cacho at Diamond Light Source.

Additional publications the author has contributed to but are not contained within this thesis:

- Graham, A. J., Park, H., Nguyen, P. V., Nunn, J. E., Kandyba, V., Cattelan, M., Giampietri, A., Barinov, A., Watanabe, K., Taniguchi, T., Andreev, A., Rudner, M., Xu, X., Wilson, N. R., Cobden, D. H. Revealing the conduction band and pseudovector potential in 2D moiré semiconductors. arXiv: 2309.10964 (2023) (submitted to Nature Materials).

- Gao, Y., Weston, A., Enaldiev, V., Castanon, E., Wang, W., Nunn, J. E., Carl, A., de Latour, H., Li, X., Summerfield, A., Kretinin, A., Clark, N., Wilson, N. R., Fal'ko, V. I., Gorbachev, R. V. Tunnel junctions based on interfacial 2D ferroelectrics. (2023) (submitted to Nature Communications).

Abbreviations

µARPES	Micro-angle-resolved photoemission spectroscopy
1D	One-dimensional
2D	Two-dimensional
3D	Three-dimensional
AFM	Atomic force microscopy
ARPES	Angle-resolved photoemission spectroscopy
BL	Bilayer
BZ	Brillouin zone
CBM	Conduction band minimum
CrSBr	Chromium sulphur bromide
EDC	Energy distribution curve
hBN	Hexagonal boron nitride
HkpTB	Hybrid $\mathbf{k}\cdot\mathbf{p}$-tight-binding
LEED	Low-energy electron diffraction
LEEM	Low-energy electron microscopy
LH	Linear horizontal
Linac	Linear accelerator
LV	Linear vertical
mBZ	Mini Brillouin zone

MDC	Momentum distribution curve
ML	Monolayer
OSA	Order-sorting aperture
PC	Polycarbonate
PDMS	Polydimethylsiloxane
PMMA	Polymethyl methacrylate
PVA	Polyvinyl alcohol
SPEM	Scanning photoemission microscopy
STM	Scanning tunnelling microscopy
STS	Scanning tunnelling spectroscopy
SWM	Slonczewski-Weiss-McClure
tBG	Twisted bilayer graphene
tDBG	Twisted double-bilayer graphene
TEM	Transmission electron microscopy
tMBG	Twisted monolayer-bilayer graphene
TMD	Transition metal dichalcogenide
UHV	Ultra-high vacuum
VBM	Valence band maximum

Abstract

The field of two-dimensional (2D) materials has grown significantly in recent years, motivated by the continued discovery of emergent phenomena and exotic phases in fabricated 2D homo- and heterostructures. This is particularly evident in correlated 2D systems such as the magic-angle twisted graphenes and 2D magnets. Many of the phenomena observed in these correlated materials are intimately tied to their electronic structures. Due to their complexity, simplified electronic structure models have been developed, whose predictions require testing against experimental results. In this thesis, we use angle-resolved photoemission spectroscopy (ARPES) with micrometre spatial resolution (µARPES) to directly visualise the electronic structure of twisted graphenes and 2D magnets and study their interlayer interactions, comparing measurements to theoretical predictions through both qualitative and quantitative analysis of spectral features.

Three twisted graphene systems are examined: twisted bilayer graphene (tBG), twisted monolayer-bilayer graphene (tMBG) and twisted double bilayer graphene (tDBG), allowing a systematic study of the electronic structure within these structures as a function of twist angle and number of layers. Results are compared to predictions from a hybrid $\mathbf{k}\cdot\mathbf{p}$-tight-binding (HkpTB) model, beginning with a qualitative comparison through simulation of the photoemission spectra, before extending this to a quantitative comparison of measured band parameters including hybridisation gap sizes and Dirac points shifts from an applied gate voltage. Good agreement with the HkpTB model is found across all stacking geometries for twist angles above $2°$, however, characterisation of a flat band observed in $1.5°$ tDBG highlights the need to include lattice relaxation effects in theoretical models of small twist angle systems.

Similarly, we study the model 2D magnetic system CrSBr using µARPES. By exfoliating flakes onto a fresh metal surface, low-temperature charging effects can be overcome, allowing ARPES measurements of bulk CrSBr in the antiferromagnetic phase. These are compared to measurements above the Néel temperature, revealing the effect that magnetic order has on the electronic structure. This technique could be readily applied to other semiconducting van der Waals magnetic materials, allowing measurement of their electronic structure at low-temperatures.

These results demonstrate the effectiveness of ARPES in studying complex 2D systems and how improvements in instrumentation and fabrication methods will allow for deeper comparison to theoretical predictions.

Chapter 1

Introduction

1.1   Introduction

Back in 2004, the experimental realisation of graphene revolutionised the fields of material science and condensed matter physics [1], offering the potential for a new age of nanoscale technologies and devices that could surpass that of the current silicon based frameworks [2]. Since then, despite a fairly lacklustre impact of graphene in modern industry, the discovery of stable monolayers has opened up an entire field of research dedicated to the study of two-dimensional (2D) materials that continues to grow each year [3]. Today, 2D van der Waals crystals cover the full range of material types, including metals, semimetals, semiconductors, insulators and superconductors [4, 5]. This large variety, coupled with their unique optical and transport properties, makes 2D materials well suited for use in many different electronic and optoelectronic applications [6].

The true potential for 2D materials, however, is in their ability to be combined into homo- and heterostructure stacks, enabling the design of atomically thin devices and the engineering of new material properties through interlayer interactions [7, 8]. On top of this, the weak van der Waals forces between layers means they can be stacked together with any arbitrary lateral rotation between them, known as twisting, which further influences the material properties. Together with the large family of van der Waals materials, this creates an almost endless phase space of different structure configurations to explore.

One particular system that has stood out among the rest in recent years is that of twisted bilayer graphene (tBG), primarily due to the reports in 2018 on magic-angle tBG. Graphene is semi-metallic in its monolayer and bilayer form, however, when two monolayers are stacked together with a twist angle close to $1.05°$,

known as the magic-angle, it exhibits highly correlated Mott-insulator and unconventional superconducting states [9, 10]. This ability to induce new electronic phases simply by introducing a twisted interface sparked a cascade of experimental and theoretical work into twisted graphene and other twisted 2D material systems [11], hoping to find further twist-dependent correlated phenomena.

Another system that has drawn much attention recently is that of the 2D magnets. In these materials, van der Waals layers display an in-plane long-range magnetic ordering that can persist down to the few-layer or even monolayer limit [12]. The ability to maintain an ordered magnetic state in an atomically thin layer opens up the prospects of manipulating the magnetism through applied fields and proximity effects. Additionally, integrating 2D magnets into heterostructures allows for the design of highly efficient spintronic and magneto-optical devices [13].

Future design of 2D devices, and the informed study of new 2D systems, relies on understanding the underlying physics within these materials, as well as the mechanisms with which they interact with neighbouring layers. This is aided by knowledge of the material's electronic structure, which can help explain intrinsic material properties, in addition to revealing quasiparticle interaction effects and interlayer hybridisation. In this thesis, electronic structure measurements of 2D systems will be the primary focus, aiming to highlight emergent interlayer phenomena in twisted graphene structures and exfoliated 2D magnets that can be compared to theoretical predictions.

1.2   Van der Waals materials

1.2.1   Graphene

Graphene is the single layer form of graphite and one of the first 2D materials to be studied as a monolayer [1]. It consists of carbon atoms arranged in a hexagonal lattice composed of two sublattice sites labelled A and B (Fig. 1.1(a)). Atoms are bonded to their nearest neighbours via three sp^2 hybridised orbitals, known as σ-bonds, with bond lengths, $a_0 \simeq 1.42$ Å [14]. The unit cell has lattice vectors, $\boldsymbol{a_1}$ and $\boldsymbol{a_2}$, described by

$$\boldsymbol{a_1} = \frac{a}{2}(\sqrt{3}, 1), \quad \boldsymbol{a_2} = \frac{a}{2}(\sqrt{3}, -1), \tag{1.2.1}$$

where $a = \sqrt{3}a_0 = |\boldsymbol{a_1}| = |\boldsymbol{a_2}| \simeq 2.46$ Å is the in-plane lattice constant [15]. In reciprocal space, graphene has a hexagonal Brillouin zone (BZ), shown in Fig. 1.1(b),
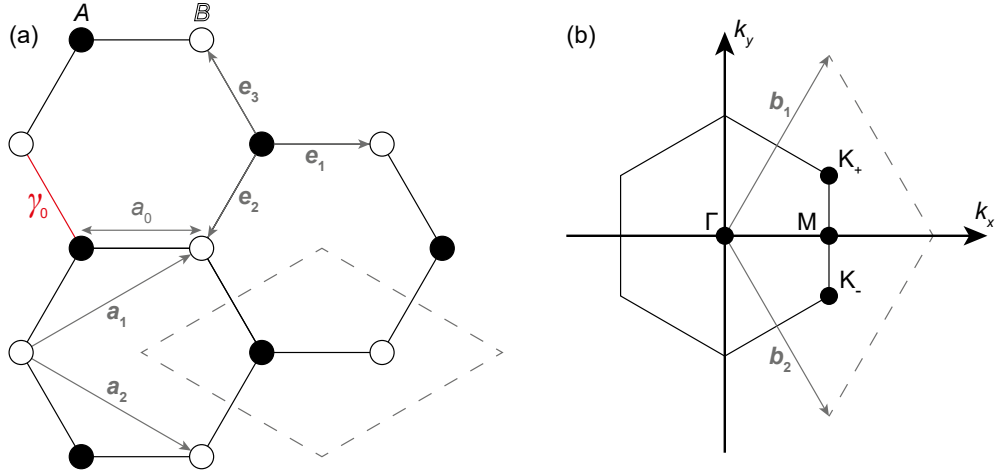
Figure 1.1: a) Crystal structure of graphene. Sublattice A and B sites are marked by filled and empty circles, respectively. Structure is labelled with bond length, a_0, lattice vectors, $\boldsymbol{a_1}$ and $\boldsymbol{a_2}$, nearest neighbour vectors, $\boldsymbol{e_1}$, $\boldsymbol{e_2}$ and $\boldsymbol{e_3}$, and nearest neighbour hopping parameter, γ_0. Dashed lines mark the unit cell. b) Brillouin zone of graphene, labelled with high symmetry points and reciprocal lattice vectors, $\boldsymbol{b_1}$ and $\boldsymbol{b_2}$.

with reciprocal lattice vectors, $\boldsymbol{b_1}$ and $\boldsymbol{b_2}$, given by

$$\boldsymbol{b_1} = \frac{2\pi}{\sqrt{3}a}(1, \sqrt{3}), \quad \boldsymbol{b_2} = \frac{2\pi}{\sqrt{3}a}(1, -\sqrt{3}), \tag{1.2.2}$$

with magnitude $|\boldsymbol{b_1}| = |\boldsymbol{b_2}| \simeq 2.95$ Å^{-1} [15]. The hexagonal BZ has high symmetry points, $\boldsymbol{\Gamma}$, at the centre of the BZ, $\mathbf{K}$, at the BZ corners, and $\mathbf{M}$, at the midpoint of the BZ edges. The $\mathbf{K}$ points, which are the primary area of focus in reciprocal space when studying graphene, have two inequivalent valleys labelled $\mathbf{K_+}$ and $\mathbf{K_-}$. Their positions in Fig. 1.1(b) are given by

$$\mathbf{K_+} = \frac{2\pi}{3a}(\sqrt{3}, 1), \quad \mathbf{K_-} = \frac{2\pi}{3a}(\sqrt{3}, -1), \tag{1.2.3}$$

with magnitude $|\mathbf{K_+}| = |\mathbf{K_-}| = |\mathbf{K}| \simeq 1.703$ Å^{-1} [14].

Of the four valence electrons available to each carbon atom in graphene, three occupy the in-plane σ-bonds, while the fourth occupies a p_z orbital extending out of the plane. These p_z orbitals bond covalently to form half-filled delocalised π-bonds. In addition to being the source of graphene's unique low-energy electronic structure, the π-bonds also enable the van der Waals forces holding layers together in graphite [14]. Note, electronic structure contributions from the graphene σ-bonds are also present [16], however, these occur at high binding energies and are not

relevant for understanding the data presented in this thesis.

The dispersion of the graphene π-bands can be calculated through a tight-binding approach. When considering only nearest neighbour hopping, the monolayer graphene Hamiltonian is expressed as

$$\mathcal{H}_{\mathrm{ML}} = \begin{pmatrix} \epsilon_A & -\gamma_0 f(\boldsymbol{k}) \\ -\gamma_0 f^*(\boldsymbol{k}) & \epsilon_B \end{pmatrix}, \tag{1.2.4}$$

where the diagonal terms, ϵ_A and ϵ_B, are the on-site energies for the A and B sites, respectively, and the off-diagonal terms describe hopping between the two sublattice sites [17]. Here, γ_0 is a coupling constant for hopping between nearest neighbours, while the function $f(\boldsymbol{k})$ is given by

$$f(\boldsymbol{k}) = \sum_{j=1}^{3} \mathrm{e}^{i\boldsymbol{k}\cdot\boldsymbol{e_j}} = \mathrm{e}^{ik_x a/\sqrt{3}} + 2\mathrm{e}^{-ik_x a/(2\sqrt{3})} \cos{(k_y a/2)}, \tag{1.2.5}$$

where $\boldsymbol{k} = (k_x, k_y)$ is the in-plane wave vector and $\boldsymbol{e_j}$ are the nearest neighbour vectors (Fig. 1.1(a)) [15]. The energy dispersion, $E_{\mathrm{ML}}(\boldsymbol{k})$, is related to the Hamiltonian by the Schrodinger equation, $\mathcal{H}_{\mathrm{ML}}\Psi = E_{\mathrm{ML}}(\boldsymbol{k})\Psi$, where Ψ is the graphene wavefunction. The dispersion of graphene can thus be determined by solving

$$|\mathcal{H}_{\mathrm{ML}} - E_{\mathrm{ML}}| = 0. \tag{1.2.6}$$

For intrinsic graphene, $\epsilon_A = \epsilon_B = 0$, and so Eq. (1.2.6) returns the result

$$E_{\mathrm{ML}} = \pm\gamma_0|f(\boldsymbol{k})|. \tag{1.2.7}$$

The dispersion of the graphene π-band is plotted in Fig. 1.2(a). Note, in this plot, next-nearest neighbour hopping has also been including, which results in electron-hole asymmetry at large energies [18]. For low energies, the next-nearest neighbour hopping strength is negligible and the dispersion is well described by Eq. (1.2.7). $f(\boldsymbol{k})$ is zero at $\boldsymbol{k} = \mathbf{K}$, where the solutions to Eq. (1.2.7) are degenerate. This is known as the Dirac point and marks a zero band gap contact point between the valence and conduction bands [17]. Eq. (1.2.7) can be simplified further by expanding $f(\boldsymbol{k})$ close to the $\mathbf{K}$ points through the substitution $\boldsymbol{k} = \mathbf{K}_\xi + \boldsymbol{\kappa}$, where $\xi = \pm 1$ is the valley index, and $\boldsymbol{\kappa} \ll \mathbf{K}_\xi$ [18]. Following the expressions for $\mathbf{K}_\xi$ in

4
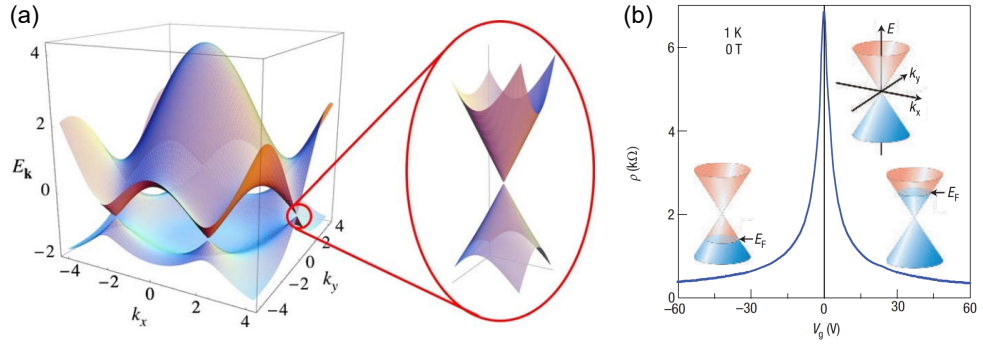
Figure 1.2: a) The dispersion of the graphene π-band, taken from [18]. b) The field effect in graphene, taken from [2]. An applied gate voltage results in a rapid decrease in resistivity due to a change in the Fermi energy (insets).

Eq. (1.2.3), this leads to the approximation

$$f(\boldsymbol{k}) \approx -\frac{\sqrt{3}}{2}a\left[\left(\frac{\sqrt{3}}{2}+\frac{1}{2}\mathrm{i}\right)\kappa_x - \xi\left(\frac{1}{2}-\frac{\sqrt{3}}{2}\mathrm{i}\right)\kappa_y\right], \qquad (1.2.8)$$

where $|\boldsymbol{\kappa}| = \sqrt{\kappa_x^2 + \kappa_y^2}$. Substituting Eq. (1.2.8) into Eq. (1.2.7) gives the simple result

$$E_{\mathrm{ML}} = \pm\hbar v|\boldsymbol{\kappa}|, \qquad (1.2.9)$$

where $v = \frac{\sqrt{3}a\gamma_0}{2\hbar}$ is the band velocity [17]. Eq. (1.2.9) demonstrates a linear conical dispersion centred on the $\mathbf{K}$ points of graphene, as illustrated by the magnification in Fig. 1.2(a). Interestingly, the linear nature of this dispersion implies electrons close to the Dirac point behave as massless Dirac fermions with an effective velocity given by $v = v_{\mathrm{F}}$, where v_{F} is the Fermi velocity [19]. This is where the Dirac point gets its name and, similarly, is why the linear dispersion around the $\mathbf{K}$ points is nicknamed the Dirac cone. This behaviour ultimately results in exceedingly high carrier mobilities in graphene and allows the carrier concentration to be easily tuned between electrons and holes by applying a back gate voltage (Fig. 1.2(b)) [2, 20].

For future reference, the density of states per unit cell, ρ_{ML}, can be approximated close to the Dirac point using Eq. (1.2.9). This gives the result

$$\rho_{\mathrm{ML}} = \frac{2|E_{\mathrm{ML}}|}{\pi v_{\mathrm{F}}^2}. \qquad (1.2.10)$$

which reveals a linear energy dependence on the density of states close to the $\mathbf{K}$ points. Note, some descriptions of ρ in the literature include a factor of $1/4$ to give the density of states per spin and per valley [18]. Finally, we mention that expansion

5

of $f(\boldsymbol{k})$ around the **K** points when including next-nearest neighbour hopping results in a three-fold symmetric equation for E_{ML}. Known as trigonal warping, this causes a distortion of the standard linear Dirac cone and becomes pronounced at high binding energies [18].

Bilayer graphene

For the results presented in Chapters 3 and 4, it can be useful to also be familiar with the structural and electronic properties of bilayer graphene, and how these differ from the monolayer case. Graphite naturally forms as Bernal- or AB-stacked layers and exfoliated graphene bilayers maintain this stacking arrangement. This crystal structure is illustrated in Fig. 1.3(a), where A_1 atoms from the top layer are vertically aligned with B_2 atoms in the bottom layer, known as dimer sites. Meanwhile, B_1 and A_2 atoms from the top and bottom layers, respectively, are aligned with the centres of the honeycombs in the opposing layer, known as non-dimer sites [17]. This results in several different electronic environments for the different sublattice sites. Adopting the convention used for graphite, interlayer coupling between different atoms from the top and bottom layers can be described by the Slonczewski-Weiss-McClure (SWM) parameters, γ_1, γ_3 and γ_4 [21–23]. Explicitly, γ_1 couples A_1 and B_2 sites, γ_3 couples B_1 and A_2 sites, and γ_4 couples A_1 (B_1) and A_2 (B_2) sites, where the relative strength follows $\gamma_1 > \gamma_3 > \gamma_4$. Note, in thicker graphitic systems, γ_2 and γ_5 terms are also included to describe next-nearest layer coupling [24].

In much the same way as monolayer graphene, the bilayer electronic structure can be described using a tight-binding model [17]. The corresponding bilayer Hamiltonian has the form

$$
\mathcal{H}_{\mathrm{BL}} = \begin{pmatrix}
\epsilon_{A1} & -\gamma_0 f(\boldsymbol{k}) & \gamma_4 f(\boldsymbol{k}) & -\gamma_3 f^*(\boldsymbol{k}) \\
-\gamma_0 f^*(\boldsymbol{k}) & \epsilon_{B1} & \gamma_1 & \gamma_4 f(\boldsymbol{k}) \\
\gamma_4 f^*(\boldsymbol{k}) & \gamma_1 & \epsilon_{A2} & -\gamma_0 f(\boldsymbol{k}) \\
-\gamma_3 f(\boldsymbol{k}) & \gamma_4 f^*(\boldsymbol{k}) & -\gamma_0 f^*(\boldsymbol{k}) & \epsilon_{B2}
\end{pmatrix}. \tag{1.2.11}
$$

The upper-left and lower-right 2×2 blocks in $\mathcal{H}_{\mathrm{BL}}$ resemble that of the monolayer graphene Hamiltonian and describe intralayer coupling within each layer, while the upper-right and lower-left blocks describe interlayer coupling. A simple analytical solution to $\mathcal{H}_{\mathrm{BL}}$ can be found again by setting the on-site energies to zero and approximating $f(\boldsymbol{k})$ close to the **K** points, in addition to neglecting γ_3 and γ_4 terms
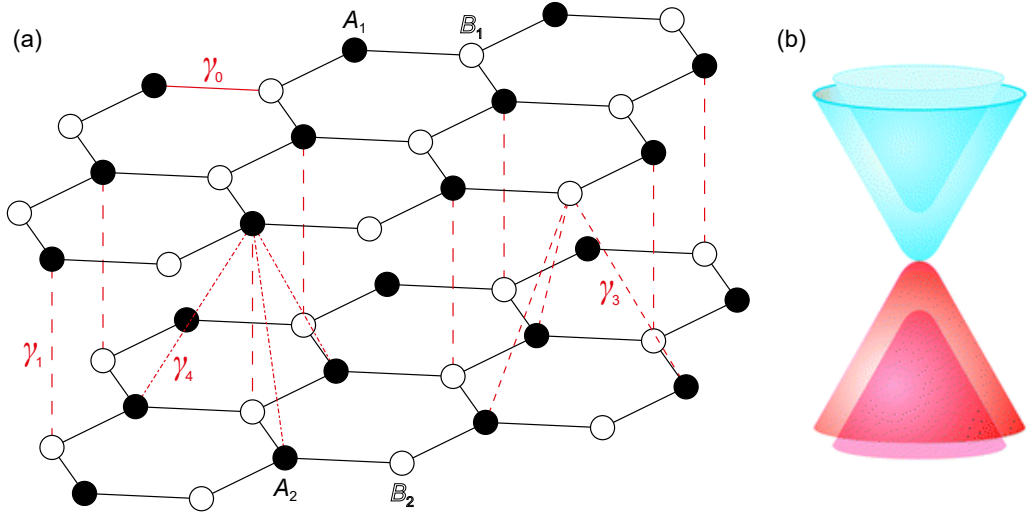
Figure 1.3: a) Crystal structure of AB-stacked bilayer graphene. Structure is labelled with intralayer coupling parameter, γ_0, and interlayer parameters, γ_1, γ_3 and γ_4. b) Schematic of the low-energy valence (red) and conduction (blue) bands centred on the **K** points of bilayer graphene, taken from [25].

in the low-energy limit [17]. This returns the result

$$E_{\text{BL},\beta} \approx \pm \frac{1}{2}\gamma_1 \left[\sqrt{1 + 4\frac{v^2|\boldsymbol{\kappa}|^2}{\gamma_1^2}} + (-1)^\beta \right], \qquad (1.2.12)$$

where $\beta = 1, 2$. Eq. (1.2.12) describes four bands: $\pm$ differentiates between conduction and valence bands, $\beta = 1$ describes low-energy bands that are degenerate at **K**, and $\beta = 2$ describes split bands with energy $|E_{\text{BL},2}| \geq |\gamma_1|$ [26]. These are shown schematically in Fig. 1.3(b) and switch between an approximately linear dispersion for large $\boldsymbol{\kappa}$ and a quadratic dispersion at small $\boldsymbol{\kappa}$. At low-energies in the $\beta = 1$ band, the density of states can be approximated as

$$\rho_{\text{BL}} = \frac{\gamma_1}{\pi v^2}, \qquad (1.2.13)$$

which is a constant [17].

In general, however, the on-site energies in bilayer graphene are finite and non-equivalent, resulting in subtle changes in the low-energy electronic structure. Differences between these can be described by three parameters:

$$U = \frac{1}{2}[(\epsilon_{A1} + \epsilon_{B1}) - (\epsilon_{A2} + \epsilon_{B2})], \qquad (1.2.14)$$
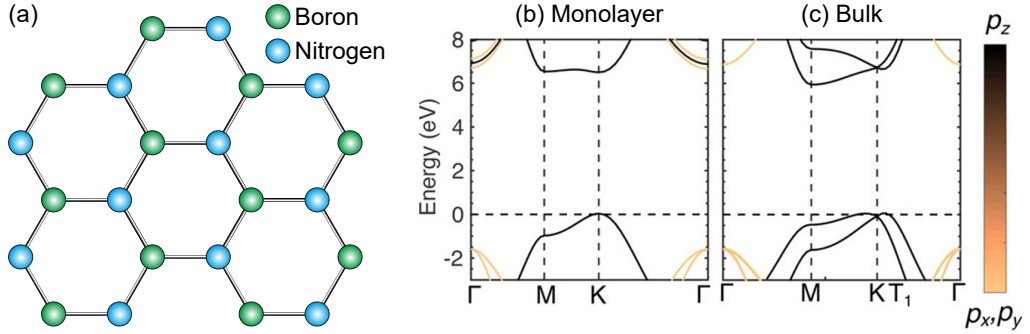
Figure 1.4: a) 2D Crystal structure of hBN. b,c) Calculated band structure of (b) monolayer and (c) bulk hBN, adapted from [33].

$$\Delta' = \frac{1}{2}[(\epsilon_{B1} + \epsilon_{A2}) - (\epsilon_{A1} + \epsilon_{B2})], \tag{1.2.15}$$

$$\delta_{AB} = \frac{1}{2}[(\epsilon_{A1} + \epsilon_{A2}) - (\epsilon_{B1} + \epsilon_{B2})], \tag{1.2.16}$$

where U describes an interlayer energy difference between the two layers, Δ' describes an energy difference between dimer and non-dimer sites, and δ_{AB} describes an intralayer energy difference on each layer. Δ' has the effect of adding electron-hole asymmetry into the system, while U and δ_{AB} open a band gap between the conduction and valence bands [17]. Experimentally, it has been shown that the interlayer asymmetry described by U can be induced by surface doping and the use of external gates [27, 28].

1.2.2 Hexagonal boron nitride

Another important member of the van der Waals materials family is hexagonal boron nitride (hBN). Structurally similar to graphene, hBN forms the same 2D crystal lattice, but with the A and B carbon sites now replaced by boron and nitrogen atoms (Fig. 1.4(a)). Additionally, the in-plane lattice parameter, $a_{\mathrm{hBN}} = 2.50$ Å, is slightly larger than in graphene [29]. The main difference between hBN and graphene, however, is in their electronic structure. hBN is a wide band gap semiconductor with a band gap on the order of $\sim$6 eV [30], that undergoes an indirect to direct transition in the monolayer limit (Figs. 1.4(b) and (c)) [31, 32].

hBN's large band gap, as well as dielectric properties similar to that of SiO_2 ($\varepsilon_{\mathrm{hBN}} \approx 4$; $V_{\mathrm{breakdown}} \approx 0.7$ V nm^{-1}), make it suitable for use as a tunnel barrier or dielectric in field effect devices [34, 35]. Furthermore, the atomically flat nature of hBN makes it an ideal substrate for other 2D materials, with minimal hybridisation to neighbouring layers due to the large energy separation in reciprocal space. It

has been shown that stacking graphene on hBN increases its carrier mobilities by an order of magnitude compared to graphene placed on oxide substrates [34]. This can be increased even further by encapsulating the graphene with another flake of hBN, which protects the graphene from surface impurities, as well as enabling a self-cleansing process that collects contamination into large pockets, allowing the remaining interface areas to be atomically clean [36].

1.2.3   2D magnets

A recent addition to the family of 2D materials is that of the van der Waals magnets – layered materials that possess a magnetic ground state in the few-layer limit [12, 13, 37, 38]. The Mermin-Wagner theorem states that thermal fluctuations should destroy long-range magnetic order in a truly isotropic 2D system [39]. In the case of the van der Waals magnets, this is overcome through magnetocrystalline anisotropies that allow the transition to an ordered magnetic state at finite temperature. Magnetic phases have been observed experimentally in a number of 2D crystals such as bilayer $CrGeTe_3$ [40] and monolayer CrI_3 [41], $CrBr_3$ [42], Fe_3GeTe_3 [43] and $FePS_3$ [44]. In many cases, the ordering temperature, as well as the exact magnetic phase, changes with the number of layers, allowing the magnetic properties to be tuned with thickness [40, 41, 45]. In addition, it has been shown that these properties can be further tuned through electrostatic gating [46, 47], in some cases, even able to shift the transition temperature above 300 K [48]. This tunability demonstrates the functionality of 2D magnetic materials and their potential for being incorporated into devices [12, 38]. This is not without restrictions, however, as the majority of 2D magnets display poor air stability and degrade when exposed to light [49, 50], making the design and fabrication of structures comprising van der Waals magnets nontrivial.

Chromium sulphur bromide

In the past few years, the van der Waals material chromium sulphur bromide (CrSBr) has emerged as an exciting addition to the 2D magnetic family. It shows significantly improved stability compared to other 2D magnets (initially thought to be entirely air stable) allowing it to be studied more easily [51]. Particular highlights in the reported properties of CrSBr include anisotropic transport [52, 53], a large negative magnetoresistance [54, 55], and strong magneto-optical [56, 57] and exciton-magnon coupling [58]. Furthermore, its semiconducting properties and expected high carrier mobility make CrSBr an ideal candidate for spintronic and
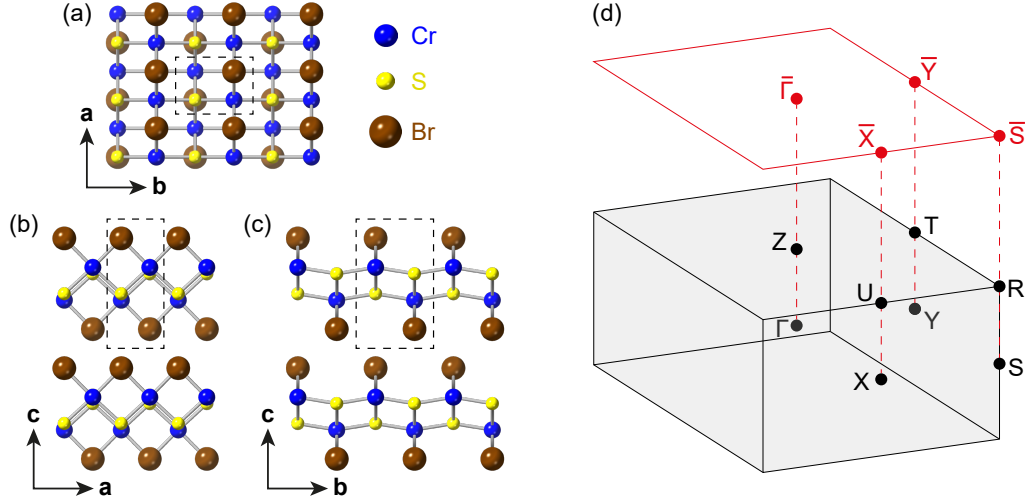
Figure 1.5: a–c) Crystal structure of CrSBr as viewed along the (a) *c*-axis, (b) *b*-axis and (c) *a*-axis. Dashed lines mark the unit cell. b) Bulk (black) and surface (red) Brillouin zones of CrSBr, with labelled high symmetry points.

magneto-optoelectronic applications [59].

In the bulk, CrSBr is an A-type antiferromagnet with a Néel temperature of $T_N = 132$ K [54]. It forms as van der Waals layers stacked along the *c*-axis, where each layer consists of buckled planes of Cr and S atoms sandwiched between sheets of Br (Fig. 1.5(a)–(c)). It is described by a simple orthorhombic unit cell with the P_{mmn} space group and lattice constants $a = 3.50$ Å, $b = 4.76$ Å and $c = 7.96$ Å [60]. Subsequently, the BZ of CrSBr is similarly simple, characterised by a rectangular in-plane BZ (Fig. 1.5(d)).

In the magnetic phase, spins on the Cr sites align along the *b*-axis, corresponding to the magnetic easy axis, and form a ferromagnetic layer [61]. When below T_N, these layers couple antiferromagnetically, giving the observed antiferromagnetic behaviour in bulk CrSBr. The antiferromagnetic transition temperature of CrSBr increases for decreasing number of layers, before becoming ferromagnetic in the monolayer limit with a Curie temperature of $T_C \sim 150$ K [45]. Above T_N, CrSBr has been shown to initially enter an intermediate ferromagnetic phase, where long-range order between layers has been lost, but intralayer ferromagnetic order persists (Fig. 1.6) [62]. This continues up to a temperature T_{intra}, where eventually long-range order within each layer is also lost. Measurements have found $T_{intra} \simeq 156$ K, which is in line with the expected Curie temperature of monolayer CrSBr. Above T_{intra}, it is thought that short-range order survives until reaching a temperature $T^* \simeq 185$ K, where CrSBr enters a truly paramagnetic phase [62].
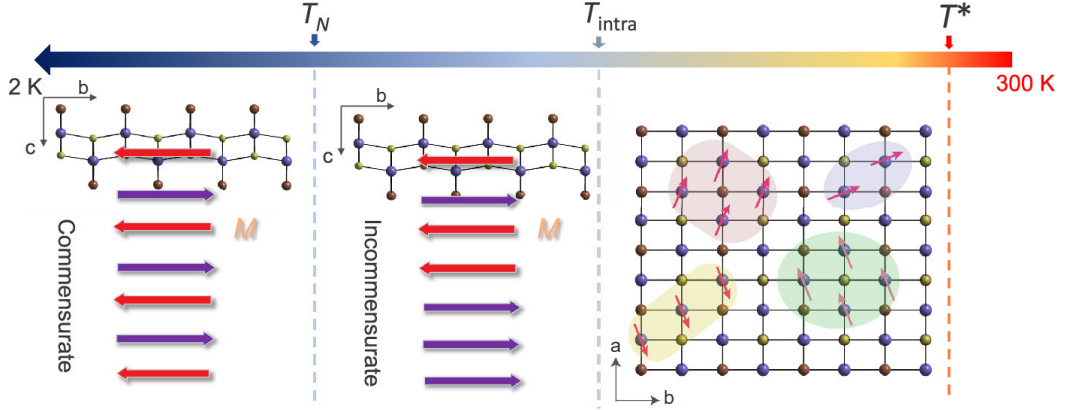
Figure 1.6: Schematics of the different magnetic phases of CrSBr as a function of temperature, taken from [62].

An interesting question concerning these reports is how the electronic structure of CrSBr changes across the different magnetic phases? A recent study by Bianchi *et al.* aimed to provide insight through detailed band structure calculations of CrSBr [63]. They used a quasiparticle self-consistent GW method which takes into account Coulomb interactions and is self-consistent in both self-energy and charge density through an iterative process, allowing much greater accuracy compared to standard density functional theory methods. Figs. 1.7(a) and (b) show their calculations for bulk CrSBr in an antiferromagnetic and ferromagnetic phase, respectively, for different magnetic easy axis. Within each phase, changing of the easy axis has only minor effect on the electronic structure, however, switching the interlayer magnetic coupling from antiferromagnetic to ferromagnetic significantly modifies the valence band structure. This is most clearly seen for the low-energy valence bands around $\mathbf{\Gamma}$, which are shifted up in the ferromagnetic case, resulting in a reduced band gap. Additionally, various split bands appear in the ferromagnetic case due to a lifting of the degeneracy of the antiferromagnetic bands from the broken inversion symmetry [63]. For the intermediate ferromagnetic phase described previously, the electronic structure can be expected to lie somewhere between the two paradigms in Figs. 1.7(a) and (b).

Fig. 1.7(c) shows the electronic structure calculation performed by Bianchi *et al.* for a paramagnetic approximation. Here, they have considered a $2 \times 2 \times 2$ supercell with spins frozen in a quasi-random configuration [63]. Note, due to the supercell, the high symmetry points correspond to a reduced BZ with a band structure that is folded compared to those shown in Figs. 1.7(a) and (b). The paramagnetic structure shows many bands closely spaced in energy, which is a result of the frozen

11
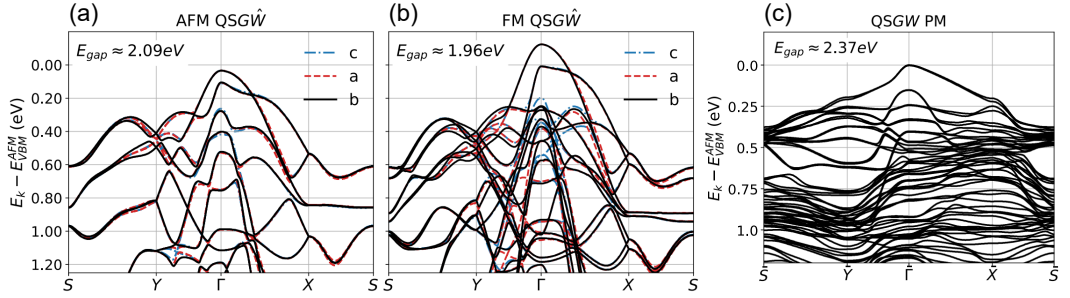
Figure 1.7: a,b) Electronic structure calculations of CrSBr for different magnetic easy axis when in an (a) antiferromagnetic and (b) ferromagnetic phase. c) Paramagnetic approximation of the electronic structure of CrSBr. Figures taken from [63].

spin disorder. Experimentally, one can expect this to manifest as a broadening of the electronic states due to dynamic spin fluctuations, similar to that observed in $CrGeTe_3$ [64].

1.3 Combining 2D layers

One of the greatest benefits of 2D materials is their ability to be easily stacked together into homo- and heterostructures without boundary defects that occur in many three-dimensional (3D) systems [7, 8]. This is enabled through the layered nature of 2D crystals, where strong covalent bonds provide in-plane stability, while out-of-plane van der Waals forces allow universal bonding to other 2D layers. In addition to allowing the creation of fully 2D devices through stacking of 2D materials with different functionalities [65], interaction effects at 2D interfaces can modulate the underlying properties of the parent materials [10, 66, 67], providing a route to engineer materials for different purposes.

Being able to achieve high performance 2D devices and pronounced interlayer interaction effects is dependent on two main factors: high purity 2D materials and clean interfaces. Focusing initially on the first of these, the most successful way of producing high quality mono or few-layer flakes is by exfoliating them from low-impurity bulk single crystals. The van der Waals forces holding layers together can be easily broken by mechanical cleavage or exfoliation. Researchers use specialist tapes to thin down bulk crystals before pressing them onto a substrate (usually SiO_2) and peeling the tape away, leaving the substrate covered with 2D flakes of various thicknesses. Typically this method results in numerous few-layer or thinner flakes with lateral sizes on the order of 10s of micrometres wide. This places a natural limit on the size of structure that can be fabricated from these flakes, but

offers a high quality of material that is dependent solely on the parent crystal.

Once exfoliated, 2D flakes can be stacked into homo- and heterostructures using a variety of transfer methods [68], with the most popular of these involving the use of polymer stamps [69]. These utilise competing adhesive forces between polymer membranes and 2D flakes to pickup and stack layers together. Two common transfer techniques will be discussed further in Section 2.3.1. Despite the success these methods have had, the resulting structures can suffer from polymer residue contamination. Besides, exfoliated flakes, produced either in air or a controlled atmospheric environment such as a glove box, still experience surface contamination, namely in the form of hydrocarbons [70]. Contamination on and between layers greatly reduces the contact area and hence performance of 2D stacks and devices. Fortunately, a self-cleansing process aids in accumulating contamination into bubbles, increasing the contact area [36, 70]. This can be improved further through annealing, increasing the mobility of contaminants and allowing them to collect into larger bubbles [71], as well as manually pushing bubbles using surface probe tips to create areas with large clean interfaces [72].

Though 2D stacks made from exfoliated flakes can achieve a high quality, their fabrication process is notoriously slow and limited to lateral sizes < 100 µm. Efforts are being made to develop growth methods to fabricate van der Waals homo- and heterostructures on much larger scales, using techniques such as physical or chemical vapour deposition [73, 74] and molecular beam epitaxy [75, 76]. Historically, epitaxial growth of 2D materials on substrates has suffered from increased defects and grain boundaries compared to exfoliated flakes, leading to reduced device performance. Recent advancements, however, have allowed for the single crystal growth of 2D monolayers with domain sizes larger than a millimetre [77, 78]. This opens the door to the large area growth of van der Waals stacks [79], though further work is required to fully understand their growth mechanisms [80].

As mentioned before, 2D devices can be designed through combining of different 2D materials into heterostructures. hBN is often used as a substrate for improved transport properties, seen in graphene and semiconducting 2D materials such as the transition metal dichalcogenides (TMDs) [81]. Encapsulation with hBN improves this further and protects the underlying 2D layer from contamination, particularly useful for air sensitive materials [82]. Graphene is commonly used as an electrical contact in 2D devices as it offers lower contact resistance compared to standard 3D metal contacts [83]. When combined with hBN as a dielectric, it can additionally act as an electrostatic gate, discussed further in Section 2.3.2. Combining these with other functional 2D layers allows the design of a number of 2D devices,
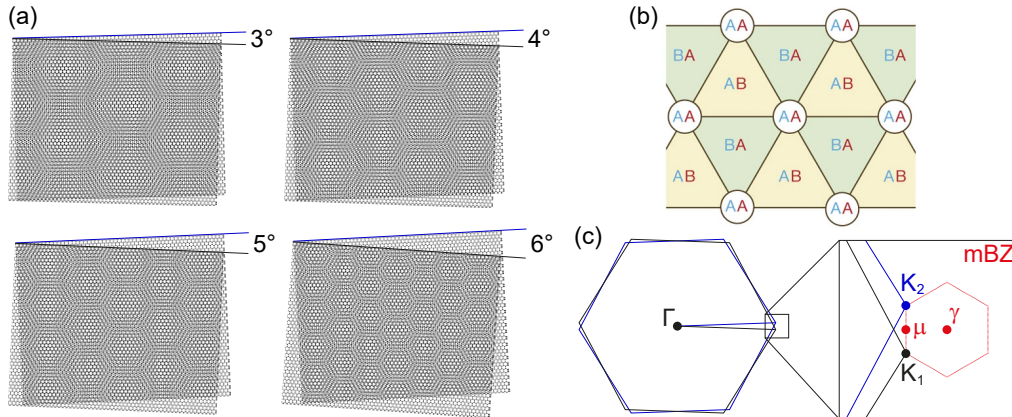
Figure 1.8: a) Moiré patterns formed from twisting two identical 2D hexagonal lattices for different twist angles. b) Simplified schematic of the different stacking domains in moiré patterns, taken from [9]. c) Formation of a mini Brillouin zone at the corners of two identical twisted hexagonal Brillouin zones. $\mathbf{K_1}$ belongs to the top BZ (black) and $\mathbf{K_2}$ to the bottom BZ (blue).

such as atomically thin p–n junctions [84], light emitting diodes [85] and field-effect transistors [86]. The discovery of 2D magnets also brings with it the possibility of 2D spintronic devices such as magnetic tunnel junctions and spin-filters [87, 88], as well as enabling magnetic proximity effects in non-magnetic 2D layers [89, 90].

1.3.1 Twistronics

When stacking together 2D materials, the layers are not limited to specific lateral alignments related to lattice configuration. Instead, the weak van der Waals forces allow layers to be stacked with an arbitrary rotation or 'twist' between them. This rotational degree of freedom is known as the twist angle and adds yet another tuning parameter in the fabrication of 2D homo and heterostructures. It turns out that twisting can have a profound effect on the properties of 2D materials through modulation of the interlayer coupling strength, which changes as a function of twist angle [9, 10, 91–93]. This has led to a whole new field of study, known as twistronics, specifically looking at twisted phenomena in 2D materials. For the most part, twistronics has focused on stacks of 2D hexagonal lattices, as they are the most abundant type in the family of van der Waals materials, and their physics can be readily understood. As such, information presented here will apply primarily to hexagonal 2D materials, which is directly relevant to the results in Chapters 3 and 4.

The most universal feature in twisted stacks of 2D materials is the creation

of a moiré superlattice pattern in the crystal lattice. This occurs for twisted layers of the same material, e.g. twisted graphene, or twisted layers with small lattice mismatch, e.g. hBN/graphene or TMD/TMD heterobilayers. The moiré pattern introduces a new long range periodicity, whose period, λ_m, varies with twist angle according to

$$\lambda_\mathrm{m} = \frac{(1+\chi)a_1}{\sqrt{2(1+\chi)(1-\cos\theta)+\chi^2}}, \qquad (1.3.1)$$

where $\chi = \frac{a_2-a_1}{a_1}$ is the lattice mismatch between the two twisted layers, a_1 and a_2 are the lattice parameters of the two layers such that $a_2 \geq a_1$, and θ is the twist angle [67]. Note, Eq. (1.3.1) shows that there is still a finite moiré periodicity at zero twist angle for layers with a small lattice mismatch. The moiré pattern formed from two twisted layers of graphene can be seen in Fig. 1.8(a), where the periodicity increases with decreasing twist angle, and can be orders of magnitude larger than that of the individual layers at small twist angles. This pattern can be described by a triangular lattice of approximately AA-stacked domains, where the atoms from each layer are stacked on top of each other, and alternating AB- and BA-like domains at the triangle centres, connected by intermediate stacking arrangements (Fig. 1.8(b)). These domains become increasingly large as the twist angle is decreased, allowing them to be imaged using surface probe techniques such as scanning tunnelling microscopy (STM) [94] and piezoresponse force microscopy [95], providing a visualisation of the moiré pattern. Furthermore, at small twist angles, lattice reconstructions maximise the area of the energetically favourable AB and BA regions by atomic displacements, altering the domain sizes further [96]. The degree of reconstruction and the range of twist angles at which they become relevant is of great interest, as reconstructions have been shown to cause important modifications to the electronic structure of twisted systems [97]

In reciprocal space, the moiré periodicity is characterised by the formation of a moiré or mini Brillouin zone (mBZ), illustrated in Fig. 1.8(c). The mBZ shares corners with the BZ of the two twisted layers, referred to as the primary BZs. Consequently, the size of the mBZ is dependent on the separation of the primary $\mathbf{K}$ points and, hence, twist angle. Similar to the primary BZs, the mBZ has reciprocal lattice vectors, $\mathbf{G_m} = \mathbf{G_1} - \mathbf{G_2}$, where $\mathbf{G_1}$ and $\mathbf{G_2}$ are the reciprocal lattice vectors of the of the top and bottom twisted layers, respectively, and has magnitude given by

$$|\mathbf{G_m}| = \frac{4\pi}{\sqrt{3}\lambda_\mathrm{m}}. \qquad (1.3.2)$$

In the electronic structure, hybridisation between twisted layers results in
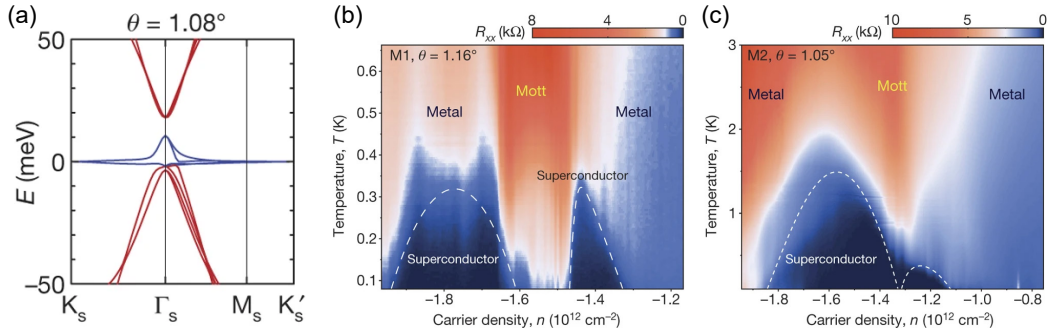
Figure 1.9: a) Calculated low-energy electronic structure of magic-angle tBG, with the flat bands shown in blue, taken from [9]. b,c) Temperature vs carrier density phase diagram of tBG at the twist angles (b) 1.16° and (c) 1.05°, taken from [10].

the opening of energy gaps where primary bands belonging to different layers cross in reciprocal space. Likewise, scattering of the primary bands by $\mathbf{G_m}$ results in the appearance of replica bands that also hybridise with the primary bands. This was originally observed in twisted heterostructures of graphene on hBN, giving rise to van Hove singularities in the density of states and superlattice Dirac points [67, 98]. Furthermore, the energy position of these hybridisation gaps change with twist angle, allowing them to be tuned closer to the Fermi level [99]. For twisted bilayer graphene (tBG), Bistritzer and MacDonald demonstrated theoretically that this hybridisation results in a reduction of the Dirac point band velocity, which reduces to zero for specific twist angles known as magic-angles. This signifies the formation of a highly non-dispersive flat band at the Fermi level (Fig. 1.9(a)), with the largest magic angle being only 1.05° [100]. In 2018, the existence of these flat bands in magic-angle tBG was experimentally realised and shown to host Mott-like insulator and superconducting states [9, 10], accessible through electrostatic doping (Figs. 1.9(b) and (c)). These arise due to the localisation of electrons in the moiré lattice, leading to strong correlation effects. This simple ability to change bilayer graphene, a semi-metal, into a superconductor or Mott insulator sparked a wave of experimental and theoretical research hoping to observe similar effects in other systems.

In addition to tBG, other twisted graphitic systems have been shown to possess correlated phases, such as in twisted monolayer-bilayer graphene (tMBG) [101, 102], twisted double-bilayer graphene (tDBG) [103–106] and twisted trilayer graphene [107]. The benefit of these systems being that the flat bands can occur for larger twist angles, aiding in the fabrication of magic-angle structures. Aside from graphene, twisted TMD homo- and heterostructures are being explored, which have also been predicted to form flat bands [108]. On top of this, their

unique spin-valley characteristics and the formation of moiré excitons make them particularly interesting for optical purposes [109]. Finally, experimental results of twisted 2D magnets are now emerging which have demonstrated the coexistence of ferromagnetic and antiferromagnetic phases in twisted bilayers of CrI$_3$, providing a platform to investigate nanomagnetism [110].

1.4 Measuring the electronic band structure of 2D materials

Many of the phenomena observed in 2D materials, particularly for twisted systems, are closely tied to their electronic structures. Being able to model the electronic structure of these materials and how they change on stacking and twisting with adjacent layers is thus highly useful for predicting the existence of quantum phases in unexplored homo- and heterostructures. In complex systems, such as twisted stacks and 2D magnets, this is far from trivial, however, as accurate calculations can require modelling of am exceptionally large number of atoms. Simplified models have been developed to overcome this, but require comparison with experimental data to validate their results. Standard experimental techniques such as transport and scanning tunnelling spectroscopy (STS) are commonly used to study the electronic properties of materials. However, they are momentum integrated methods and cannot provide precise information regarding the electronic dispersion of a material. Angle-resolved photoemission spectroscopy (ARPES) on the other hand allows for a direct energy and momentum-resolved visualisation of a material's electronic structure.

ARPES utilises a light source to photo-excite electrons from a sample. Measuring the kinetic energy and emission angle of these photoelectrons provides information about the occupied electronic states within the material, allowing a picture of the band structure to be developed. During the photoemission process, which will be explained further in Section 2.1, the in-plane momentum is conserved, while the out-of-plane component is not. This can complicate the interpretation of ARPES spectra from 3D materials due to k_z broadening. Additionally, ARPES is highly surface sensitive, meaning only the top few atomic layers of a bulk material are probed. Consequently, this makes ARPES ideally suited to study 2D materials, as they are governed predominantly by an in-plane dispersion, and the surface sensitivity means only the 2D layers of interest are probed, avoiding spectral contributions from the sample substrate.

The success of ARPES in measuring the electronic structure of 2D materials was demonstrated early-on through studies of graphene grown on SiC. These

were able to confirm the linear and quadratic dispersion of monolayer and bilayer graphene around the **K** point [27, 111], respectively, as well as investigate the evolution of the electronic structure for thicker films. This highlighted a periodic modulation of the photoemission intensity from different π-bands, as a result of the quantised nature of the 2D layers [112]. ARPES measurements from bilayer graphene revealed an energy gap at the charge neutrality point, induced from doping of the bottom layer by the SiC substrate, whose size could be controlled by alkali metal doping to the top surface [27]. Similarly, alkali metal doping was used to increase the carrier concentration in monolayer graphene, giving rise to renormalisation effects [113]. These come from many-body interactions such as electron-phonon and electron-electron coupling, resulting in a modification to the Dirac cone away from the bare-band dispersion predicted by the tight-binding model [114].

The length scale with which different regions can be resolved in ARPES is dependent on the spot size of the photon beam. Conventional ARPES can typically produce beam spot sizes on the order of 10s of micrometres, suitable for studying cleaved bulk single crystals and grown thin films. Exfoliated 2D materials tend to have lateral sizes smaller than this, however, with the regions of interest becoming even smaller when combined into heterostructures and twisted stacks. Furthermore, disorder and imperfections introduced through stacking mean that uniform domains are often only a few micrometres or smaller in size. Thankfully, advancements in optics has enabled the focusing of ARPES beam spots down to the micrometre or sub-micrometre size. Termed micro-ARPES (µARPES), this technique allows small domains to be spatially resolved, making it the primary method to study the electronic structure of 2D material systems.

µARPES has been used extensively to study a range of 2D phenomena, such as the layer-dependent electronic structure of exfoliated flakes [115–117], hybridisation and band alignments within 2D heterostructures [118, 119], and the appearance and characteristics of replica bands in twisted systems [120–123]. Twisted graphene, for example, has garnered particular attention from the µARPES community. Reports on tBG for $\theta > 3°$ have revealed hybridisation gaps and replicas of the Dirac cones at the mBZ corners coming from twist-induced interlayer coupling [124–126]. Additionally, for samples close to the magic-angle, µARPES has observed a flat-like band at the Fermi level [127, 128], however, due to limitations in both energy and momentum resolution, exact details about the flat band topology could not be extracted. In general, detailed comparison to theoretical predictions is also lacking due to the limited scope of many reports, focusing primarily on just one or two twist angles.

Fundamentally, ARPES only maps the occupied electronic states within a material, meaning, for semiconductors, the conduction band cannot be probed without additional doping. As mentioned previously for graphene, this can be achieved by depositing alkali metal atoms on the sample surface, which readily donate their outer valence electron. Though alkali metal doping has proven very successful in studying band gaps and carrier concentration dependent effects in bulk and few-layer 2D materials [111, 129–131], it is limited in control, non-reversible, and can change the chemical composition of the sample. An alternative method is to integrate thin 2D materials into device geometries that utilise a back gate, allowing control of the carrier concentration via electrostatic doping [132, 133]. μARPES systems with feed through electrical contacts allow for simultaneous *in-situ* gating and electronic structure measurements of 2D materials. As well as offering more precise tuning of the carrier density than alkali doping, gating also mimics a device-like setting, allowing one to observe how the electronic structure behaves in operating conditions. Recently, *in-situ* gating of 2D materials has been able to demonstrate direct to indirect transitions and band gap renormalisation effects in monolayer and few-layer TMDs [132], and the electrical tunability of van Hove singularities in tBG [134].

A family of materials currently lacking in terms of μARPES reports is the 2D magnets. This is largely due to the difficulties in fabricating few-layer 2D magnetic samples suitable for ARPES. In the few-layer form they are particularly susceptible to degradation from oxygen and water [49, 50], requiring them to be encapsulated, which, due to the surface sensitivity of ARPES, results in reduced photoemission intensity from the underlying magnetic layers. As such, most reports are from bulk crystals that can utilise conventional ARPES methods and achieve higher energy resolution [63, 64, 135–137]. These have been successful at studying the electronic structure from a number of bulk 2D magnets, however, the semiconducting nature of many of these materials mean that low-temperature measurements in the ordered magnetic phase are inaccessible due to charging effects [63, 136, 137]. Measurements of thin exfoliated flakes using μARPES could help to overcome this limitation. Aside from this, μARPES can also be useful for bulk crystals, as cleaving of certain layered systems can result in multiple terminations that display differing surface states in their ARPES spectra, and whose lateral size is smaller than conventional ARPES beam spots, requiring increased spatial resolution from μARPES [138, 139].

1.5   Outline of Thesis

In this thesis, we use µARPES to study the electronic structure and interlayer interactions within twisted graphene and 2D magnetic systems. Notable features from the measured ARPES spectra are compared to predictions from theory, allowing a test of theoretical models. A description for each of the following Chapters are as follows:

Chapter 2 covers the main experimental techniques and methodologies used throughout this thesis. We begin with an overview of ARPES, outlining how the energy and momentum of measured photoelectrons can be converted to a quantum mechanical description of electrons within solids, before exploring more generally the theoretical framework of photoemission and the processes that govern the measured photoelectron intensity. Following this, we discuss µARPES at the I05 beamline of Diamond Light Source, where all of the photoemission data presented in this thesis was acquired, before finishing with a description of the various fabrication and preparation techniques used for our µARPES samples.

Chapter 3 presents a comparison between ARPES spectra of aligned and twisted few-layer graphene, discussing differences in their electronic structure and how their spectral features can be understood through simulation of the photoemission intensity. Three twisted graphene systems are considered: tBG, tMBG and tDBG, allowing a demonstration of electronic structure changes as a function of both number of layers and twist angle. We end this Chapter by validating various aspects of our twisted graphene data, such as the determined twist angles and sample uniformity, which provides confidence in our results.

Chapter 4 demonstrates how different quantitative parameters, including hybridisation gap sizes and replica band intensities, can be extracted from ARPES spectra of twisted graphene and compared to simulations, allowing a test of predictions from theoretical models. This Chapter concludes with specific analysis of a flat band observed in small-angle tDBG, highlighting potential lattice reconstruction effects, as well as the gate-dependent electronic structure of tMBG.

Chapter 5 studies the electronic structure of bulk CrSBr. This is enabled through exfoliation of flakes on a fresh gold surface, which minimises low-temperature charging effects for semiconducting materials. The electronic structure of CrSBr in the antiferromagnetic phase is characterised and compared to measurements above T_{N}, highlighting a number of band shifts that occur at the antiferromagnetic ordering temperature. Ongoing work to relate these changes to specific magnetic interactions within the crystal is also discussed.

Chapter 6 summarises our results and final conclusions, in addition to the future work that could be undertaken to address some of the remaining open questions. Similar 2D systems to those presented in this thesis are discussed, as well as the recent advancements in sample fabrication that may help to push forward research of 2D materials.

Chapter 2

Methods

2.1 Angle-resolved photoemission spectroscopy

2.1.1 Photoelectron kinematics

ARPES utilises the photoelectron effect, the phenomenon by which electrons are emitted from a material when illuminated by light, to gain insight into the quantum description of solids. By measuring photoemitted electrons over an angular range and applying conservation laws, the energy and momentum of electronic states within the material can be determined. Emitted photoelectrons are characterised by their kinetic energy, E_{kin}, and momentum, $\boldsymbol{K} = \boldsymbol{p}/\hbar$, which are related by $|\boldsymbol{K}| = K = \sqrt{2m_e E_{\text{kin}}}/\hbar$, where m_e is the electron rest mass. Similarly, the photoelectron momentum can be related to the polar, ϑ, and azimuthal, φ, photoelectron emission angles defined in Fig. 2.1(a) by:

$$K_x = \frac{1}{\hbar}\sqrt{2m_e E_{\text{kin}}}\sin\vartheta\cos\varphi, \tag{2.1.1}$$

$$K_y = \frac{1}{\hbar}\sqrt{2m_e E_{\text{kin}}}\sin\vartheta\sin\varphi, \tag{2.1.2}$$

$$K_z = \frac{1}{\hbar}\sqrt{2m_e E_{\text{kin}}}\cos\vartheta, \tag{2.1.3}$$

where $K = \sqrt{K_x^2 + K_y^2 + K_z^2}$. Equivalently, the photoelectron momentum is also often described by components parallel, $K_{\parallel} = \sqrt{K_x^2 + K_y^2}$, and perpendicular, $K_{\perp} = K_z$, to the sample surface [140].

The aim of ARPES is to relate these measurable quantities to the electronic dispersion, $E(\boldsymbol{k})$, within the material. Fig. 2.1(b) shows a generalised illustration of the energy distribution of electrons within a solid and the measured energy dis-
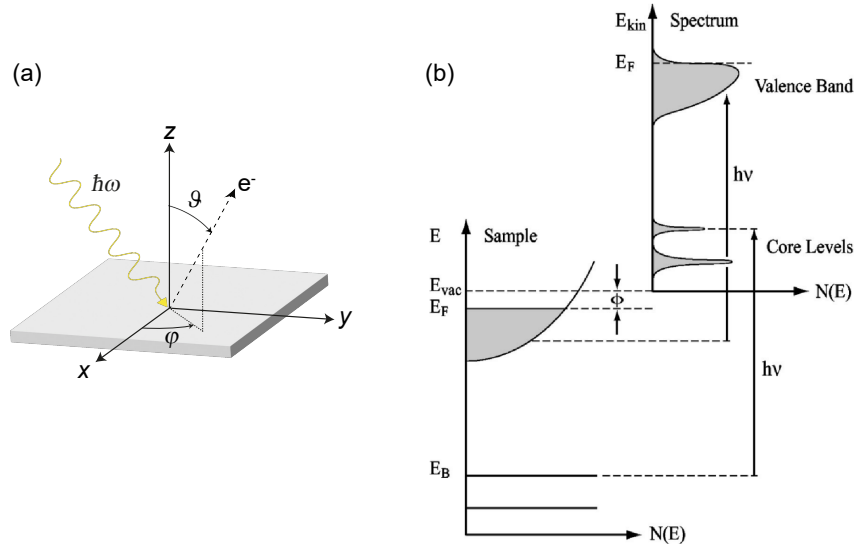
Figure 2.1: a) Schematic of the photoemission geometry in ARPES. Incident light of energy $\hbar\omega$ photoemits an electron whose trajectory is characterised by polar, ϑ, and azimuthal, φ, emission angles. b) Energy distribution of electronic states within a crystal (left) and measured photoelectrons (right) labelled with relevant energy levels, taken from [141].

tribution of photoelectrons. Low-energy electrons occupy the valence band, shown as a continuum of energy states from the bottom of the valence band at E_0 to the Fermi level, E_{F}. These are separated from the vacuum by a potential barrier at the surface, Φ, known as the work function. In ARPES, valence electrons are excited into the vacuum by a photon of energy $\hbar\omega = h\nu$, leading to the conservation of energy relation

$$E_{\mathrm{kin}} = \hbar\omega - \Phi - |E_B|, \tag{2.1.4}$$

where E_B is the binding energy of the electronic state within the material, measured relative to E_{F}. Due to the in-plane translational symmetry at the sample surface, the parallel component of the electron momentum, $k_\parallel$ is conserved during photoemission, such that

$$k_\parallel = K_\parallel = \frac{1}{\hbar}\sqrt{2m_e E_{\mathrm{kin}}}\sin\vartheta. \tag{2.1.5}$$

Together with Eq. (2.1.4), this allows for a full description of the in-plane electronic dispersion to be obtained from the kinetic energy and angular distribution of the measured photoelectrons. On the other hand, the abrupt change in potential along the sample normal means the perpendicular component of the electron momentum, $k_\perp$, is not strictly conserved, with additional momentum contributions coming from

the sample surface. Instead, $k_\perp$ can be estimated using a nearly-free electron approximation,

$$\frac{\hbar^2 k_\perp^2}{2m_e} = \frac{\hbar^2 K_\perp^2}{2m_e} + V_0, \tag{2.1.6}$$

where $V_0 = |E_0| + \Phi$ is known as the inner potential. By substituting in Eq. (2.1.3), one arrives at the equation [142]

$$k_\perp = k_z = \frac{1}{\hbar}\sqrt{2m_e(E_{\text{kin}}\cos^2\vartheta + V_0)}. \tag{2.1.7}$$

In general, V_0 is unknown and material specific. V_0 can either be determined from detailed comparison to theory, or, more conveniently, inferred from periodic features in the measured ARPES spectra. The latter of these usually involves measuring the energy distribution of photoelectrons along the surface normal, i.e. $k_\parallel = 0$ ($\mathbf{\Gamma}$ point), while varying the photon energy and, hence, probing different values of k_z. This results in periodic features in the measured spectra coming from adjacent BZs, allowing V_0 to be deduced. It is worth noting that the finite probing depth of ARPES produces an intrinsic uncertainty in the measured valued of k_z. In highly 2D materials, this has negligible effect due to a lack of out-of-plane dispersion, however, materials with a prominent k_z dispersion display broadening effects in their ARPES spectra due to a range of k_z values being probed [143].

Note, Eqs. (2.1.5) and (2.1.7) ignore momentum transfer from the incident photon. In reality, the photon is an additional source of momentum to the photoelectron that should be included in the momentum conservation. For example, this changes Eq. (2.1.5) to $k_\parallel = K_\parallel - k_\parallel^{\hbar\omega}$, where $k_\parallel^{\hbar\omega}$ is the in-plane component of the photon momentum. Experimentally, this results in a small shift in the photoelectron emission angle, as opposed to if the photon momentum was zero. Due to the trigonometric relationship between the emission angle and the photoelectron momentum, this angular shift is not constant and increases for photoelectrons emitted further from the $\mathbf{\Gamma}$ point, corresponding to higher momentum parts of the BZ. This effectively causes a photon energy (and hence photon momentum) dependent shifting and stretching of the ARPES spectrum in angle space, which should be accounted for within the transformation to reciprocal space.

Thankfully, however, for typical ARPES photon energies (e.g. ~ 100 eV) the photon momentum is small on the scale of the BZ. For example, a photon of energy 100 eV has a momentum of ~ 0.05 Å^{-1} – only 3% of the BZ of graphene when considering the reciprocal space distance from $\mathbf{\Gamma}$ to $\mathbf{K}$. This means that, though there is some variation in the angular shift of photoelectrons as a function of their momentum, this is approximately constant across the BZ, and so the photon momentum

can be accounted for by a constant angular shift. In practice, this angular shift is a translation of the measured ARPES spectrum such that the measured $\boldsymbol{\Gamma}$ point coincides with normal emission (which is not exactly the case due to the transferred photon momentum). If the photon energy were much higher, however, for example in the case of soft x-ray ARPES, then the photon momentum would be comparable to the size of BZ and pronounced stretching effects would be observed in the angular spectrum. Proper treatment of the photon momentum in the transformation to reciprocal space would thus be required.

Note, in moiré systems, the mBZ can be of similar size to that of the photon momentum (a 100 eV photon is $\sim \frac{1}{3}$ of the mBZ of $3°$ twisted graphene). Though this may have some effect for moiré features around the $\boldsymbol{\Gamma}$ point, we do not believe this to be important for those around the BZ corners (which we will focus on later). This is because photoelectrons emitted from around the $\mathbf{K}$ points, though contained within a mBZ, still have a large momentum in comparison to the photon momentum, and so the photon momentum can be accounted for as described above.

2.1.2 Photoemission process

Fundamentally, photoemission describes the excitation of an electron from an initial state within a material, i, into a final state in the vacuum, f, through interaction with a photon. The probability of this optical transition, w_{fi}, is given by Fermi's golden rule,

$$w_{fi} = \frac{2\pi}{\hbar} |\langle \Psi_f^N | H_{int} | \Psi_i^N \rangle|^2 \delta(E_f^N - E_i^N - \hbar\omega), \tag{2.1.8}$$

where Ψ_i^N, E_i^N and Ψ_f^N, E_f^N are the wavefunctions and corresponding energies for the N-electron initial and final states, respectively [140]. H_{int} is the electron-photon interaction Hamiltonian which can be approximated by

$$H_{int} = \frac{e}{2m_e c}(\mathbf{A} \cdot \mathbf{p} + \mathbf{p} \cdot \mathbf{A}) = \frac{e}{m_e c}\mathbf{A} \cdot \mathbf{p}, \tag{2.1.9}$$

where $\mathbf{p} = i\hbar\nabla$ is the momentum operator and $\mathbf{A}$ is the electromagnetic vector potential. In Eq. (2.1.9), only first order terms in $\mathbf{A}$ have been included, and the final result was obtained by using the commutator relation $[\mathbf{p}, \mathbf{A}] = -i\hbar\nabla \cdot \mathbf{A}$ and the dipole approximation $\nabla \cdot \mathbf{A} = 0$.

The transition from initial state in the crystal to final state in the vacuum is most accurately described by a single coherent process. In this approach, known as the one-step model (Fig. 2.2(a)), the wavefunction must take into account bulk, surface and vacuum states, including their finite overlap, in addition to potential rel-
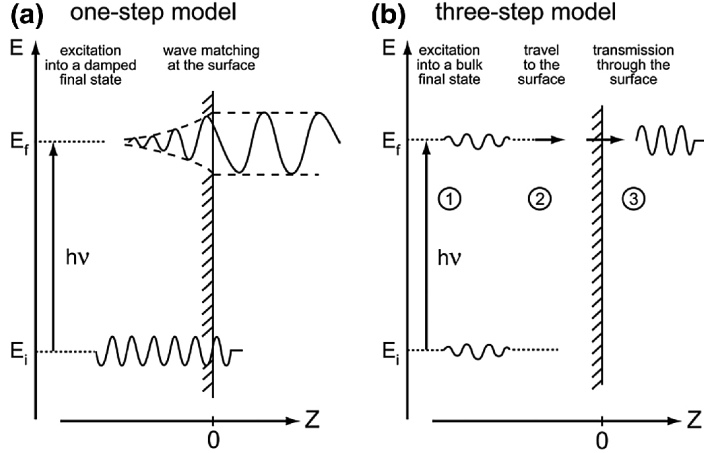
Figure 2.2: Illustrations of the (a) one-step and (b) three-step models used to describe the photoemission process, adapted from [141].

ativistic and many-body effects [144, 145]. Calculation of this can be rather complex and, as such, many descriptions of photoemission use a simplified phenomenological three-step model (Fig. 2.2(b)) [146]. This separates the photoemission process into three independent steps: (1) excitation of an initial state electron into an excited final state in the bulk; (2) travel of the excited electron to the sample surface; (3) emission of the electron into the vacuum. The total photoemission intensity is thus a product of these three processes. Step (1) follows on from the Fermi's golden rule description in Eq. (2.1.8) and will be discussed next. Step (2) can be described by a mean free path approach that details the probability of inelastic scattering within the crystal, discussed at the end of this section. Finally, step (3) involves the transmission of the electron through the surface potential, characterised by the work function, Φ, as covered in the previous section [140].

Continuing with a description for step (1) of the three-step model, Eq. (2.1.8) can be expanded by expressing the wavefunctions as a product of photoexcited electron and $(N-1)$-electron terms. This can be done using the sudden approximation, which assumes the photoemission process to be very rapid and that the photoelectron is unaffected by relaxation effects in the $(N-1)$-electron system. This effectively decouples the two wavefunctions, allowing them to be treated as independent terms. Note, the sudden approximation is not valid in the low kinetic energy limit [147], however, ARPES experiments typically produce photoelectrons above this threshold. Using the sudden approximation, Ψ_f^N can be written as

$$\Psi_f^N = \mathcal{A}\phi_f^{\boldsymbol{k}}\Psi_f^{N-1}, \tag{2.1.10}$$

26

where $\mathcal{A}$ is an antisymmetric operator that ensures the Pauli exclusion principle is satisfied, $\phi_f^{\boldsymbol{k}}$ is the wavefunction of the excited final state electron with momentum $\boldsymbol{k}$, and Ψ_f^{N-1} is the final state wavefunction of the $(N-1)$-electron system. Similarly, the initial state wavefunction can be expressed as a product of a one-electron orbital, $\phi_i^{\boldsymbol{k}}$, and an $(N-1)$-electron system, such that

$$\Psi_i^N = \mathcal{A}\phi_i^{\boldsymbol{k}}\Psi_i^{N-1}. \tag{2.1.11}$$

Using Eqs. (2.1.10) and (2.1.11), the matrix elements in Eq. (2.1.8) can be expanded as

$$\langle \Psi_f^N | H_{int} | \Psi_i^N \rangle = \langle \phi_f^{\boldsymbol{k}} | H_{int} | \phi_i^{\boldsymbol{k}} \rangle \langle \Psi_m^{N-1} | \Psi_i^{N-1} \rangle, \tag{2.1.12}$$

where Ψ_f^{N-1} has been replaced by Ψ_m^{N-1} to account for the many possible different final states of the $(N-1)$-electron system, and the total transition probability is given by a sum over all possible states m [140].

The total photoemission intensity, I, is given by the sum of w_{fi} over all initial and final states. Expressed in terms of kinetic energy, E_{kin}, at momentum, $\boldsymbol{k}$, this returns the result

$$I(E_{\text{kin}}, \boldsymbol{k}) = \frac{2\pi}{\hbar} \sum_{f,i} |\langle \phi_f^{\boldsymbol{k}} | H_{int} | \phi_i^{\boldsymbol{k}} \rangle|^2 \sum_m |\langle \Psi_m^{N-1} | \Psi_i^{N-1} \rangle|^2 \delta(E_{\text{kin}} + E_m^{N-1} - E_i^N - \hbar\omega), \tag{2.1.13}$$

which uses the definition $E_m^N = E_{\text{kin}} + E_m^{N-1}$, and can be shortened to the form

$$I(E_{\text{kin}}, \boldsymbol{k}) = \frac{2\pi}{\hbar} \sum_{f,i} |M_{fi}^{\boldsymbol{k}}|^2 \sum_m |c_{mi}|^2 \delta(E_{\text{kin}} + E_m^{N-1} - E_i^N - \hbar\omega). \tag{2.1.14}$$

Here, $M_{fi}^{\boldsymbol{k}} = \langle \phi_f^{\boldsymbol{k}} | H_{int} | \phi_i^{\boldsymbol{k}} \rangle$ is known as the one-electron dipole matrix element, and $|c_{mi}|^2 = |\langle \Psi_m^{N-1} | \Psi_i^{N-1} \rangle|^2$ is the probability that removal of an electron from state i will leave the $(N-1)$-electron system in an excited state m [140].

Focusing initially on the latter of these two terms, for a non-interacting particle system, $|c_{mi}|^2$ is non-zero only for $m = i$ and the measured ARPES spectra is a delta function at the energy and momentum of state i. In reality, however, many-body interactions cause a finite overlap between several different wavefunctions, meaning $|c_{mi}|^2$ is non-zero for many different m states. This many-body picture is best treated by a Green's function approach which can describe the propagation of a particle in a many-body system. As a function of energy and momentum, the one-particle Green's function, $G(E, \boldsymbol{k})$, is related to the one-particle spectral function,

$A(E, \boldsymbol{k})$ by

$$A(E, \boldsymbol{k}) = A^+(E, \boldsymbol{k}) + A^-(E, \boldsymbol{k}) = -\frac{1}{\pi} \text{Im} G(E, \boldsymbol{k}), \qquad (2.1.15)$$

where $A^+(E, \boldsymbol{k})$ and $A^-(E, \boldsymbol{k})$ are the one-particle addition and removal spectra, respectively. Notably, $A^-(E, \boldsymbol{k})$ can be shown to be equal to the sum over m in Eq. (2.1.13), demonstrating the connection between the spectral function and photoemission and the ability to measure it from ARPES [140].

In the presence of electron-electron or electron-phonon interactions, the spectral function can conveniently be expressed in terms of the electron self-energy, $\Sigma(E, \boldsymbol{k}) = \Sigma'(E, \boldsymbol{k}) + \text{i}\Sigma''(E, \boldsymbol{k})$, by

$$A(E, \boldsymbol{k}) = -\frac{1}{\pi} \frac{\Sigma''(E, \boldsymbol{k})}{[E - (\epsilon_{\boldsymbol{k}} + \Sigma'(E, \boldsymbol{k}))]^2 + [\Sigma''(E, \boldsymbol{k})]^2}, \qquad (2.1.16)$$

where $\Sigma'(E, \boldsymbol{k})$ and $\Sigma''(E, \boldsymbol{k})$ are the real and imaginary components of the self energy, respectively, and $\epsilon_{\boldsymbol{k}}$ is the band energy of an electron with momentum $\boldsymbol{k}$ propagating in a many-body system. Eq. (2.1.16) resembles a Lorentzian function with a peak centre given by $(\epsilon_{\boldsymbol{k}} + \Sigma'(E, \boldsymbol{k}))$ and a width proportional to $\Sigma''(E, \boldsymbol{k})$. Therefore, in addition to containing information on the energy-momentum dispersion of electrons within a material, the spectral function also describes many-body renormalisation effects, seen in the offset of $\epsilon_{\boldsymbol{k}}$ due to the real part of the self-energy, as well as lifetime broadening effects from the imaginary part of $\Sigma(E, \boldsymbol{k})$ [140, 148].

Returning to the matrix element, $M_{fi}^{\boldsymbol{k}}$, this describes the probability of an electron in state i being excited into a state f following interaction with a photon. Using the description of H_{int} in Eq. (2.1.9), $M_{fi}^{\boldsymbol{k}}$ can be expanded to give terms dependent on the incident photon polarisation vector, final state electron momentum, angular distribution of electron orbitals, and incident photon energy. From this, for a given electron orbital, it can be shown that $M_{fi}^{\boldsymbol{k}} = 0$ for light of certain polarisation vector and energy. $M_{fi}^{\boldsymbol{k}}$ is thus intimately tied to the specific measurement conditions and can provide information regarding the orbital symmetry of different electronic states [142, 149].

The total photoemission intensity is often rewritten as

$$I(E, \boldsymbol{k}) = I_M(\boldsymbol{k}, \hbar\omega, \mathbf{A}) \cdot f(E) \cdot A(E, \boldsymbol{k}), \qquad (2.1.17)$$

where $I_M(\boldsymbol{k}, \hbar\omega, \mathbf{A}) \propto |M_{fi}^{\boldsymbol{k}}|^2$, and $f(E)$ is the Fermi-Dirac distribution,

$$f(E) = \frac{1}{\text{e}^{(E - E_\text{F})/k_B T} + 1}, \qquad (2.1.18)$$

where T is the sample temperature, which has been included as only occupied states are probed from photoemission. The total photoemission intensity is thus given by a product of three terms: the spectral function, which describes the probability of an electron being found in a particular energy and momentum state under the influence of many-body interactions; the Fermi-Dirac distribution, which describes the probability of a given energy state being occupied at a finite temperature; and the one-electron matrix element, which describes the probability of an electron contributing to the photoemission intensity under specific measurement conditions. Together, these factors contribute to the measured spectra in ARPES, allowing the study of the electronic ground state within a material. It should be noted that factors such as the finite experimental resolution and an inelastic background have not been included in Eq. (2.1.17) but also contribute to the final measured intensity [140].

Surface sensitivity

In the description for step (2) of the three-step model, the excited final state electron propagates to the surface and is treated as being quasi-free, but can undergo inelastic scattering events. The characteristic length scale with which the electron travels before being inelastically scattered is known as the mean free path, λ, and the probability of a scattering event increases exponentially with distance travelled. Consequently, the intensity of photoelectrons escaping the material from a depth z without undergoing an inelastic scattering event, and thus contributing to the measured intensity in Eq. (2.1.17), decays exponentially according to

$$I(z) = I_0 \mathrm{e}^{-\frac{z}{\lambda}}, \tag{2.1.19}$$

where I_0 is the initial intensity of excited electrons. A larger λ indicates a greater depth within a material from which photoelectrons can escape without being inelastically scattered, and thus a greater depth that can be probed by ARPES.

The mean free path of electrons within a solid varies as a function of kinetic energy and is approximately given by the Universal curve, shown in Fig. 2.3. ARPES is typically performed using photon energies of 20–200 eV, which, incidentally, coincides with a minimum in the mean free path [150]. This puts $\lambda \lesssim 10$ Å, corresponding to only a few atomic layers and making ARPES extremely surface sensitive. As mentioned previously, this can be advantageous for the study of 2D materials, as only the top layers of interest are probed and signal from the underlying substrate is effectively blocked. However, the surface sensitivity also highlights the need for an atomically clean surface to reduce inelastic scattering from sur-
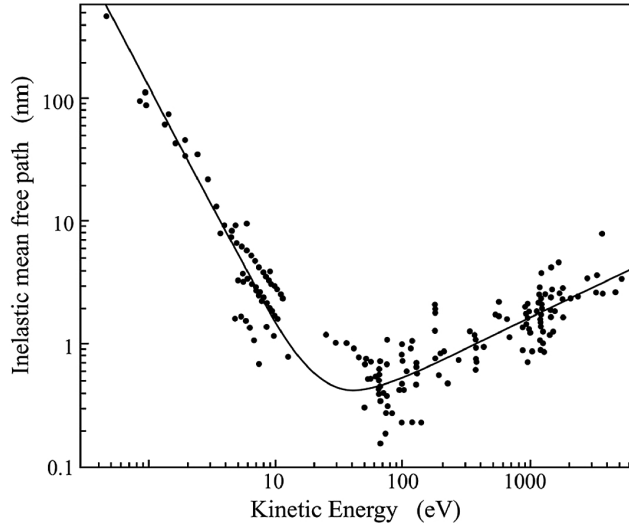
Figure 2.3: Kinetic energy dependence of the inelastic mean free path of electrons in a solid, taken from [150].

face contamination. Methods of achieving this for 2D materials will be covered in Section 2.3.4.

2.2 Spatially-resolved ARPES

2.2.1 Synchrotron radiation

ARPES requires an intense monochromatic source of light to probe the electronic structure of a material through photoemission. Typical laboratory setups use either gas discharge lamps or lasers as light sources, however, these are limited to only a few discrete photon energies [151]. Additionally, the intensity of these sources is relatively weak, with further intensity lost due to focusing optics. As such, the majority of ARPES setups utilise synchrotron lights sources which offer orders of magnitude higher flux than lab based sources and can cover a wide spectral range, in addition to variable polarisation capabilities.

Synchrotron radiation is produced when charged particles moving at relativistic speeds are radially accelerated, causing them to emit electromagnetic waves along their direction of motion. Synchrotron facilities utilise this effect to produce highly intense beams of light through the acceleration of electrons. In practice, this acceleration is achieved through magnetic fields that cause the electrons to orbit perpendicular to the applied field lines, meaning the radiation is emitted tangentially to the circular trajectory of the electrons. To achieve the relativistic speeds required,

30

the electrons are initially accelerated by a linear accelerator (Linac), where they gain MeVs worth of energy, and then by a circular accelerator, known as a booster ring, that increases their energy further to the GeV range. The electrons are then transferred into the main ring of the synchrotron, known as the storage ring [152].

The storage ring consists of a series of straight sections connected by bending magnets, so as to create a closed loop for the electrons to travel around. Synchrotron radiation is produced when the electrons pass through the bending magnets, as well as through insertion devices, know as wigglers and undulators, fitted into the straight sections [152]. The radiation produced in each straight section continues moving forward into the connecting synchrotron beamline, where it is used for various experiments, while the electrons are diverted by the bending magnets into the next straight section. The storage ring also contains various radio frequency cavities that accelerate the electrons using electric fields to account for the energy lost from synchrotron radiation [151].

The mentioned insertion devices are made up of a series of magnets designed to oscillate the electrons through a sinusoidal-like path. The electrons emit radiation through each bend, offering greatly increased spectral brightness compared to bending magnets. Insertion devices come in two forms: wigglers and undulators, with their main difference being the size of their oscillations and the resulting spectral distribution of radiation. In wigglers, the oscillation amplitude is large and each pulse of radiation can be considered separate from each other. This is similar to the case of bending magnets which have a single emission pulse with a broad energy distribution. Wigglers can thus be thought of as a series of bending magnets. In undulators, however, the oscillations are weak and each emission pulse overlaps with those before it. This results in an interference effect that produces an intense narrow band in the energy distribution. Furthermore, the energy peak of this emission can be controlled by changing the undulator gap (distance between upper and lower magnets) making it ideal for techniques requiring tunable monochromatic light [153]. Additionally, the polarisation of emitted light can be controlled by lateral displacement of the sets of magnets [154]. As such, ARPES beamlines typically use undulators to produce their photon beams.

2.2.2   I05 nanoARPES, Diamond Light Source

All µARPES data presented in this thesis have been acquired using the nanoARPES branch of the I05 beamline at Diamond Light Source, able to perform spatially-resolved ARPES on samples down to the micrometre and sub-micrometre scale. A layout of the beamline is shown in Fig. 2.4, where synchrotron light produced by
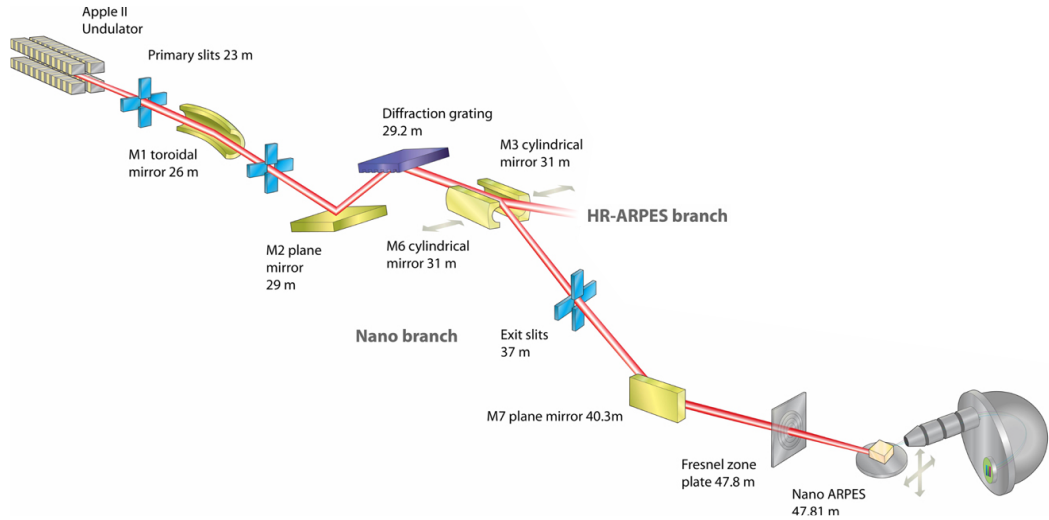
Figure 2.4: Schematic layout of the optics at the I05 nanoARPES beamline, adapted from [155].

an undulator in the energy range 18–240 eV passes through a series of elements, including mirrors to divert and focus the beam, shutters or slits to control the beam divergence and intensity, and a diffraction grating to monochromate the beam [155]. For completeness, we also mention that the I05 beamline has a second branch, known as the high-resolution branch, used for conventional ARPES, but was not used within this thesis.

At the entrance to the nanoARPES branch is a set of shutters known as the exit slit. By adjusting the size of the opening, the exit slit controls the intensity of the beam reaching the sample in addition to the beam divergence, which also plays a role in further monochromating the beam and, hence, adjusting the energy resolution. A trade off must be made with setting the size of the exit slit: a larger opening provides a higher intensity beam and, thus, increased photoelectron signal, but at the expense of worse energy resolution. How the exit slit is set is therefore dependent on the specific experimental requirements.

The nanoARPES endstation is an ultra-high vacuum (UHV) chamber with a base pressure of $\sim 1 \times 10^{-10}$ mbar that houses the sample stage and optics used to focus the synchrotron beam onto the sample, and is attached to an external hemispherical analyser for the detection of photoelectrons. The sample stage is cooled by a liquid helium cryostat, with a base sample temperature of ~ 30 K. Additionally, feed-through electrical contacts on the sample stage allow for *in-situ* electrical control and gating of 2D devices. A choice of two focusing optics are available within the chamber: a Fresnel zone plate [156], and a capillary mirror [157].

These will be covered in more detail in the next section, but both offer high spatial resolution with different functionalities.

An approximate schematic of the sample and analyser geometry for the nanoARPES endstation is presented in Fig. 2.5. Fig. 2.5(a) depicts a focused beam of synchrotron light incident on a sample surface and the excitation of a photoelectron, while Fig. 2.5(b) offers a top-down view of this setup. The sample itself is mounted on a manipulator that has five degrees of freedom, allowing translational movement of the sample in the x, y (sample plane) and z (sample normal) directions, as well as azimuthal rotation, φ, in the $x - y$ plane, and polar rotation, ϑ_s, in the $x - z$ plane, measured relative to the beam axis. In addition to these parameters, the analyser can also be rotated through a polar angle, ϑ_a, relative to the sample normal.

During µARPES measurements, ϑ_s is kept constant and ϑ_a is used as the variable rotation parameter when mapping the electronic structure. This is because even a small rotation of the sample polar angle can result in translation of the sample relative to the beam spot, losing the correct measurement position. In standard operating conditions, the sample polar angle is set to $\vartheta_s = 45°$ so that normal emission of photoelectrons is approximately along the analyser polar 'zero' point. In some cases, however, the sample polar angle is reduced to allow a greater photoelectron emission angle to be accessed by the analyser. This is particularly useful at lower photon energies when the BZ is larger in angle space, and thus a large polar rotation is required to access the BZ edges.

Also depicted in Figs. 2.5(a) and (b) are the possible linear polarisation vectors for the synchrotron beam, namely linearly horizontal (LH) and linear vertical (LV). Changing between these polarisations changes the orientation of the electric field vector relative to the sample, and thus, according to the matrix element derived in Section 2.1.2, can affect the measured intensity of certain bands in ARPES. This is particularly relevant for the results presented in Chapter 5, and so, we outline explicitly that LV is entirely in the sample plane and points along the y-axis, while LH has components both in-plane along x, and out-of-plane along z, dependent on ϑ_s.

The nanoARPES branch is equipped with a Scienta DA30 hemispherical analyser for the detection of photoelectrons. In these types of analysers, photoelectrons enter into a lens column, where they are focused through an opening to a hemisphere. Within the hemisphere, photoelectrons travel through a circular trajectory, due to a perpendicular electric field, to a detector on the other end of the hemisphere. For a constant electric field strength, the radius of the photoelectron's
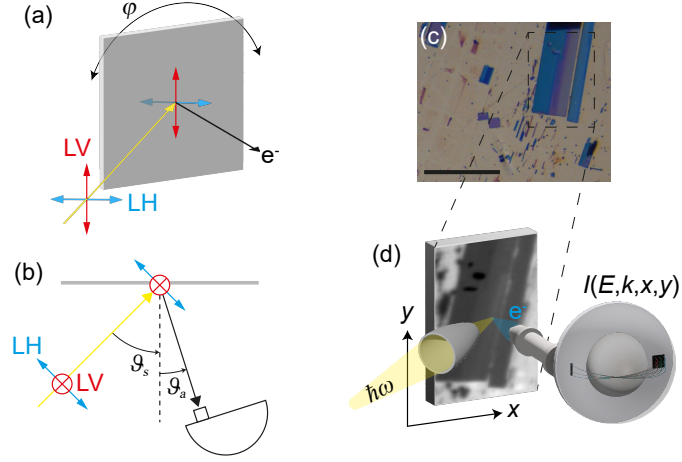
Figure 2.5: a) Schematic of the I05 nanoARPES sample stage geometry, showing light of linear horizontal (LH) or linear vertical (LV) polarisation incident on a sample surface, which can be rotated by an azimuthal angle, φ, in the sample plane. b) Top-down view of (a) illustrating the polar rotation angles ϑ_s and ϑ_a of the sample and analyser, respectively. c) Optical image of an exfoliated CrSBr flake. d) Schematic of the SPEM mapping capabilities of the nanoARPES endstation. SPEM image in (d) is of the dashed box region in (c).

orbit is dependent on its velocity and, hence, kinetic energy. Photoelectrons with different kinetic energy are thus incident on different positions on the detector, filtering them according to their kinetic energy. The energy range acquired by the detector is set by two parameters known as the pass energy, E_p, and centre energy, E_c. Photoelectrons are accelerated/retarded in the lens column by an energy $E_p - E_c$, such that those entering the lens column with a kinetic energy equal to the centre energy enter the hemisphere with kinetic energy equal to the pass energy. This simultaneously sets the energy range measured by the detector, dependent on the geometrical ratio between the size of the hemisphere and the detector width, multiplied by the pass energy. In practice, a larger pass energy gives a larger energy window, but also worsens the energy resolution. E_p and E_c can thus be tuned depending on the experiment.

The opening of the hemispherical analyser is a vertical slit with long axis aligned with the y-direction of the sample. The slit has an approximate $\pm 15°$ acceptance angle and variable width that defines an angular resolution. The opening allows the analyser detector to collect a 2D dataset of photoelectron intensities as a function of their kinetic energy, and detector entrance angle, equal to the photoelectron emission angle in the $y - z$ plane. Converting this into reciprocal space coordinates provides an $I(E, k)$ cut through a particular direction in reciprocal space,

dependent on the azimuthal and polar coordinates of the sample and analyser. Polar rotation of the analyser then maps out an $I(E, k_x, k_y)$ region of reciprocal space, providing a Fermi surface map of the in-plane electronic structure.

It is common to report measured ARPES spectra as energy-momentum ($I(E, k)$) cuts along high symmetry directions of the BZ. One method of acquiring this is to align the high symmetry directions with the vertical slit of the analyser, providing a direct image of the desired reciprocal space cut. This can offer high statistical data, dependent only on the photoelectron flux and acquisition time. Alternatively, the high symmetry cut can be extracted from the Fermi surface through an interpolation. This can be particularly useful in systems where alignment of the high symmetry directions with the analyser is challenging, such as in twisted samples. As such, to outline here explicitly, energy-momentum cuts for twisted graphene in Chapters 3 and 4 have been extracted from Fermi surface maps, while in Chapter 5, the ARPES spectra of CrSBr are from alignment of the high symmetry directions with the analyser.

ARPES lacks a conventional microscopy setting that allows the sample to be viewed in real-time, such as that available in electron microscopy techniques. Instead, in µARPES, the sample can be visualised by raster scanning in x and y while measuring the photoemission intensity, known as scanning photoemission microscopy (SPEM). Differing intensity from neighbouring parts of the sample (coming from a difference in material or sample environment) provides contrast in the resulting image, allowing it to be compared to optical images taken prior to ARPES (Figs. 2.5(c) and (d)). In fact, SPEM acquires a 4D dataset of $I(E, k, x, y)$, meaning each (x, y) position measured has a corresponding $I(E, k)$ spectrum. As will be demonstrated in Chapter 3, this allows for an in-depth analysis of the SPEM image which can enhance contrast and highlight particular regions of interest.

2.2.3 Spatial resolution

As mentioned previously, the I05 nanoARPES beamline has two focusing optics available for µARPES: a Fresnel zone plate and a capillary mirror, shown schematically in Figs. 2.6(a) and (b), respectively. The zone plate consists of a series of concentric circular slits that focus the synchrotron beam by a diffractive interference effect (in reality the slits are held by a frame and so they are more like circular segments). These types of focusing optics can routinely achieve a focal spot size of less than a micrometre, making them well suited to spatially-resolved ARPES [156, 158]. As well as the main (1st order) focal point, however, there are a number of additional focal points coming from higher order diffraction terms, as well as a zero
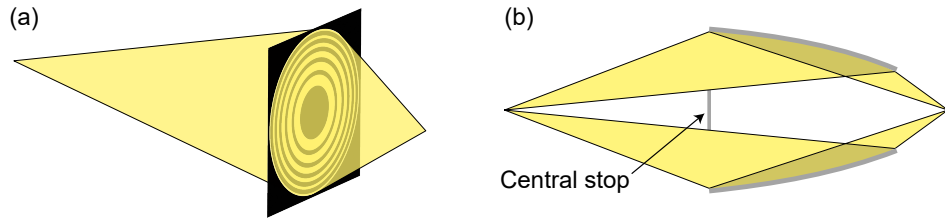
Figure 2.6: Schematics of the (a) Fresnel zone plate and (b) capillary mirror used for focusing synchrotron light for spatially-resolved ARPES. The capillary mirror central stop blocks light that would otherwise travel through without being focused.

order term due to the undiffracted part of the beam. These can contribute to a constant background in photoemission spectra, thus zone plates are paired with an order-sorting aperture (OSA) to block these higher order and zero order diffraction peaks. The diffractive nature of the zone plate also means the focal point position changes with photon energy. This means, in practice, µARPES experiments using the zone plate only operate at a single photon energy, as changing of the energy requires complete realignment of the sample and optical systems. On top of this, due to spatial constraints within the UHV chamber, and an absorption edge coming from the Si membrane of the zone plate itself, the nanoARPES branch zone plate can only operate using photon energies of ∼70–100 eV. Finally, zone plates also suffer from low efficiency, with typically only 10% of the original beam (i.e., the synchrotron light incident on the back of the zone plate) contributing to the focused beam spot.

The capillary mirror is an elliptically-shaped conical mirror for the focusing of synchrotron light that possesses many benefits over the zone plate [157]. Firstly, the reflective focusing is achromatic, allowing for simple photon energy dependent ARPES studies to be performed without time consuming realignment or loss of sample position. Secondly, the capillary mirror can provide a much more intense beam spot than the zone plate (almost 20 times greater). This comes both from the capillary having greater efficiency than the zone plate, but also a larger opening at the back of the capillary, allowing a higher proportion of the synchrotron beam to be focused onto the sample (the profile of the synchrotron beam is often much larger than the focusing optics). This enables higher energy resolution measurements as more intensity can be sacrificed to use lower pass energy modes and a smaller exit slit opening. As such, the majority of ARPES data presented in this thesis were acquired using the capillary mirror.

The drawback of the capillary mirror is that it cannot reach as small a spot size as the zone plate. Currently, the I05 nanoARPES capillary mirror can provide a

36
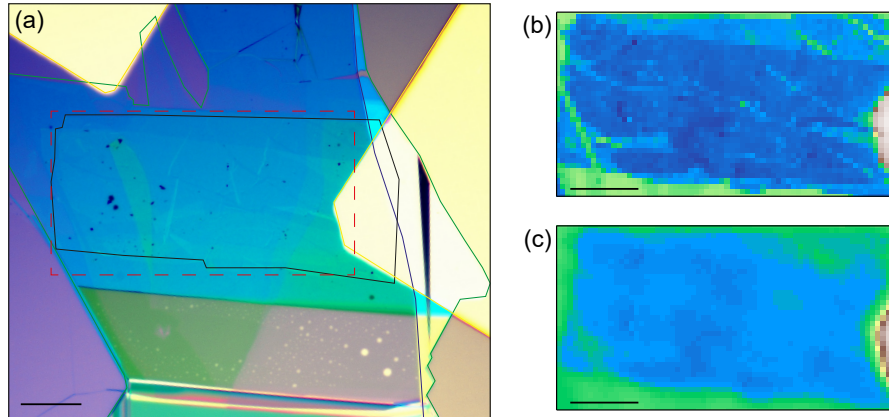
Figure 2.7: a) Optical image of a twisted bilayer graphene sample with metal contacts. Solid lines mark the twisted graphene (black), Au contacts (yellow), hBN (green) and graphite (indigo) regions. b,c) SPEM images from the red dashed box region in (a) acquired using the (b) zone plate and (c) capillary mirror. Scale bars are 20 µm.

minimum beam spot size of 4–5 µm in diameter, placing limitations on what samples and features can be measured using the capillary mirror. The difference in resolving power is best exemplified by comparing SPEM images acquired using the two optics, as shown in Fig. 2.7 for an example twisted bilayer graphene sample. The SPEM image from the zone plate in Fig. 2.7(b) shows much greater detail, able to reveal cracks and wrinkles within the sample, whereas the capillary mirror SPEM image appears washed out in comparison. Nonetheless, we will demonstrate in the next Chapter how SPEM can be used to identify uniform sample regions that are large enough for the capillary mirror to resolve.

2.3   Sample fabrication and preparation

2.3.1   Polymer-based stacking of 2D layers

Twisted samples made from exfoliated flakes are typically fabricated using polymer-based stamping techniques that allow for the pickup and manipulation of 2D layers. The two most common of these techniques are loosely referred to as the PDMS and PMMA methods [68]. Beginning with the former, the PDMS method is shown schematically in Fig. 2.8 in the context of fabricating a 2D heterostructure. Details on the use of these methods for fabricating twisted structures will be discussed at the end of this section.

The first step in the PDMS technique is the creation of a polymer stamp
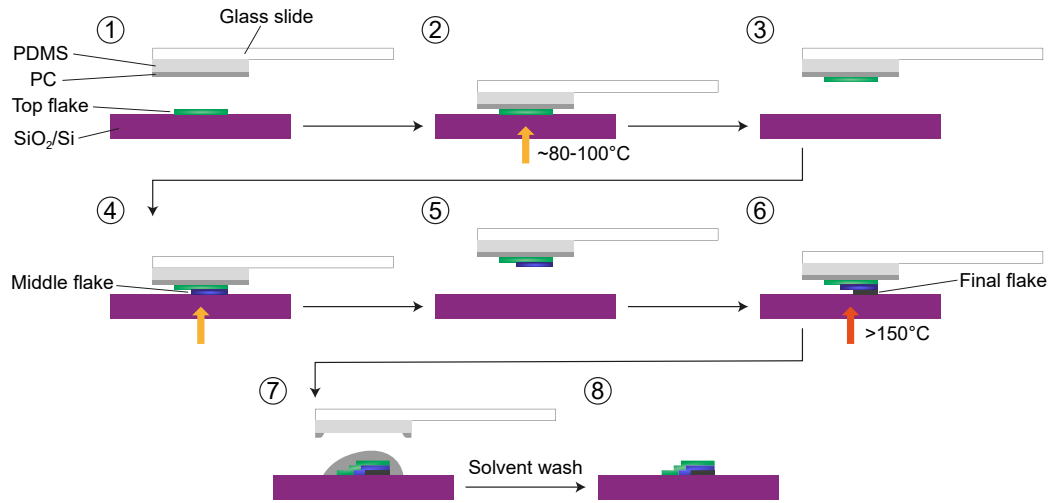
Figure 2.8: Schematic of the PDMS polymer transfer method. 1) A PC coated PDMS stamp is aligned with an initial flake exfoliated onto a SiO_2/Si substrate. 2) The stamp is brought into contact with the flake and heated on a hot plate to a temperature of 80–100°C. 3) The flake adheres to the stamp, allowing it to be lifted off the substrate. 4) The stamp and initial flake are brought into contact with another exfoliated flake. 5) The van der Waals forces between flakes allows the second flake to be picked up. Steps (4) and (5) can be repeated for an arbitrary number of flakes. 6) When in contact with the final flake, the hot plate is heated to a temperature above 150°C. 7) The PC melts onto the substrate, allowing the stack to be detached from the stamp. 8) The PC is removed using solvents, leaving the finished heterostructure.

that consists of a glass slide with an attached polydimethylsiloxane (PDMS) layer coated in a polycarbonate (PC) film (1). The PC acts as an adhesion layer, while the PDMS controls contact with the exfoliated flakes due to variable thermal expansion [69]. Importantly, all parts of the stamp are transparent, allowing it to be used in conjunction with a microscope for the controlled alignment with target flakes. Using a micro-manipulator, the stamp can be brought slowly into contact with an initial flake exfoliated on a substrate (2). As will be seen, this flake forms the top layer in the resulting 2D stack. Heating of the substrate using a hot plate increases the contact area and adhesion of the PC with the flake, due to the as mentioned expansion of the PDMS. Once in full contact with the flake, the stamp is lifted, picking up the flake (3).

The stamp can then be used to pickup subsequent flakes in much the same way. Here, the initial flake on the stamp is aligned with a second flake and the area of contact controlled by heating (4). The van der Waals forces between flakes create a preferential adhesion compared to the flake and the substrate, allowing the second

flake to be picked up using the first (5) [69, 159]. These steps can be repeated an arbitrary number of times, continually building up a thicker heterostructure stack. Once finished, reliable release of the stack from the polymer stamp can be challenging due to the different adhesive forces present. A common alternative is to heat the substrate to a high temperature once the stamp is brought into contact with the final flake (6). This melts the PC film onto the substrate, detaching it completely from the PDMS layer (7). The PC can then be removed using a solvent wash leaving the heterostructure stack on the substrate, where the initial flakes are the top most layers [69].

The PDMS method is a fast and efficient technique in the fabrication of 2D heterostructures. The process of picking up exfoliated flakes with other flakes often leads to contamination free interfaces that enhance sample quality [68, 69, 159]. This is only the case for the buried interfaces, however, as the PC film is known to leave a residue on the exposed surface, made worse when using the melting release process. For transport devices, this isn't a problem as the flakes of interest are often encapsulated between layers of hBN, however, ARPES samples can suffer greatly from the polymer residue due to the surface sensitivity. Furthermore, the adhesion of the PC film to the 2D flakes varies for different materials. hBN is often used as the initial flake due to its strong adhesion to the PC, but, again, this is incompatible with ARPES due to the surface sensitivity, unless the hBN is a monolayer.

The second commonly used polymer transfer technique is the PMMA method (Fig. 2.9) [68, 71]. In this method, the initial flake is exfoliated straight onto a polymer coated substrate, which consists of a SiO_2/Si wafer spin coated with a layer of polyvinyl alcohol (PVA) and subsequent polymethyl methacrylate (PMMA) (1). The PMMA acts as a carrier layer for the exfoliated flake, while the PVA is a sacrificial layer that allows the PMMA to be detached from the substrate. A circle centred on the target flake is etched into the PMMA using a scalpel to separate it from the surrounding polymer film (2). The whole substrate is then placed in a bath of deionised water to dissolve the PVA layer (3). Once the PVA under the flake is fully dissolved, the PMMA is released and floats to the surface of the water (4). The PMMA carrying the flake is fished out of the water using a stamp that consists of a stainless steel holder, referred to as a plectrum, attached to a glass slide (5). The end of the plectrum is a circular ring that allows the flake to be viewed when the stamp is inverted (6). At this point the stamp may be used in the same way as the PDMS stamp where the initial flake is used to pickup subsequent layers, however, the weaker adhesion of the flake to the PMMA usually means it is transferred and deposited onto a target flake instead (7/8) [68].
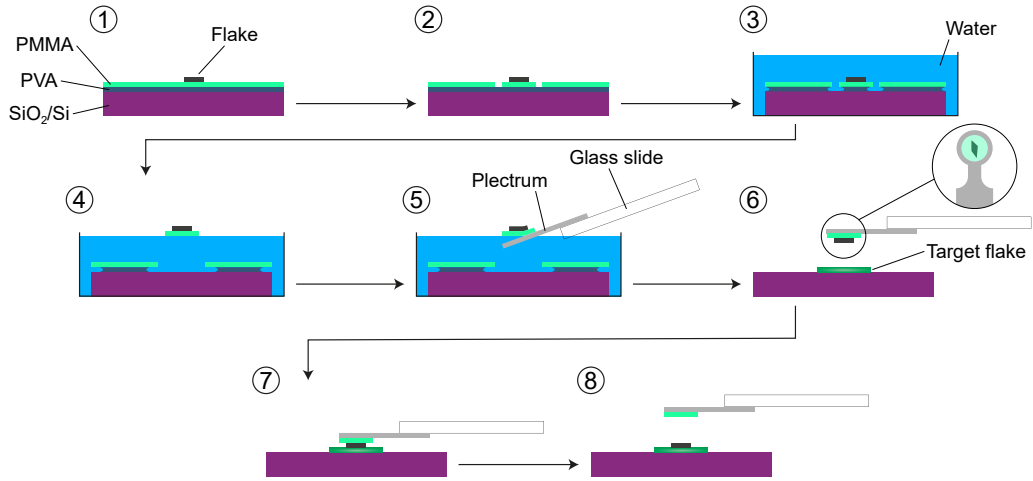
Figure 2.9: Schematic of the PMMA polymer transfer method. 1) A 2D flake is exfoliated onto a SiO_2/Si substrate coated in a layer of PVA and PMMA. 2) A circle is etched into the PMMA around the flake using a scalpel. 3) The substrate and flake are placed in deionised water, dissolving the PVA. 4) Once the PVA has dissolved, the PMMA holding the flake floats to the surface of the water. 5) The PMMA membrane is fished out of the water using a stainless steel membrane holder (plectrum). 6) The plectrum holding the flake is inverted and aligned with a target flake. 7) The initial flake is brought in contact with the target. 8) The plectrum is slowly lifted and the PMMA detaches from the flake.

As outlined in Fig. 2.9, the PMMA method is optimised for the transfer of a single flake onto a target flake or substrate. Thicker stacks and heterostructures are fabricated by additional transfers, making it much slower than the PDMS method. Furthermore, the steps to attach the PMMA film to the plectrum can be challenging, requiring a high amount of skill compared to the steps in the PDMS transfer. The advantage of the PMMA method, however, is that the PMMA film leaves much less polymer residue compared to PC/PDMS [71], meaning a higher quality sample surface can be achieved, which is particularly beneficial for ARPES.

In the fabrication of twisted structures, there is often a desired twist angle for the final sample, which requires knowledge of the relative orientation of the flakes being twisted. When stacking flakes from different crystals, the orientation must often be inferred from the shape of the flake and direction of straight edges that correspond to crystallographic axes. Unfortunately, the determined orientation can have a high degree of uncertainty which potentially results in a large offset from the desired twist angle. In twisted homostructures, however, an alternative method allows this uncertainty to be mitigated. Known as the tear-and-stack method, a single flake is used to form both the top and bottom layers of the twisted stack by

splitting the flake into two pieces [160]. As they come from the same parent flake, each piece must have the same orientation and, thus, the desired twist angle can be achieved by rotating one piece relative to the other by said angle.

The tear-and-stack method is realised by bringing half of the initial flake in contact with another flake, usually hBN, which it adheres to strongly. Lifting the initial flake away causes it to tear, leaving half attached to the hBN. One of the pieces can then be rotated by the desired twist angle and the two pieces stacked together. The tear-and-stack method can be performed using both the PDMS and PMMA method. In the PDMS-based tear-and-stack method, the hBN is attached to the PDMS stamp and brought in contact with half of the flake of interest. Lifting the stamp then causes the hBN to tear off half of the flake, bringing that piece with it [160]. In the PMMA-based tear-and-stack method, however, the flake of interest is on the PMMA stamp and half brought in contact with the hBN on a substrate. The half on the hBN is then left behind when the stamp is lifted, while the other half stays on the PMMA.

2.3.2   In-situ electrostatic gating

Discussed in Section 1.4, µARPES with *in-situ* gating enables visualisation of the conduction band in semiconducting materials, as well as the study of carrier concentration and field dependent band renormalisation effects [132–134]. Gated samples typically follow a standard geometry that allows them to be studied with ARPES, as shown schematically in Fig. 2.10. A back gate is designed by stacking a flake of hBN, optimally 10–20 nm thick, on top of graphite. The graphite acts as the back gate electrode while the hBN acts as the insulating dielectric layer. The material to be studied is then placed on top of the hBN, isolating it from the underlying graphite. Metal contacts are used to connect to the different parts of the sample, allowing for wire bonding and subsequent connections to voltage and ground terminals. The metal contacts can either be deposited onto the sample using lithography and metal deposition techniques, or the 2D heterostructure is placed directly onto a pre-patterned metal contact design. One metal contact touches the graphite flake, which can be biased by a variable gate voltage, V_G, while the other contact connects to the flake on top of the hBN, grounding it. For semiconducting flakes, a layer of graphene is often used to connect to the ground contact rather than the flake itself as, even when the conduction band is populated, the lateral conductivity of the semiconducting flake can still be low. The graphene thus helps ground the flake, while also giving a better Ohmic contact to the metal.
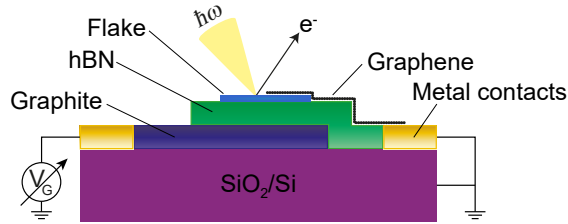
Figure 2.10: Schematic of an example device for µARPES with *in-situ* gating. The flake to be measured is grounded by a layer of graphene connected to a metal contact. An underlying flake of graphite is connected to another metal electrode that can apply a variable gate voltage to the graphite. The graphite and top flake are separated by a hBN dielectric layer.

2.3.3 Template-stripped gold exfoliation

Exfoliation of 2D materials onto standard SiO_2/Si substrates typically produces a low yield of few-layer or thinner flakes when compared to the total exfoliated area. These flakes are also of relatively small lateral size, on the order of 10s of micrometres. As exfoliated 2D materials tend to possess better intrinsic properties over those grown from bottom-up approaches, there is strong interest in identifying substrates that allow for the exfoliation of large area atomically thin flakes. A promising candidate is that of gold thin films, which have been able to achieve exfoliated monolayer flakes with lateral sizes of several millimetres [161, 162]. This is enabled through a strong bonding strength between the gold and van der Waals layers that rapidly decreases with separation, leading to a preferential exfoliation of monolayers [163].

This exfoliation mechanism relies on the gold being clean and atomically flat. Exposure to air and increased surface roughness results in a greatly reduced mono-layer area and an increase of bulk exfoliated flakes [163]. Thermal evaporation or sputtering of gold typically gives an atomically rough surface. Furthermore, exposed gold surfaces prepared in this way must either be used immediately or kept in a controlled environment to prevent contamination prior to exfoliation. A technique that can overcome these issues is that of the template-stripped method [164]. Originally developed in the early 1990s for the study of molecules adsorbed on metal surfaces via STM [165, 166], the template-stripped method has found a more recent use in the exfoliation of large area 2D flakes [167, 168].

Shown schematically in Fig. 2.11, the template-stripped gold method begins by depositing a gold film onto a substrate referred to as the template (1). The idea is that, at the interface, the gold adopts the surface roughness of the template.
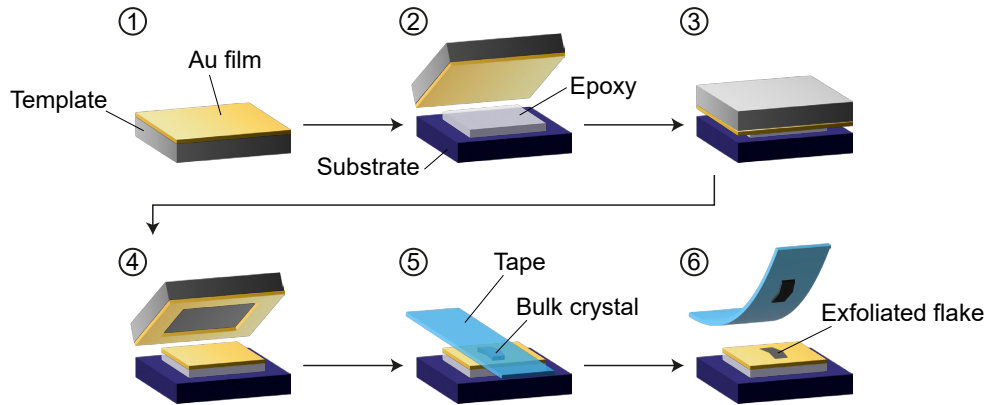
Figure 2.11: Schematic of the template-stripped gold exfoliation method. 1) Gold is deposited onto a clean smooth template surface, such as silicon or mica. 2/3) The gold surface is attached to a support substrate using an adhesive epoxy. 4) The lattice mismatch between the gold and the template creates a weak adhesion, allowing the template to be mechanically cleaved at the gold-template interface. 5/6) 2D material flakes are deposited onto the fresh gold surface using the standard tape-assisted exfoliation method.

Templates such as silicon wafers and mica are commonly used as they can achieve a very smooth surface. The templates must also be cleaned prior to gold deposition to prevent contamination at the interface. Once deposited, however, the templated-Au can be stored in ambient conditions without contamination, due to the buried interface. The next step is to adhere the exposed gold surface to a support substrate using epoxy (2/3). The strong adhesion of the epoxy emphasises a weak point at the gold-template interface due to the lattice mismatch. This allows the template to be mechanically cleaved from the stack, exposing the interfaced gold surface which maintains the surface roughness of the template (4) [164]. In this way, a smooth fresh gold surface is prepared, suitable for the exfoliation of 2D materials (5/6).

2.3.4 Surface preparation for ARPES

The surface sensitivity of ARPES requires samples to have atomically clean surfaces free from contamination. When exposed to air, materials become coated in a thin layer of particles and adsorbates, requiring the surfaces to be prepared in someway for photoemission measurements. In the study of bulk single crystals, samples are commonly cleaved in UHV to obtain a new fresh surface free from contaminants. For exfoliated 2D material samples and heterostructures, however, this isn't possible and the surface must be prepared by a different method. Typically, these surfaces are cleaned by annealing in UHV. The heightened temperatures assist in desorbing

particles from the sample surface which are then removed via the vacuum pumps, gradually cleaning the surface over time.

The twisted graphene samples presented in Chapters 3 and 4 were transferred through air to the I05 nanoARPES beamline, requiring annealing in UHV prior to µARPES measurements. As well as the measurement chamber that houses the sample stage and optics, the nanoARPES endstation has additional UHV chambers, connected by valves, for the loading and preparation of samples prior to experiments. Samples are transferred into UHV from air via a load lock that can be vented to atmospheric pressure and pumped to the 10^{-8} mbar range. Samples can then be annealed within a connecting UHV chamber before being transferred to the measurement chamber. A drawback of UHV annealing is that samples tend to outgas as the temperature is increased. Annealing temperatures must be ramped slowly to limit this outgassing and maintain a good vacuum pressure within the chamber.

Twisted graphene samples were annealed at a measured temperature of 300°C for 3–12 hours depending on the amount of outgassing. For example, the gated twisted graphene samples, as will be seen in Section 4.5, are mounted using a UHV compatible epoxy into bulky sample holders required for *in-situ* gating, resulting in a large amount of outgassing. It was found that cooling samples down when the chamber pressure is at its lowest gives the best possible sample quality, thus, samples that are outgassing more must be annealed for longer to allow the chamber pressure to decrease.

The CrSBr samples presented in Chapter 5 did not require UHV annealing prior to measuring. Discussed in Section 5.2, these samples were fabricated using an *in-situ* exfoliation method, similar to cleaving of bulk crystals in UHV, meaning a fresh surface was achieved that did not require annealing.

Chapter 3

ARPES measurements of few-layer graphene systems

3.1 Introduction

Despite it being almost 20 years since the publication of Geim and Novoselov's Nobel Prize winning paper [1], research surrounding graphene continues to flourish. This is in part to the recent advent of twistronics - lateral rotation (or twisting) of 2D layers relative to one another [11]. For van der Waals crystals with similar lattice parameters, twisting creates a real-space moiré pattern in the crystal lattice – a new long range periodicity, that modulates the underlying electronic structure of the system and can result in new properties absent from the parent materials [67, 169–171]. This garnered particular attention in magic-angle tBG due to the groundbreaking discovery of superconducting and Mott insulating states [9, 10], accessible through tuning of the carrier density by electrostatic doping. Prior theoretical work predicted a flat band at the Fermi level of tBG at these so-called 'magic-angles' [100], whose high density of states gives rise to these correlated phases. Similar phenomena have also been observed in few-layer twisted graphene systems, such as tMBG [101, 102] and tDBG [103, 104], that benefit from larger magic-angles than in tBG. These results presented twisted graphene as a model system to study correlated states, both experimentally and theoretically.

Most experimental studies of twisted graphene use either transport [101, 102], which can easily tune the carrier density and displacement field to access different correlated states, or STM/STS techniques [105, 106], which can probe the local moiré structure. Though effective, these methods are momentum-integrated and do not provide direct information on the electronic dispersions that determine much of

the observed physics in these systems. Conversely, ARPES is momentum-resolved and can directly image the electronic structure of a material. Combined with state-of-the-art synchrotron light sources and focusing optics, μARPES has already been used to investigate interlayer effects in twisted graphene [124, 125, 134]. This is not without difficulty, however. Firstly, the measured ARPES signal is an integration over the sample area illuminated by the photon beam. Twisted structures are known to exhibit a number of lateral defects, including twist angle domains, strain and wrinkles [172]. Care must be taken to ensure the measurement area is uniform, which can often only be inferred from the quality of the ARPES data. Secondly, interpretation of the ARPES spectra is non-trivial. The moiré periodicity is usually incommensurate to that of the individual graphene lattices. This leads to a complex distribution of spectral weight primarily around the original graphene bands [173], with weak features appearing from interlayer interactions. For a detailed comparison with theory, simulation of the ARPES intensity is often required.

The aim of this Chapter is to bridge the gap between ARPES spectra of aligned and twisted graphene systems. Beginning with few-layer aligned graphene, we will identify key features in the ARPES data and the information which can be extracted from these. This is supported by band structure calculations and simulation of the photoemission intensity, validated by comparison to the experimental data. Changes in the ARPES spectra due to a twisted interface will then be explained for three different twisted graphene systems, including how these evolve with twist angle. How the ARPES spectra can be used to determine the twist angle will also be explained, as well as how we can confirm the uniformity of the measurement position.

3.2 ARPES of aligned graphene

Graphene samples were fabricated by Astrid Weston at the National Graphene Institute, University of Manchester, using a PMMA-based transfer method, as described in Section 2.3.1. A schematic of the samples is shown in Fig. 3.1(a). The graphene layers are supported on a flake of hBN to eliminate roughness introduced by the substrate and to isolate it from any lower lying flakes, such as graphite. The twist angle between the graphene and hBN is purposefully made large to reduce moiré effects. For grounding, the sample can either be placed on a conductive substrate, or, in the case shown here, contacted via a metal electrode. The Au electrode has been deposited through a transmission electron microscopy (TEM) grid shadow mask to avoid contamination of the surface introduced through the use of photoresists. An
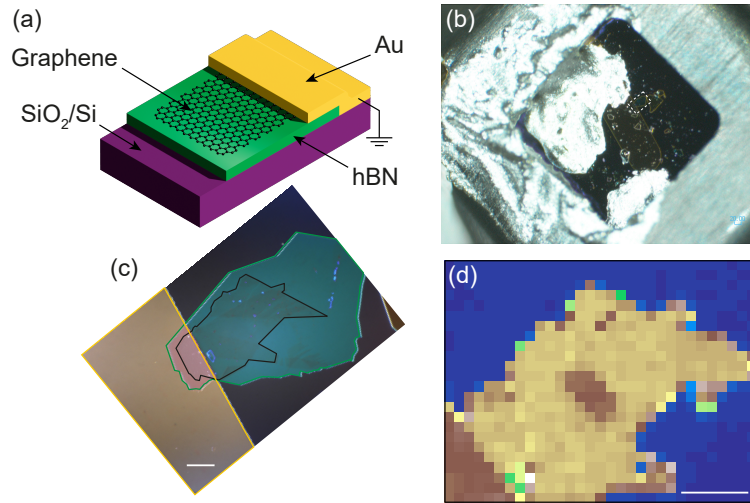
Figure 3.1: a) Schematic of a graphene/hBN heterostructure sample. b) Low-magnification optical image of a few-layer graphene sample, mounted in a nanoARPES beamline sample holder. c) High-magnification optical image of the few-layer graphene sample from the white dashed box in (b). The few-layer graphene (black), hBN (green) and Au electrode (yellow) regions have been outlined. d) SPEM image of the few-layer graphene region in (c). Scale bars are 20 µm.

example of a few-layer graphene sample is shown in Figs. 3.1(b) and (c). As seen in Fig. 3.1(b), silver epoxy has been used to contact the Au electrode with the sample holder frame, which is connected to ground during the experiment. Fig. 3.1(d) shows a SPEM image centred on the few-layer graphene region. The shape of the graphene flake can clearly be seen in the SPEM image, while the surrounding exposed hBN regions show minimal intensity. This is due the hBN becoming charged by the photon beam, which shifts the hBN valence bands outside of the detector energy window, and thus these appear as a minimum in the SPEM image. As will be seen later, stacking the hBN on top of a graphite flake can effectively ground it for thin enough pieces of hBN, on the order of 10s of nanometres allowing it to be seen in SPEM images.

A comparison between the ARPES spectra for monolayer and Bernal-stacked bi-, tetra- and pentalayer graphene is shown in Fig. 3.2. Panels (i) show energy-momentum cuts through the $\mathbf{K}$ point for the different graphene thicknesses, while panels (ii)–(iv) show the corresponding constant energy cuts. Monolayer graphene exhibits the stereotypical singular Dirac cone with a linear dispersion close to the Dirac point, while for the bilayer, the ARPES spectrum shows a pair of cones with an approximately parabolic dispersion close to the peak of the cone. Thicker
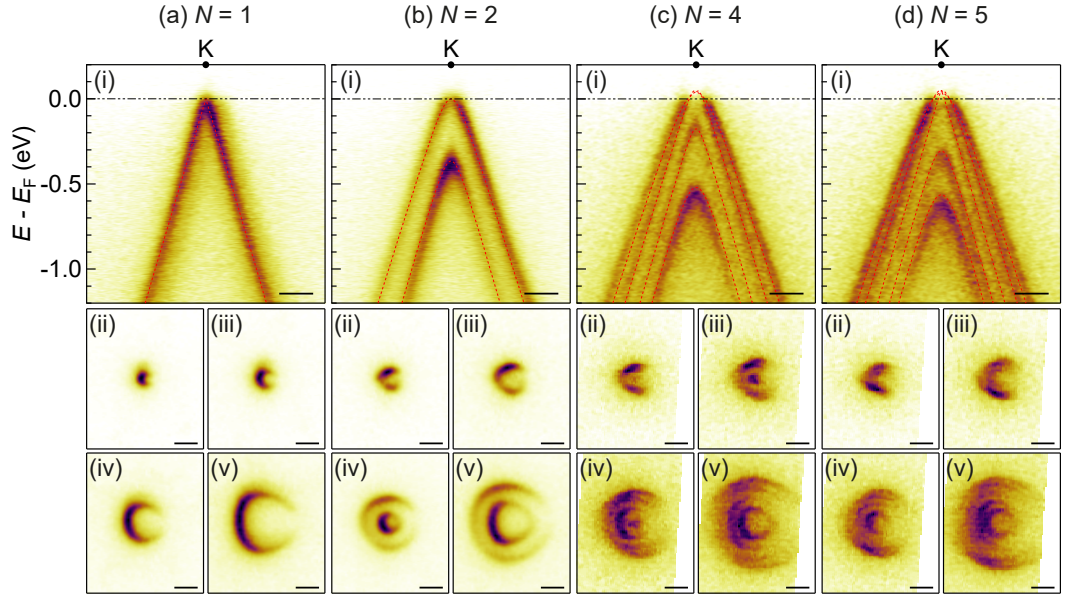
Figure 3.2: a–d) ARPES spectra around the **K** point of (a) monolayer, (b) bilayer, (c) tetralayer and (d) pentalayer graphene, labelled with the number of layers, N. i) Energy-momentum cuts centred on the **K** point of graphene, taken perpendicular to the $\mathbf{\Gamma} \rightarrow \mathbf{K}$ direction of the 1st Brillouin zone. ii–v) Constant energy cuts centred on the **K** point of graphene at $E - E_{\mathrm{F}} =$ (ii) -100 meV, (iii) -200 meV, (iv) -500 meV and (v) -800 meV, averaged over ± 15 meV of the specified energy. Scale bars are 0.1 Å^{-1}.

graphene sheets can be described by a combination of these cones: stacks with an even number of layers possess entirely parabolic cones, while for an odd number of layers they exhibit a singular linear cone in addition to parabolic, where the total number of bands is equal to the number of layers [174, 175]. It should be noted that this trend is only followed for AB-stacked graphene layers. Other stacking orders are known to exist including ABC rhombohedral-stacking [176] and few-layer specific configurations (e.g. ABCB stacking in tetralayer graphene [177]) that exhibit different electronic structures, leading to changes in their optical properties [175, 178, 179].

Importantly, the tetra- and pentalayer bands have been shifted in energy so that the topmost bands are cut off by the Fermi level. This is due to p–doping that most likely comes from surface contamination. This is supported by the increased background observed, suggesting a thin layer on the surface of the graphene that increases the amount of inelastic scattering of photoelectrons, highlighting the importance of a clean surface for ARPES.

Overlaid in red in panels (i) of Fig. 3.2 are the calculated band dispersions, as

γ_0 (eV)	γ_1 (eV)	γ_3 (eV)	γ_4 (eV)
3.16	0.39	0.315	0.07

Table 3.1: The SWM parameters used to model few-layer graphene, taken from [180].

performed by Andrew McEllistrim at the National Graphene Institute, University of Manchester. Note the tetra- and pentalayer bands have been shifted by 50 meV to account for the experimentally observed p–doping. As outlined in Section 1.2.1, the monolayer and bilayer dispersion around the **K** point can be accurately predicted using a tight-binding model [17, 18]. For few-layer graphene, we used a hybrid **k·p**-tight-binding (HkpTB) model [179], which is an effective extension of the bilayer Hamiltonian to account for the additional layers. Underlying both of these are the SWM coupling parameters (Section 1.2.1). The values used for these parameters are shown in Table 3.1, which return the calculated band dispersions in Fig. 3.2 [180]. There is good agreement between the predicted dispersion and ARPES spectra, providing confidence to the validity of the HkpTB model and the SWM parameters used here, which will be important when applying it later to twisted graphene systems.

As mentioned previously, doping in graphene shifts the chemical potential so that the Fermi level lies within the valence cone (p–doping) or conduction cone (n–doping). Doping also plays a role in band renormalisations that subtly change the Dirac cone dispersion [111, 113, 181, 182]. Accurately knowing the amount of doping present is important for quantifying these band structure changes. The doping, as well as other relevant parameters, can be extracted by fitting the measured ARPES spectra to the low-energy graphene dispersions, as derived in Section 1.2.1. Figs. 3.3(a) and (b) show this for monolayer and bilayer graphene, respectively. The band positions (black data points) were determined by fitting momentum distribution curves (MDCs) to Lorentzian functions and extracting the peak centre. The dispersions (red lines) were fitted over the energy range -3–0 eV, where the low-energy dispersion approximation is expected to hold.

For the monolayer graphene shown, Eq. (1.2.9) returned a Dirac energy of $E_D^{ML} = 33 \pm 2$ meV, and a Fermi velocity of $v_F = (1.09 \pm 0.02) \times 10^6$ m s^{-1}. The non-zero E_D^{ML} demonstrates a small but notable amount of doping present in the monolayer graphene, presumably from contamination on and between the layers, while the reported value for v_F is reasonable for graphene on hBN [114, 183]. An equation for the charge carrier density, n_{ML}, can be derived from the density of states using $\int_{E_F}^{E_D^{ML}} \rho_{ML} dE$. Note, this applies for p–doped graphene, whereas for

49

n–doping the limits of integration are reversed. Setting $E_F = 0$ returns the result

$$n_{\text{ML}} = \frac{(E_{\text{D}}^{\text{ML}})^2}{\pi v_{\text{F}}^2}. \tag{3.2.1}$$

From the extracted parameters, Eq. (3.2.1) gives a value of $n_{\text{ML}} = (6.7 \pm 0.9) \times 10^{10}$ cm^{-2}.

For fitting the bilayer graphene, the parameters v and γ_1 are very dependent on the shape of the dispersion near E_F, which is poorly defined from MDCs. This makes fitting difficult when allowing both of these parameters to vary freely. Instead, it is easier to hold one constant while letting the other vary. Here, we set $\gamma_1 = 0.39$ eV to match the value used previously for the calculated band dispersions in Fig. 3.2. This gave $E_{\text{D}}^{\text{BL}} = 6 \pm 1$ meV and $v = (1.02 \pm 0.02) \times 10^6$ m s^{-1}. Most notably, this value of v is in good agreement with our chosen parameter set (Table 3.1) and justifies our choice for the value of γ_1. The charge carrier density for bilayer graphene can similarly be derived from the density of states (Eq. (1.2.13)), giving the equation [17]

$$n_{\text{BL}} = \frac{\gamma_1 E_{\text{D}}^{\text{BL}}}{\pi v^2}, \tag{3.2.2}$$

which, from the extracted parameters, returns $n_{\text{BL}} = (1.7 \pm 0.3) \times 10^{11}$ cm^{-2}. Within uncertainty, this is twice the value determined for the monolayer graphene and, as such, they have the same carrier density per layer. The monolayer and bilayer graphene data shown were taken from the same sample, so it is expected that they would exhibit similar levels of doping induced by contamination.

As mentioned above, the fitting was performed over a small energy range close to E_F where the low-energy dispersions are relevant. Extrapolating these fits to higher binding energies shows the band dispersions diverging away from the approximate fitting due to trigonal warping (Section 1.2.1). Additionally, this extrapolation reveals a small amount of asymmetry in the band dispersions at high binding energy. This likely comes from the extracted energy-momentum cuts not being exactly perpendicular to the $\mathbf{\Gamma} \rightarrow \mathbf{K}$ direction, and so the degree of trigonal warping on either side of the cone is different. This ultimately comes from uncertainty in the position of $\mathbf{\Gamma}$ when transforming the data from angle-space to reciprocal space. Due to the large BZ of graphene, it can be difficult to take a single measurement with both $\mathbf{\Gamma}$ and $\mathbf{K}$ included. As such, when aiming to measure around the $\mathbf{K}$ point of graphene, $\mathbf{\Gamma}$ must often be inferred from features in the ARPES spectra, increasing the amount of uncertainty.

Discussed in Sections 1.4 and 2.1.2, ARPES can be used to study many-
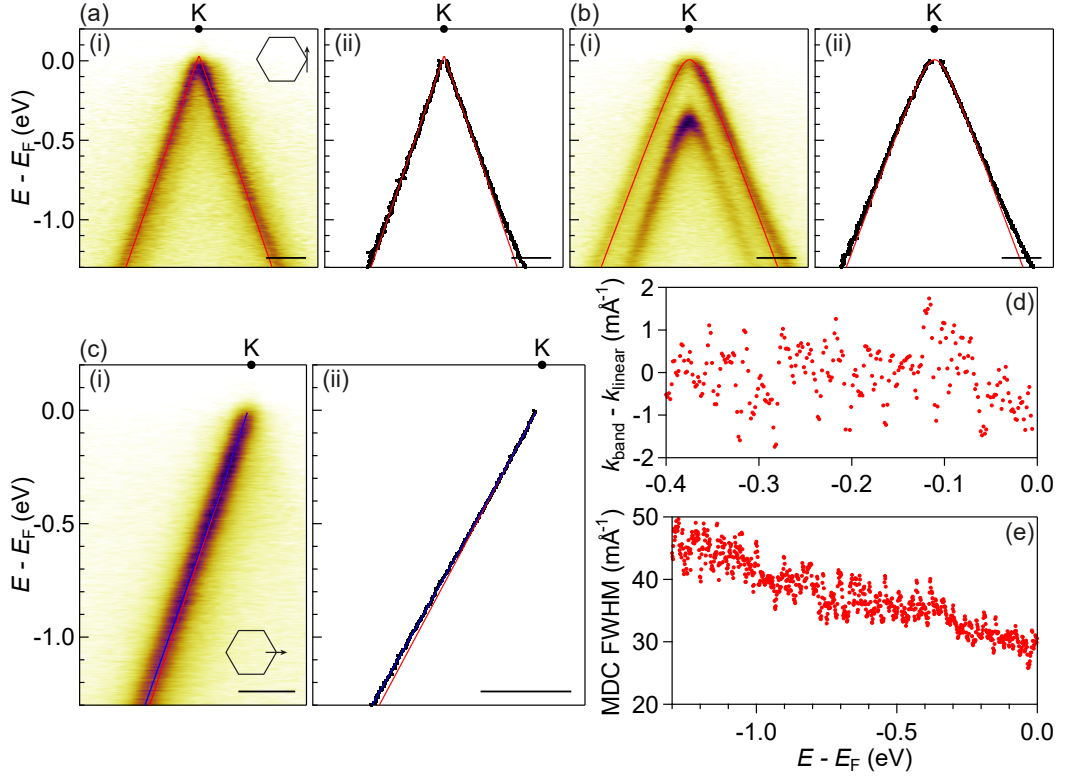
Figure 3.3: a,b) Monolayer and bilayer graphene dispersions, respectively, perpendicular to the $\mathbf{\Gamma} \to \mathbf{K}$ direction. c) Monolayer graphene dispersion along the $\mathbf{\Gamma} \to \mathbf{K}$ direction. Panels (i) show measured ARPES energy-momentum cuts. Data points in (ii) are band positions extracted from fitting to MDCs. Red lines are fits to the data points over the energy range -3–0 eV using the low energy dispersion approximations for graphene (Section 1.2.1). Blue line fit in (c) includes a logarithmic self-energy correction and is fitted over the full data range. Scale bars are 0.1 Å^{-1}. d) Difference in k between the extracted band positions in (c) and a linear function. e) Lorentzian widths extracted from Voigt fits to MDCs of the ARPES data in (c).

body interactions within a material that lead to renormalisation of the bare-band dispersion. In graphene, electron-electron (e–e) interactions are known to modify the band velocity of the Dirac cone [114, 182], while electron-phonon (e–ph) interactions introduce a kink into the Dirac dispersion [111, 113, 181]. Starting with the first of these, the e–e interaction is expected to introduce a logarithmic correction to the linear bare-band dispersion of the form $\frac{\alpha}{4} v_{\mathrm{F}}^0 |k - k_{\mathrm{F}}| \ln |\frac{k_{\mathrm{D}}}{k_{\mathrm{D}} - k}|$, where k_{F} is the Fermi wavenumber along $\mathbf{\Gamma} \to \mathbf{K}$, $k_{\mathrm{D}} = 1.703$ Å^{-1} is the Dirac point wavenumber, and α is the graphene fine structure constant [18, 184]. Fitting of this to the graphene dispersion along $\mathbf{\Gamma} \to \mathbf{K}$ is shown in Fig. 3.3(c). The red line is a linear fit that diverges from the extracted band dispersion at high binding energy, while the blue

line fit containing the logarithmic correction matches well to the data points. From the corrected fit, we obtain a band velocity of $v_{\mathrm{F}}^0 = (1.03 \pm 0.02) \times 10^6 \ \mathrm{m\,s^{-1}}$, slightly less than the Fermi velocity from the low-energy fitting, and a fine structure constant of $\alpha = 0.088 \pm 0.008$. This value for α is very small, much smaller than previous reports for graphene on hBN [183, 185], and suggests minimal deviation from the bare-band dispersion due to e–e interactions.

Electron-phonon interactions create a kink in the Dirac cone dispersion close to E_{D}, predominantly seen for highly n–doped graphene [111, 113, 114]. To see if this is present in the graphene dispersion in Fig. 3.3(c), we subtracted a linear function from the measured band positions (Fig. 3.3(d)) which should produce a peak at the energy of the kink. However, no obvious peak is visible and the data shows random noise. From first principle calculations, it is expected that the kink should only become noticeable at doping levels on the order of 10^{12} cm^{-2} [181], at least an order of magnitude higher than what is displayed here. Together with the minimal deviations due to e–e interactions, this shows that there are minimal band renormalisation effects present in our graphene samples, and that the measured dispersion is well described by the tight-binding model.

Note, some evidence of many-body effects is still apparent in the MDC linewidths. The observed broadening has both a Gaussian component, that comes from experimental factors such as energy resolution and sample quality, and a Lorentzian component, that depends on many-body interactions [114]. The Lorentzian component is equal to the imaginary part of the electron self-energy (Section 2.1.2) [111] and can be determined from the ARPES data by fitting of a Voigt function [186]. Fig. 3.3(e) shows the measured Lorentzian widths. A Gaussian width of 60 meV was fixed in the Voigt function to match the empirically determined broadening used later in simulations of the ARPES spectra. The data in Fig. 3.3(e) shows a roughly linear dependence with binding energy, as expected for e–e interactions [114, 182, 187]. For simplicity, these effects are not included in later models of the ARPES data, as they are not required to understand the features of interest.

Returning to the constant energy cuts in panels (ii)–(v) of Fig. 3.2, a signature feature in the ARPES spectra of monolayer graphene when using linearly polarised light is the so-called dark corridor [188]. This can be seen in Fig. 3.2(a) panels (ii)–(v) as a suppression of the photoemission intensity on the side of the Dirac cone facing away from $\mathbf{\Gamma}$, giving the stereotypical horseshoe shape. The dark corridor is a matrix element effect that comes from interference between photoelectrons emitted from the different graphene sublattice sites [189]. The appearance of

the dark corridor is heavily dependent on the polarisation, however, and it has been shown that it is possible to restore this intensity under specific conditions [190]. While the intensity distribution for the monolayer cone appears symmetric either side of the $\mathbf{\Gamma} \to \mathbf{K}$ axis, the constant energy cuts for the other graphene thicknesses show much more variation. This is particularly evident for the bilayer, where the bands appear more intense on one side of the cone than the other. Similarly, this unequal distribution of spectral weight makes the tetra- and pentalayer constant energy cuts look distorted.

To understand the origins of this intensity variation, it is useful to simulate the ARPES spectra. This follows a similar approach to the photoemission model described in Section 2.1.2 [26, 140]. The initial state electron, Ψ_i, is modelled as a Bloch wave that comprises on-layer and sublattice components, while the electron final state, Ψ_f, is assumed to be a plane wave. By ignoring dynamical effects, the ARPES intensity can be written as

$$I \propto |\mathbf{A} \cdot <\Psi_f|\nabla_{\boldsymbol{k}}\mathcal{H}|\Psi_i>|^2 \, \delta(E_{\text{kin}} + \Phi - E_i - \hbar\omega), \qquad (3.2.3)$$

where the interaction Hamiltonian now includes the tight-binding Hamiltonian for the respective graphene system from the substitution $\mathbf{p} \sim \nabla_{\boldsymbol{k}}\mathcal{H}$. The Bloch wave components can be solved by diagonalising the Hamiltonian and solving for the different wavefunctions. This leads to wavefunction coefficients, $c_{l,X}$, for each lattice site, where l denotes the layer number (starting from the topmost layer) and $X = \{A, B\}$ are the sublattice sites. Additionally, to account for the observed energy broadening in the ARPES spectra, the delta function is changed to a Lorentzian, $\mathcal{L}(...)$, whose width (60 meV) is set to match the experimental broadening [26, 125]. Eq. (3.2.3) thus becomes

$$I \propto \left|\sum_{l=1}^{N}(c_{l,A} + c_{l,B}) * F^{l-1}\right|^2 \mathcal{L}(...), \qquad (3.2.4)$$

where N is the total number of graphene layers.

The term $F = A_z e^{(iK_z \cdot d)}$ in Eq. (3.2.4), where d is the graphene layer spacing, comes from the out-of-plane component of the final state electron. Treated as a plane wave, the photoemitted electron propagates through the material to the vacuum with a phase factor given by F, which is dependent on the out-of-plane momentum and the number of layers travelled through. While in the crystal, the final state wavefunction is damped [191], which we capture through an attenuation factor, $A_z = 0.4$, whose value was determined by comparison to experimental results. The
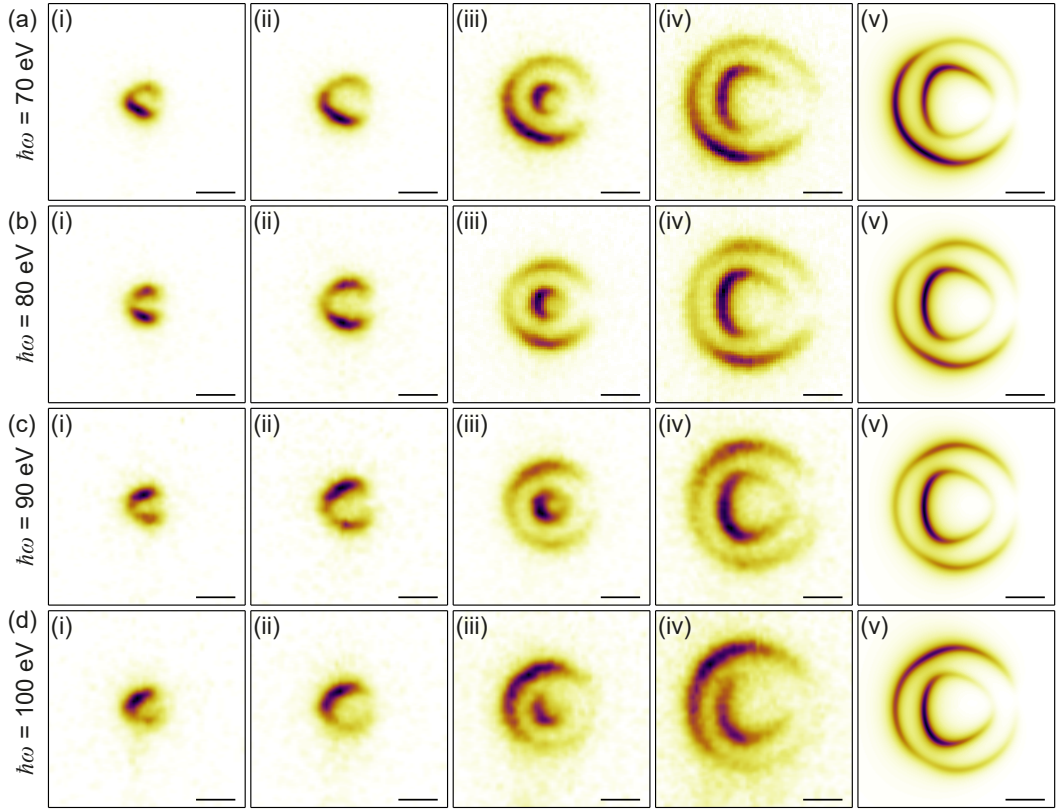
Figure 3.4: a–d) Bilayer graphene ARPES constant energy cuts taken at photon energies (a) 70 eV, (b) 80 eV, (c) 90 eV and (d) 100 eV. i–iv) Experimental constant energy cuts centred on the **K** point of graphene at $E - E_{\mathrm{F}}$ = (i) -100 meV, (ii) -200 meV, (iii) -500 meV and (iv) -800 meV, averaged over ± 15 meV of the specified energy. v) Simulated constant energy cuts at $E - E_{\mathrm{F}} = -800$ meV. Scale bars are 0.1 Å^{-1}.

final state momentum is related to the photoelectron kinetic energy by

$$E_{\mathrm{kin}} = \hbar^2 \frac{K_z^2 + K_\parallel^2}{2m_e} = \hbar\omega - \Phi - |E_B|, \tag{3.2.5}$$

as defined in Section 2.1.1 [140]. This can be rearranged to give

$$K_z = \sqrt{\frac{2m_e}{\hbar^2}\left(\hbar\omega - \Phi - |E_B|\right) - K_\parallel^2}. \tag{3.2.6}$$

By substituting back into F, one can see that the photoelectron phase clearly depends on the photon energy and initial state binding energy. From Eq.(3.2.4), this variation in F can thus be expected to cause a change in the measured photoemission intensity from different parts of the ARPES spectrum, which will vary as a

function of incident photon energy.

Fig. 3.4 shows constant energy cuts for bilayer graphene taken at different photon energies. As expected, there is a clear change in the intensity distribution with differing photon energy. Between 70 eV and 100 eV, the ARPES intensity is almost inverted across the k_x–axis. Panels (v) in Fig. 3.4 are taken from simulated ARPES spectra of bilayer graphene, using the model described previously. There is good qualitative agreement between the simulated and experimental results, despite the basic approach to the model. The observed agreement helps validate our choice of model and provides confidence for subsequent results when applying it to twisted graphene systems. It should be noted that, to achieve a good agreement, the simulations had to be performed at the $\mathbf{K_-}$ valley. Simulations from the $\mathbf{K_+}$ valley appear similar but are mirrored in the $\mathbf{\Gamma \to K}$ axis. During the experiment, it is hard to know which valley is being measured from without prior knowledge of the intensity distribution given by theory, and so, the $\mathbf{K}$ valleys we have acquired ARPES spectra from are arbitrary.

3.3 ARPES of twisted graphene

We have used ARPES to study three distinct few-layer twisted graphene stacking arrangements: twisted bilayer graphene (tBG), twisted monolayer-bilayer graphene (tMBG) and twisted double-bilayer graphene (tDBG). Ball-and-stick schematics of these are shown in Fig. 3.5. These systems are comprised of a top and bottom layer separated by a twisted interface with a relative twist angle, θ, between them. Each top and bottom layer may contain more than one graphene sheet, but within each layer the graphene is aligned in the AB-stacking configuration, such that there is only one twisted interface. In fact, the whole system is AB-stacked, such that, if $\theta = 0$, the system will resemble AB-aligned graphene. Colours black and blue are used to denote the top and bottom layers, respectively.

It is important to note that, under these rules, tMBG can have two configurations depending on which graphene layer is on top. When isolated, these two configurations are equivalent for the purposes of modelling electronic structure, as the designations 'top' or 'bottom' are arbitrary. The specific stacking arrangement becomes important when the direction becomes defined, either through application of a displacement field [101] or by interaction with a substrate [124]. The stacking arrangement can also be distinguished by ARPES as they will have different intensity distributions due to the multilayer effects described by F in the previous section. To denote between different configurations we introduce the labelling con-
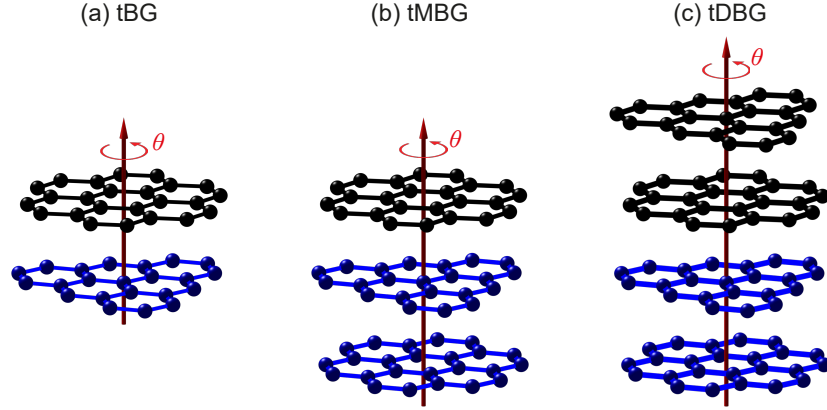
Figure 3.5: a–c) Schematics of twisted bilayer graphene (tBG), twisted monolayer-bilayer graphene (tMBG) and twisted double-bilayer graphene (tDBG), respectively.

vention $i+j$, where i and j describe the number of graphene sheets in the top and bottom layer, respectively, and the plus sign denotes the twisted interface. The two configurations for tMBG can thus be written as 1+2 to signify the monolayer being on top of the bilayer, and vice versa for 2+1. tBG and tDBG can similarly be written as 1+1 and 2+2, respectively, and we will refer to these systems using both short-hands. This convention can be expanded to include more complex twisted stacking arrangements, such as 1+1+1 to describe a trilayer system with 2 twisted interfaces, but this goes beyond the scope of this thesis.

Fig. 3.6 outlines the general layout of our twisted graphene samples for the case of tDBG. This follows the same arrangement as the samples in Fig. 3.1, but now with twisted graphene layers rather than aligned. In this particular example the hBN and graphene layers are also supported on a flake of graphite, and the whole stack is on a platinum-coated silicon substrate to ground the entire sample. These have been fabricated using a PMMA-based tear-and-stack technique (Section 2.3.1) performed by Astrid Weston. Fig. 3.6(a) shows an optical image of the tDBG sample with the different flakes outlined. While the graphite and hBN flakes can be easily seen by eye, there is little contrast to allow identification of the graphene layers. AFM images (Figs. 3.6(b) and (c)) are often better for visualising these types of samples and offer more contrast for thin flakes compared to optical images. Fig. 3.6(c) shows an AFM topography image after two regions have been AFM brushed, where an AFM tip is used to move contamination on and in-between the surfaces of 2D stacks [72]. Though marked by the arrows, these regions can be identified by the buildup of bubbles and contamination into a roughly square shape around the edges of the brushed areas. This increases the uniformity of the area,
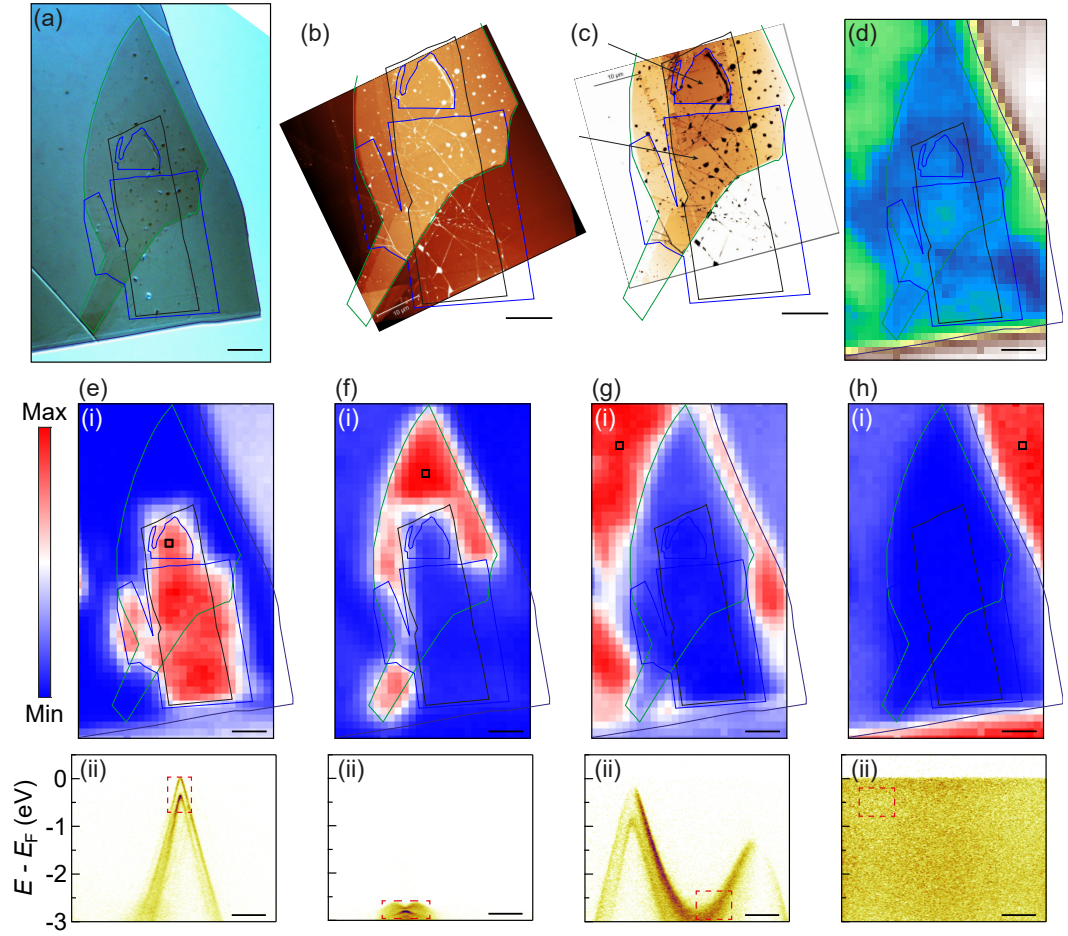
Figure 3.6: a) Optical image of a tDBG sample. The top bilayer (black), bottom bilayer (blue), hBN (green) and graphite (indigo) regions have been outlined. The whole sample is on a platinum-coated silicon substrate. b,c) AFM topography images of the sample in (a). (c) is after two regions have been AFM brushed, marked by arrows. d) SPEM image of the sample in (a). e–h) Spatial analysis of (d) highlighting the (e) twisted graphene, (f) hBN, (g) graphite and (h) metal regions. i) SPEM images obtained by integrating over the red dashed box regions in (ii) for each point in (d). ii) ARPES spectra from the position marked by the black box in (i).

improving the quality of the ARPES spectra.

Fig. 3.6(d) shows a SPEM image of the sample in Fig. 3.6(a). Due to being on a conductive substrate, the whole sample provides intensity to the SPEM image, in contrast to the image in Fig. 3.1(d) where only the grounded graphene region was visible. This can make the SPEM image more difficult to interpret, as the contrast comes from the total detected intensity for each position, which is heavily
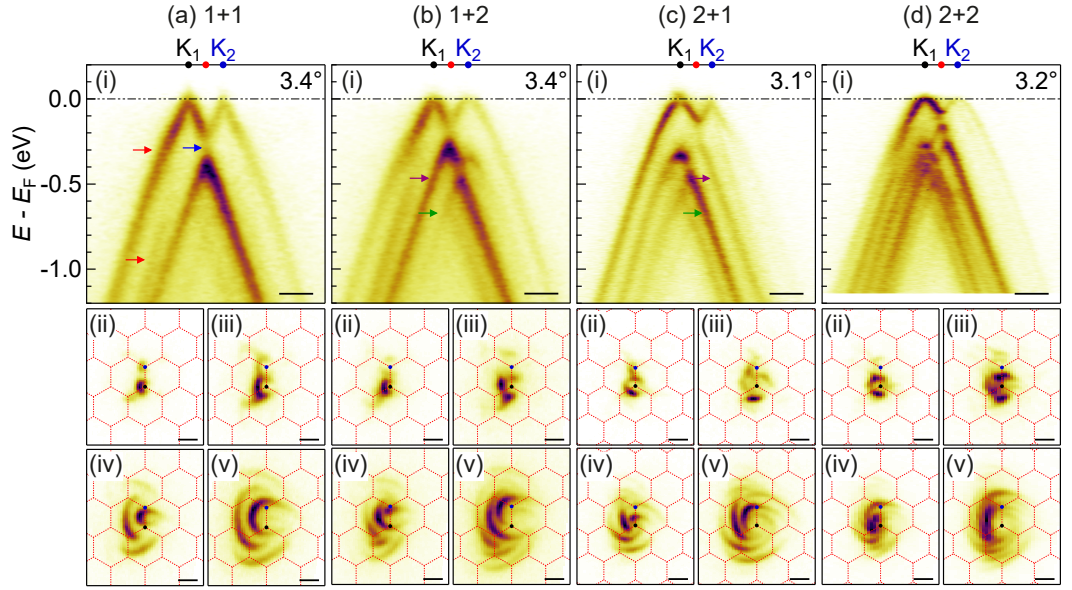
Figure 3.7: a–d) ARPES spectra around the **K** points of (a) 1+1, (b) 1+2, (c) 2+1 and (d) 2+2 twisted graphene at the specified twist angle. i) Energy-momentum cuts taken along the $\mathbf{K_1} \rightarrow \mathbf{K_2}$ direction. Arrows mark features discussed in the main text. ii–v) Constant energy cuts centred on the $\mathbf{K_1}$ and $\mathbf{K_2}$ points of twisted graphene at $E - E_F =$ (ii) -100 meV, (iii) -200 meV, (iv) -500 meV and (v) -800 meV, averaged over ± 15 meV of the specified energy. Red dotted lines show the mBZs. Scale bars are 0.1 Å^{-1}.

dependent on the part of reciprocal space being probed and the general cleanliness and uniformity of different regions. However, as described in Section 2.2.2, the SPEM image comes from a 4D dataset containing an $I(E, k)$ detector image for each (x, y) position. By selecting a specific region in (E, k) containing a particular band, we can enhance different parts of the SPEM image. This is shown in Figs. 3.6(e)–(h), where each flake is individually highlighted. Note that only the exposed parts of each flake become visible, as the intensity from the encapsulated regions is attenuated. This provides an effective method to identify different parts of the sample, which can be particularly useful during an ARPES experiment to quickly find regions of interest.

A comparison between 1+1, 1+2, 2+1 and 2+2 twisted graphene at similar twist angles (3.1–3.4°) is shown in Fig. 3.7. Panels (i) show energy-momentum cuts for the different twisted graphene systems, taken through the $\mathbf{K_1}$ (top layer) and $\mathbf{K_2}$ (bottom layer) points of the mBZ, following the convention outlined in Section 1.3.1. Additionally, panels (ii)–(v) show constant energy cuts overlaid with the mBZs (red dotted lines).

Focusing initially on tBG/1+1, at low binding energies, we can characterise the observed bands as two separate Dirac cones. These come from the top and bottom monolayer graphene sheets, separated in momentum space due to the twist angle between them. The band belonging to the bottom layer appears fainter due to attenuation of the photoemission intensity by the top layer. We will refer to these collectively as the primary bands. Going to higher binding energies, a hybridisation gap opens where the primary bands anti-cross (blue arrow). In addition to this, slight kinks in the Dirac cone dispersion can be seen, as well as the appearance of additional bands (red arrows). These are replica bands coming from scattering by the moiré potential, more easily seen in the constant energy cuts where they are centred on the mBZ corners. Also from the constant energy cuts, we can see that the replica bands hybridise with the primary bands, showing that the replicas come from an initial state and are not a final state effect such as for photoelectron diffraction [192]. The relative intensity of these features and the size of the hybridisation gaps is dependent on the interlayer coupling strength between the top and bottom layers [126]. How this can be quantified and compared with theory will be discussed in more detail in Chapter 4.

On going from 1+1 to 1+2, the bands at $\mathbf{K_2}$ can be seen to change to a bilayer cone, with similar attenuation to the $\mathbf{K_2}$ monolayer cone in 1+1. This has the subsequent effect of increasing the number of replica bands and adding to the overall complexity of the observed spectra. There is also an additional hybridisation gap opened from overlap of the primary bands. This trend continues for the 2+2 case where both primary bands are now bilayer-like, further increasing the total number of bands and hybridisation gaps. The intensity of the bottom layer primary bands are also fainter compared to that in the 1+1 and 1+2 cases, due to the increased attenuation of photoelectrons from having to pass through two graphene layers as opposed to one. This is similarly seen for 2+1 where the monolayer cone from the bottom layer is fainter than for 1+1.

As expected, the ARPES intensity distribution for 2+1 is different to that of 1+2. For example, purple and green arrows in panel (i) of Figs. 3.7(b) and (c) mark similar bands from the two cases. The purple band is much more intense than the green for 1+2, whereas the relative intensity is reversed for 2+1. These differences make it difficult to directly compare the two spectra. This complexity is shown further in the constant energy cuts, where intricate swirling patterns emerge at high binding energies. This highlights the need to simulate the ARPES spectra of these twisted graphene systems in order to understand the origins of these features, which will be discussed shortly.
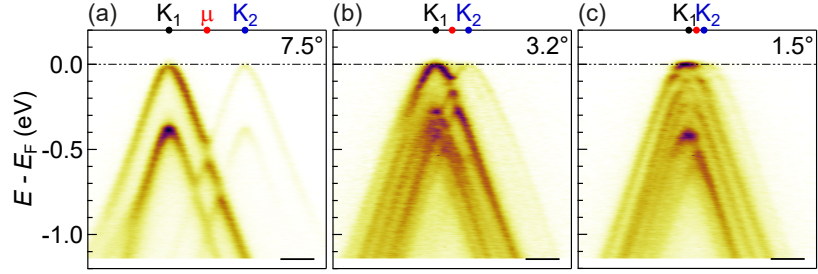
Figure 3.8: a–c) Energy-momentum cuts taken along the $\mathbf{K_1} \to \mathbf{K_2}$ direction for tDBG at twist angles (a) 7.5°, (b) 3.2° and 1.5°. Scale bars are 0.1 Å^{-1}.

To demonstrate the band structure evolution of twisted graphene on changing the twist angle, Fig. 3.8 shows energy-momentum cuts for tDBG in three different twist angle regimes. For relatively large twist angles (Fig. 3.8(a)) the primary bands are spaced far apart in momentum space and only interact at high binding energies. As such, the influence of the replicas is also only seen at high binding energies and the low energy band structure mostly resembles that of the individual graphene layers. As the twist angle is reduced, the $\mathbf{K}$ points come closer together and the mBZ shrinks, increasing the influence of the replicas on the primary bands. Eventually this enters an intermediate regime (Fig. 3.8(b)) where the replicas are very pronounced and less of the band structure resembles that of aligned graphene, but it is still possible to identify the primary bands close to E_F. It is noticeable that, between Figs. 3.8(a) and (b), the topmost band at μ moves closer to E_F, and the bandwidth of the top valence band between $\mathbf{K_1}$ and $\mathbf{K_2}$ shrinks considerably. This shrinking of the bandwidth ultimately results in the formation of the flat band at small twist angles, that has sparked so much interest in twisted graphene [9, 10, 94, 100]. Fig. 3.8(c) shows the closest we have been able to achieve from ARPES to what could be considered a flat band. In this small angle regime, the ARPES spectra becomes very complex and it is almost impossible to discern which are primary and which are replica bands. An intense, highly non-dispersive band is seen at E_F, separated from the lower lying states. A more detailed discussion into the properties of this band will be presented later in Section 4.4.

To model the electronic structure of these different twisted graphene systems, a HkpTB model was applied as used previously for few-layer aligned graphene. This can be done by constructing a Hamiltonian that describes the top and bottom layers and the coupling across the twisted interface. An example of this for tBG is as follows:

$$\mathcal{H}_{\text{tBG}} = \begin{pmatrix} \mathcal{H}_{\text{MLG},t} & \mathcal{T} \\ \mathcal{T} & \mathcal{H}_{\text{MLG},b} \end{pmatrix}. \tag{3.3.1}$$

Here, the tBG Hamiltonian has been constructed from the individual Hamiltonians for the top and bottom layers (both monolayer graphene in this case). The t and b labels specify if the layer is on the top or bottom, respectively, and account for the relative displacement of the **K** points in reciprocal space due to the twist angle. $\mathcal{T}$ is a 2 x 2 matrix that couples the graphene layers across the twisted interface, taking into account only the nearest neighbour hopping. In the case of 1+2 graphene, one could imagine changing the bottom layer Hamiltonian to be that of bilayer graphene. $\mathcal{T}$ would then couple the top monolayer graphene sheet with the topmost graphene sheet from the bilayer. The twisted graphene Hamiltonian can then be used as before to calculate the band structure. For more information, we refer the reader to refs [100, 125, 193, 194]. Similarly, the ARPES spectra can be simulated in the same way as for aligned graphene using Eq. (3.2.4), where the newly computed $c_{l,X}$ now reflect the twisted nature of the system.

Again, to gauge the accuracy of this model, we compared measured and simulated ARPES spectra of 3.4° 1+1 (Fig. 3.9) and 1+2 (Fig. 3.10) twisted graphene at different photon energies. Panels (i)–(iv) show constant energy cuts for the two twisted graphene systems. At low binding energies, where the cones are still separated from each other in reciprocal space (panels (i) and (ii)), the changes in intensity with photon energy are similar to if the layers were isolated. The monolayer intensity distribution shows almost no change with photon energy, while the bilayer shows similar behaviour to that in Fig. 3.4. At higher binding energies (panels (iii) and (iv)) the changes in intensity become more complex and it is difficult to describe a general trend. The simulated constant energy cuts well describe the shape of the experimental data and how far from the **K** points the intensity extends. However, the relative intensity distribution at different photon energies does not show perfect agreement. This is particularly evident for the central left-most band in panels (iii) and (iv). Interestingly, an offset of 10 eV to the photon energy improves this agreement, i.e. (a.iii) agrees better with (b.iv), (b.iii) agrees better with (c.iv), etc. The origin of this 10 eV offset is unknown, but we speculate that it could come from the combined use of the HkpTB model with the assumptions used in the photoemission model in Eq. (3.2.4), which result in a missing contribution to the photoelectron final state momentum. Nevertheless, the qualitative agreement between the experiment and theory is adequate, particularly at 90 eV, which corresponds to the photon energy used for the remaining twisted graphene data.

Panels (v) of Figs. 3.9 and 3.10 show energy-momentum cuts of the two twisted graphene systems at different photon energies. Changes in the intensity of the different bands have a large effect on the appearance of particular features. For
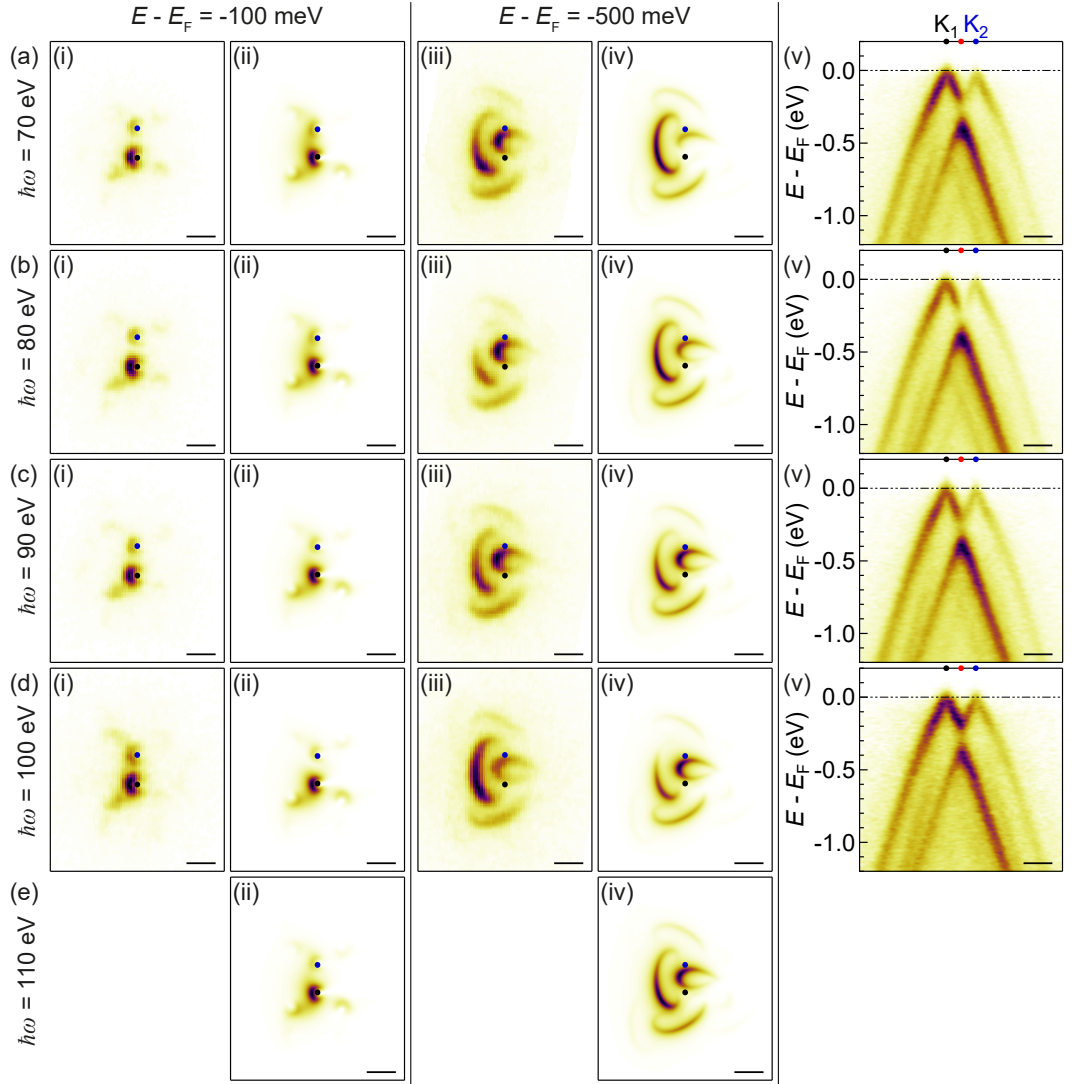
Figure 3.9: a–d) 3.4° 1+1 twisted graphene ARPES constant energy and energy-momentum cuts taken at photon energies (a) 70 eV, (b) 80 eV, (c) 90 eV, (d) 100 eV and (e) 110 eV. i,ii) Experimental and simulated constant energy cuts centred on the $\mathbf{K_1}$ and $\mathbf{K_2}$ points of twisted graphene at $E - E_F = -100$ meV, respectively. iii,iv) Experimental and simulated constant energy cuts centred on the $\mathbf{K_1}$ and $\mathbf{K_2}$ points of twisted graphene at $E - E_F = -500$ meV, respectively. Experimental constant energy cuts were averaged over ± 15 meV of the specified energy. v) Experimental energy-momentum cuts taken along the $\mathbf{K_1} \rightarrow \mathbf{K_2}$ direction. Scale bars are 0.1 Å^{-1}.

example, replica bands at high binding energy are much more visible in the 70 eV and 80 eV data compared to the 90 eV and 100 eV. The hybridisation gaps also become much more obvious when the intensity is positioned around the avoided
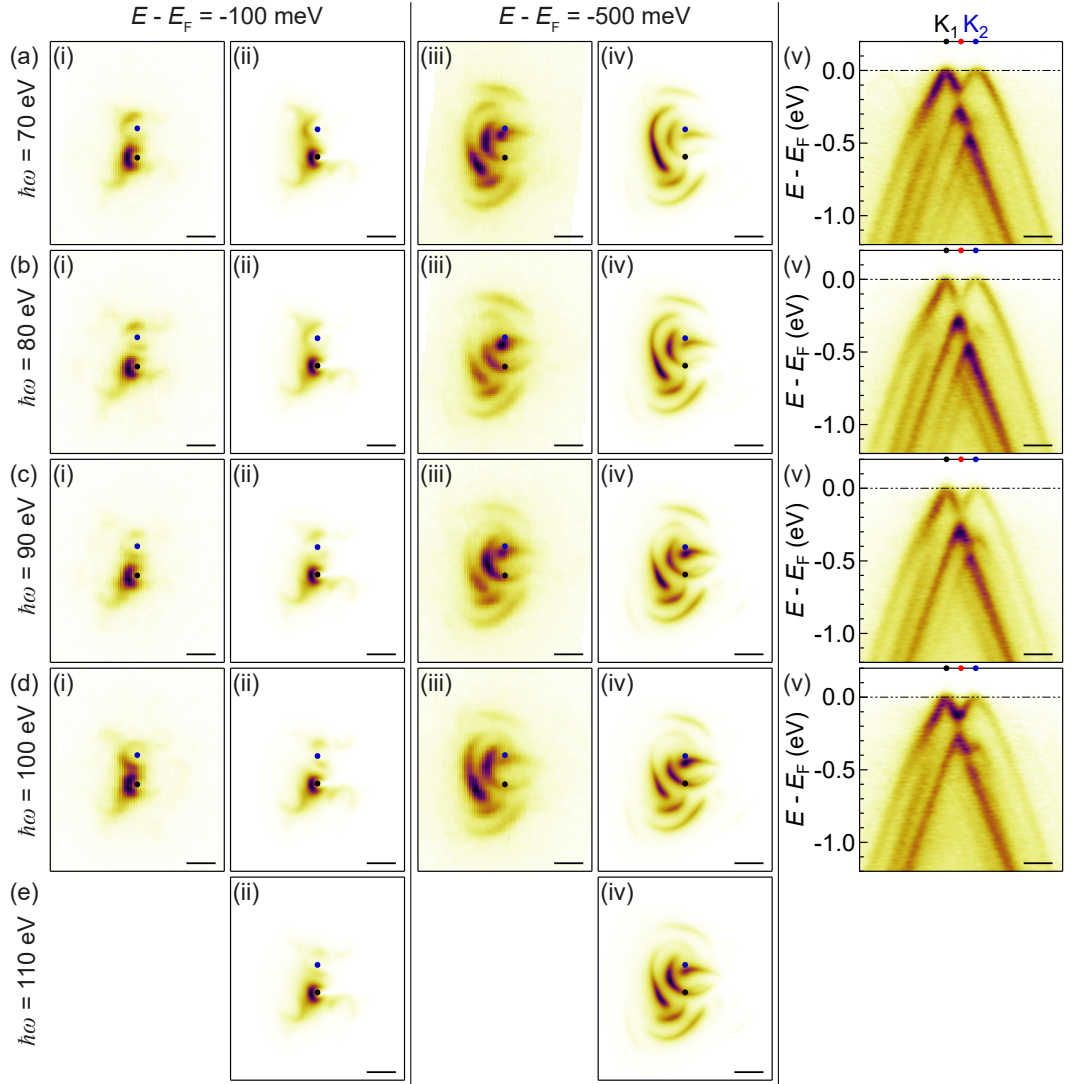
Figure 3.10: a–d) 3.4° 1+2 twisted graphene ARPES constant energy and energy-momentum cuts taken at photon energies (a) 70 eV, (b) 80 eV, (c) 90 eV, (d) 100 eV and (e) 110 eV. i,ii) Experimental and simulated constant energy cuts centred on the $\mathbf{K_1}$ and $\mathbf{K_2}$ points of twisted graphene at $E - E_\mathrm{F} = -100$ meV, respectively. iii,iv) Experimental and simulated constant energy cuts centred on the $\mathbf{K_1}$ and $\mathbf{K_2}$ points of twisted graphene at $E - E_\mathrm{F} = -500$ meV, respectively. Experimental constant energy cuts were averaged over ±15 meV of the specified energy. v) Experimental energy-momentum cuts taken along the $\mathbf{K_1} \to \mathbf{K_2}$ direction. Scale bars are 0.1 Å^{-1}.

crossings. It is thus important to consider what photon energy is best to use when trying to investigate interaction effects in twisted graphene.

3.4 Determining twist angles and sample uniformity

So far, twist angles have been given without explaining how they are determined. Though the two layers can be rotated by a high degree of accuracy during fabrication, the target twist angle can be difficult to achieve. Forces applied during the various stacking stages can result in the flakes moving relative to each other, changing the twist angle and introducing tears and wrinkles across the different layers that affect the sample uniformity [172]. As will be seen, a single twisted sample can contain regions of different twist angles. Thus, it is important to measure the local twist angle of the sample after fabrication. In the literature, this is often done by a surface probe technique, such as STM [105, 106, 127], AFM [128] or low-energy electron diffraction (LEED) [126, 195], or inferred from transport data [9, 101, 102]. Here, we determine the twist angle directly from the ARPES data.

From geometry, the distance between the $\mathbf{K_1}$ and $\mathbf{K_2}$ points can be related to the twist angle through the following equation:

$$|\mathbf{K_2} - \mathbf{K_1}| = \frac{8\pi}{3a} \sin\left(\frac{\theta}{2}\right). \qquad (3.4.1)$$

Additionally, the mBZ can be drawn from the $\mathbf{K_1}$ and $\mathbf{K_2}$ points, and has replicas centred on the mBZ corners. By taking a constant energy cut at E_F, the replica periodicity becomes more obvious and can be used to position the mBZ, which in turn provides the positions for $\mathbf{K_1}$ and $\mathbf{K_2}$. From Eq. (3.4.1), this can then be used to calculate a twist angle.

This method is demonstrated in Fig. 3.11. Figs. 3.11 (a)–(d) are constant energy cuts at E_F for the same tBG data set as in Figs. 3.7(a) and 3.9(c). Note that the data orientation is as measuring from the experiment and has not been rotated to align $\mathbf{K_1} \rightarrow \mathbf{K_2}$ parallel to the k_y axis. Weak replica spots can be seen surrounding the $\mathbf{K_1}$ and $\mathbf{K_2}$ points, forming a hexagonal pattern (Fig. 3.11(a)). The appearance of this can be enhanced by using a logarithmic scale (Fig. 3.11(b)). The size and position of the mBZ is adjusted to best match the corners with the replica and primary spots (Figs. 3.11(c) and (d)). The $\mathbf{K_1}$ and $\mathbf{K_2}$ coordinates can then be read off from this (black and blue dashed lines). Because each spot has a finite width, there is some amount of variation in the acceptable positioning of the mBZs, which provides an estimate of the uncertainty for the twist angle. For this particular data set, we determine a twist angle of $3.4 \pm 0.1°$.

To gauge the accuracy of this method, we have also performed LEED from the same sample after the ARPES measurements. LEED patterns were acquired
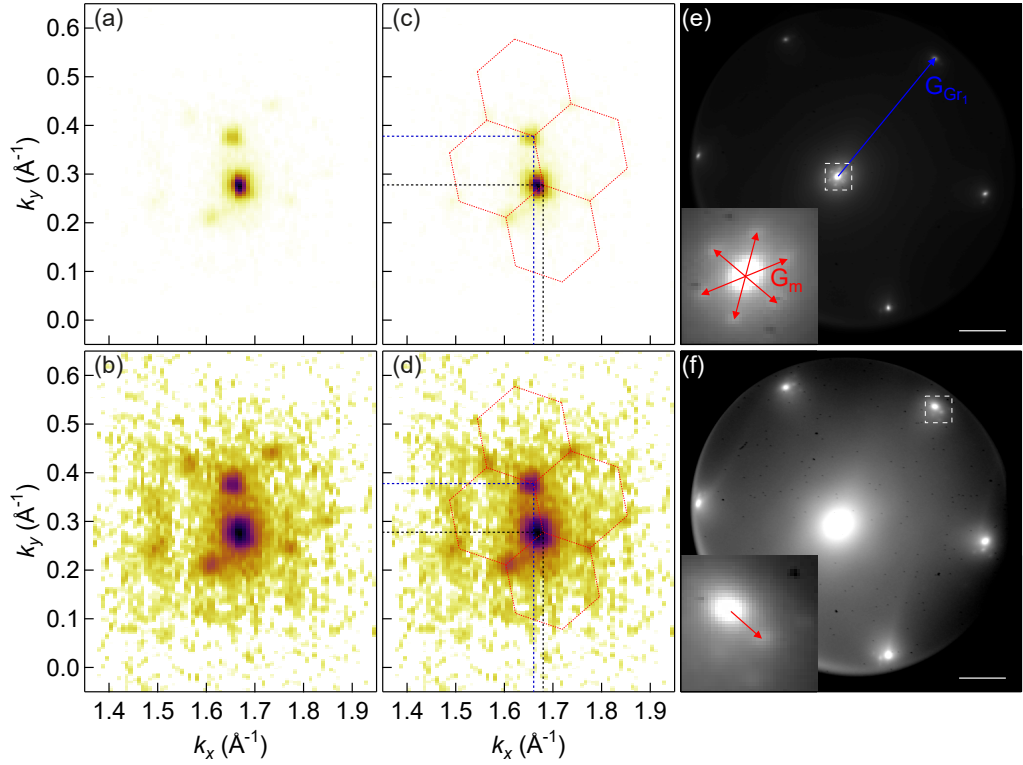
Figure 3.11: a,b) 3.4° tBG ARPES constant energy cut at $E - E_F = 0$ displayed on a (a) linear and (b) logarithmic scale, averaged over ±15 meV of the specified energy. c,d) The same constant energy cut as in (a) and (b) but overlaid with four mBZs and dashed lines to mark the coordinates of the $\mathbf{K_1}$ and $\mathbf{K_2}$ positions. e,f) LEED pattern taken from the same tBG sample displayed on a (e) linear and (f) logarithmic scale. Insets are from the white dashed boxes. $\mathbf{G_{Gr_1}}$ and $\mathbf{G_m}$ are the top layer graphene and moiré reciprocal lattice vectors, respectively. The colour scale of (f) has been saturated to emphasise the weak replica spots. Scale bars are 1 Å^{-1}.

by Brice Sarpi and Francesco Maccherozzi at the I06 beamline of Diamond Light Source. From the LEED pattern in Fig. 3.11(e), first order diffraction spots from the top layer graphene can be seen close to the edge of the Ewald sphere, as well as six replica spots around the zeroth order spot, originating from the moiré periodicity. By adjusting the contrast, it is also possible to see the weaker first order spots from the bottom graphene layer, surrounded by additional replica spots (Fig. 3.11(f)). From the insets, the moiré reciprocal lattice vector, $\mathbf{G_m}$, can be seen to be the same as the vector between the first order diffraction spots for the two graphene layers and, hence, can be used to calculate the twist angle. The reciprocal space scale was calibrated from the graphene first order spots, which have a reciprocal lattice vector
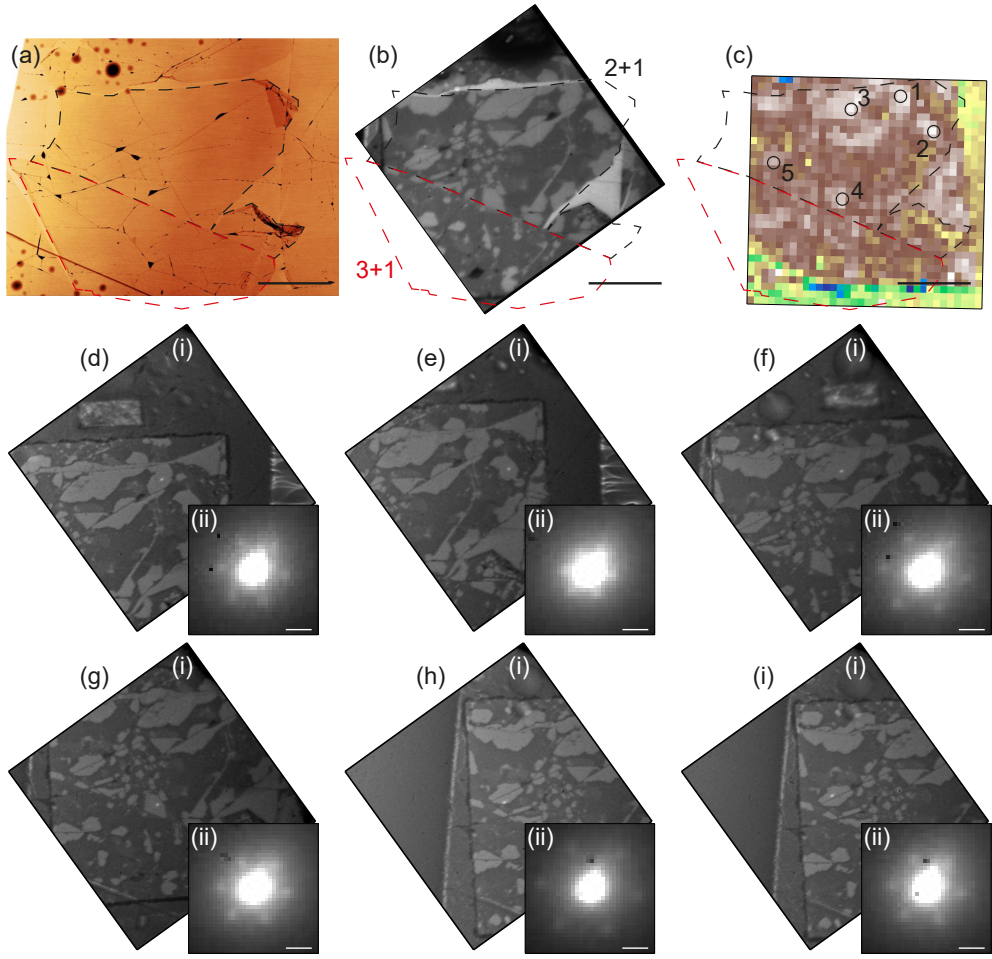
Figure 3.12: a) AFM topography image of a twisted graphene sample, marked with dashed lines for the 2+1 (black) and 3+1 (red) regions. b,c) LEEM and SPEM images, respectively, of the same area in (a). Positions in (c) mark the locations that ARPES spectra were measured from. Scale bars are 10 µm. d–i) (i) LEEM images and (ii) LEED patterns taken from the same twisted graphene sample in similar locations to the ARPES spectra. (i) is overlaid with the illumination aperture (central white spot) used when measuring the LEED patterns in (ii), marking the precise position the data was recorded from. LEED patterns in (ii) show the moiré surrounding the zeroth order spot. Scale bars are 0.1 Å^{-1}.

of $|\mathbf{G_{Gr}}| = 2.95$ Å^{-1} (Section 1.2.1). The six central replica spots surrounding the zeroth order spot provided an average value and error bar for $|\mathbf{G_m}|$, which was then used to calculate a twist angle from Eqs. (1.3.1) and (1.3.2). In this way, the twist angle was found to be $3.2 \pm 0.1°$. Though not exactly the same, this value agrees within uncertainty to that determined from ARPES.

As will be shown next, there can be relatively large differences in twist angle

Sample position	Twist angle from ARPES	Twist angle from LEED
1	$2.4 \pm 0.1°$	$2.3 \pm 0.1°$ (d)
2	$2.7 \pm 0.2°$	$1.7 \pm 0.2°$ (e)
3	$2.9 \pm 0.2°$	$2.9 \pm 0.1°$ (f)
4	$3.1 \pm 0.2°$	$2.4 \pm 0.1°$ (g)
5	$3.4 \pm 0.1°$	$3.3 \pm 0.1°$ (h)
		$2.5 \pm 0.1°$ (i)

Table 3.2: Twist angles measured from different regions of a 2+1 twisted graphene sample, determined using ARPES constant energy cuts and LEED patterns. Sample positions refer to those marked in Fig. 3.12(c).

for sample regions only a few microns apart. Additionally, the twist angle can change when the sample is heated, particularly evident in very small twist angle samples that have a tendency to realign at increased temperatures [172]. LEED measurements were taken at 300°C to prevent deposition of hydrocarbons onto the surface, which could have affected the twist angle. There is also distortion present in the LEED patterns due to misalignment within the low-energy electron microscopy (LEEM) system. This affects both the measured value of $|\mathbf{G_m}|$ and the calibration. Considering all of these factors, small differences between the twist angles calculated from the ARPES spectra and those from the LEED patterns are thus to be expected.

To further explore the validity of our twist angle measurements, we performed LEED measurements on a 2+1 sample that showed a number of different twist angles from ARPES. Figs. 3.12(a)–(c) show AFM, LEEM and SPEM images of the sample, respectively. Fig. 3.12(c) is marked with the five positions that ARPES spectra were acquired from, measured using the zone plate for increased spatial resolution. The marked positions coincide with bright regions in the SPEM image, corresponding to areas of increased intensity and uniformity. Interestingly, the shape of these bright regions matches with those in the LEEM image in Fig. 3.12(b), suggesting these areas are intrinsically more clean, and allowed an easier comparison of the two images.

Figs. 3.12(d)–(i) show LEED patterns taken from similar positions to the ARPES data. The calculated twist angle for each LEED pattern is shown in Table 3.2, compared with those extracted from the ARPES spectra. For positions 1, 3 and 5 (when compared with Fig. 3.12(h)) the agreement is very good, with the estimated twist angles being within uncertainty. For positions 2 and 4, however, the twist angles from ARPES and LEED are strikingly different. A twist angle difference of this size seems unlikely to have come from any systematic error imposed by the calculation method, neither do we suspect the twist angle to have changed
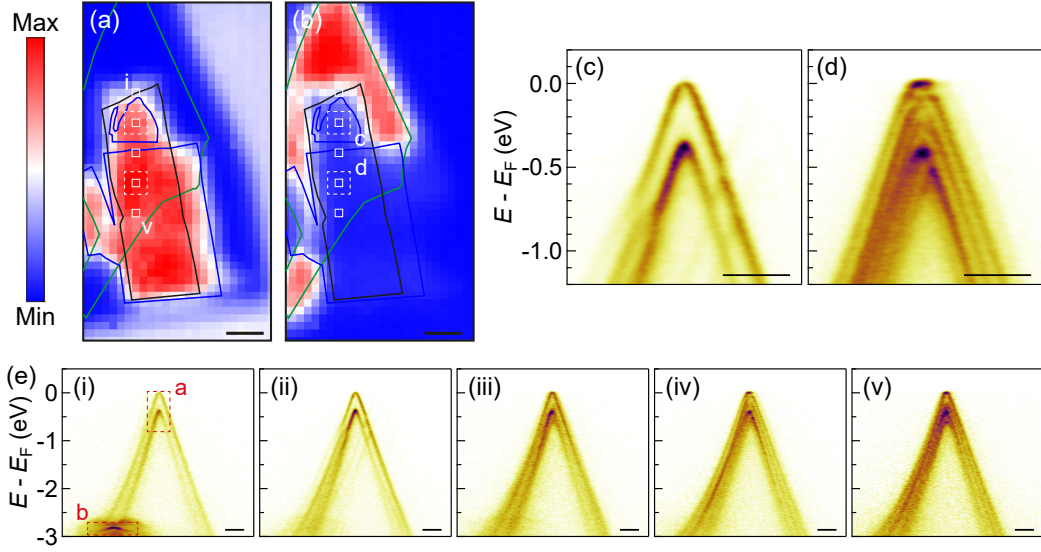
Figure 3.13: a,b) SPEM images of a tDBG sample, obtained by integrated over the red dashed boxes in panel (i). Real-space scale bars are 10 μm. c,d) Total ARPES spectra acquired by summing over the individual ARPES spectra from the white dashed boxes in (a) and (b). e) ARPES spectra from the SPEM image positions marked by the white boxes in (a) and (b). Reciprocal-space scale bars are 0.2 Å^{-1}.

by this amount between measurements. The more likely scenario is that the two measurements were taken from slightly different positions that have a large twist angle difference between them. In support of this, LEED patterns from Figs. 3.12(h) and (i) were both taken from approximately position 5, but have a large difference in twist angle. From the LEEM image, we can identify a dark line that separates positions (h) and (i), which is assumed to be a wrinkle in the graphene layers. This can give rise to the large different in twist angle observed, despite the two positions being only microns away from each other [196]. Considering this, and the agreement for positions 1, 3 and 5, we believe our method of determining the twist angle from the ARPES spectra is valid and gives us confidence in the twist angles we quote moving forward.

The sample presented in Fig. 3.12 shows a large amount of surface disorder and different twist angles which are only uniform over the scale of a couple micrometers. The 4–5 μm spot size provided by the capillary mirror is clearly too large to reliably measure ARPES from these regions without contribution from neighbouring domains. This brings into question how confident we can be that the ARPES spectra measured using the capillary mirror is from a uniform area? SPEM mapping provides some level of knowledge on the sample uniformity and helps to locate the best

positions for high quality ARPES spectra. Figs. 3.13(a) and (b) are SPEM images for the same tDBG sample shown in Fig. 3.6. The white dashed boxes are centred on two positions where ARPES spectra for tDBG was acquired from, corresponding to the 7.5° and 1.5° data shown in Fig. 3.8, respectively. Figs. 3.13(c) and (d) are summations of the $I(E,k)$ spectrum from the positions within the white dashed boxes. The fact that sharp bands and clear hybridisation gaps are maintained shows these regions to be uniform over at least a 6 μm range (size of white dashed box). The series of $I(E,k)$ spectra shown in Fig. 3.13(e) are taken from different positions on the SPEM image. When in a disordered area (panels (iii) and (v)), the spectrum appears broad and features contributions from different twist angle domains that are superimposed on top of each other without clear interactions. By analysing the sharpness of the spectra from different positions on the SPEM image, uniform twisted regions can be identified that are suitable for measuring ARPES from. This allowed us to acquire the high quality ARPES spectra presented in this Chapter and the next, confident that it was from a single twist angle domain.

3.5   Summary

In this Chapter, we have outlined the key features in the ARPES spectra of few-layer aligned and twisted graphene. Fitting of monolayer and bilayer Dirac cones to low-energy approximations allows an estimation of their respective Dirac energies, band velocities and carrier densities. Extracted band positions also highlight deviations from the expected bare-band dispersion due to many-body interactions. These were shown to be negligible in our aligned graphene samples, and are only expected to become important at high doping concentrations. The ARPES intensity distribution around the **K** point for bilayer (and thicker) graphene shows a dependence on photon energy. Through simulation of the photoemission process, this was shown to come from interference between photoelectrons emitted from different layers, where the phase difference depends on the photon energy.

We have studied three twisted graphene systems: tBG, tMBG and tDBG. At large twist angles, their low energy dispersions can be expressed as the non-interacting individual graphene layers. At higher binding energies, they exhibit interlayer interaction effects in the form of hybridisation gaps and replica bands. As the twist angle is reduced, these interlayer features become more pronounced and move closer to E_{F}. The bandwidth of the top valence band also shrinks, eventually becoming a flat band at the magic-angle. The electronic structure close to the **K** points can be modelled by a HkpTB model that couples graphene layers either side

of the twisted interface through off-diagonal terms in the Hamiltonian. Combined with simulation of the photoemission intensity, these calculations show qualitative agreement with the experimental ARPES data.

The twist angle can be determined from constant energy cuts at E_F. Replica bands are centred on the mBZ corners, forming a honeycomb pattern. The mBZ can be positioned from this periodicity, whose size provides the twist angle. This method was compared to twist angles determined from LEED, which gave good agreement in most cases. These results also highlighted the many different twist angle domains possible across a sample and their variation in size. We could confirm a particular region was uniform through a simple qualitative analysis of the measured spectra: uniform areas give sharp ARPES features and clear hybridisation gaps; disordered regions give broad bands where spectra from different twist domains are superimposed with no clear interactions.

These results provide a foundation with which we can explore specific quantitative features within the ARPES data of twisted graphene, allowing us to compare these directly to predictions from theory.

Chapter 4

Twist- and gate-dependent spectroscopic features in few-layer twisted graphene

4.1 Introduction

The majority of previous ARPES studies on twisted graphene have involved relatively large twist angles of $\theta > 3°$ [124–126, 134, 195–197], due to difficulties with fabricating small twist angle samples with uniform regions [172]. µARPES measurements of near-magic-angle tBG have been reported, able to detect a flat-like band at E_{F}, however, they lacked the resolution to resolve its dispersion [127, 128]. Nonetheless, ARPES offers a unique momentum-resolved route to studying interlayer interactions in moiré systems, able to quantify coupling parameters and band renormalisation effects, and can help test theoretical predictions [194].

In the previous Chapter, we introduced ARPES spectra for tBG, tMBG and tDBG at selected twist angles. Through low contamination fabrication methods and careful experimental preparation, we have been able to achieve high quality twisted samples offering improved energy resolution compared to many reports in the literature, better highlighting the hybridisation and moiré features visible in the ARPES spectra. Across 9 different samples, 6 tBG, 8 tMBG and 3 tDBG twist angles could be accessed by µARPES. Together, this allows a systematic study of the electronic structure of twisted graphene across a range of twist angles and stacking arrangements, which can help refine theoretical models.

In this Chapter, we use the intensity of moiré replicas and the size of hybridisation gaps as quantifiable parameters in the ARPES spectra of twisted graphene.

These were measured across all available twist angles and stacking systems and are compared with predicted values from the HkpTB model. This allows further validation of the theory and demonstrates a method of estimating the magnitude of interlayer coupling parameters. In addition to this, we looked specifically at the ARPES spectrum of 1.5° tDBG which exhibited a highly non-dispersive band at E_{F}. Characterising this flat band highlights limitations to the HkpTB model and the potential importance of lattice relaxations in calculations of small twist angles systems.

Many studies implement twisted graphene into simple device geometries that allow tuning of the carrier concentrations to access different correlated phases [9, 10, 101, 102]. Understanding the effects of electrostatic doping on the band structure of twisted graphene is thus critical for explaining these phases, as well as for the design of future twisted devices [198]. We end this Chapter by investigating the gate-dependent electronic structure of 3.4° 1+2 twisted graphene. Key parameters are extracted by fitting to the ARPES data and compared to theoretical predictions, calculated using a self-consistent method.

4.2   Twist-dependent replica intensities

A key feature in the ARPES spectra of moiré systems is the appearance of replicas surrounding the primary bands [120–123]. In the case of twisted graphene, these are replicas of the graphene $\mathbf{K}$ bands [126, 194]. As discussed in Chapter 3, the replicas are positioned at the mBZ corners, forming a honeycomb lattice of graphene-like bands. The geometry of this lattice resembles that of the individual graphene layers (Fig. 1.1(b)), but on a much smaller reciprocal space scale. In a similar way to the main BZs, the mBZ has 'valleys' corresponding to replicas of the $\mathbf{K_1}$ and $\mathbf{K_2}$ primary bands (Fig. 1.8(c)), where the vector between equivalent replicas is equal to the moiré reciprocal lattice vector, $\mathbf{G_m}$. This is evidenced in tMBG where the bands at the mBZ corners alternate between monolayer and bilayer cones (Fig. 4.1). The intensity of the replicas decreases moving away from the primary bands, indicative of scattering processes that transfer spectral weight from one state to another. It is tempting to assume this spectral weight comes solely from the neighbouring primary band scattered by the moiré reciprocal lattice vector, however, a simple analysis of ARPES constant energy cuts shows this not to be the case.

Fig. 4.1 shows a simulated constant energy cut of 3.2° 1+2 twisted graphene centred around different valleys of the main BZs. The data has been additionally plotted on a logarithmic scale to better emphasise the appearance of the replicas.
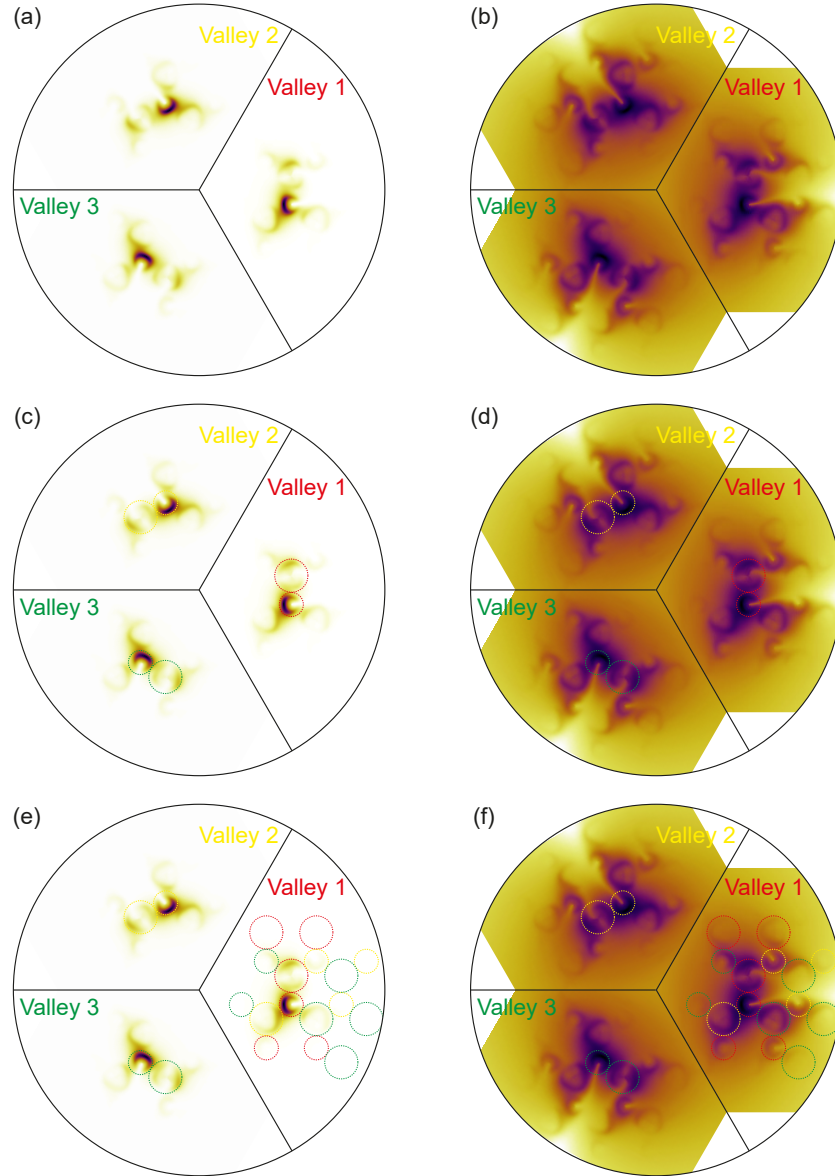
Figure 4.1: a,b) Simulated constant energy cuts of 3.2° 1+2 twisted graphene for $E - E_\mathrm{F} = -100$ meV at three equivalent valleys of the primary BZs. Intensity is plotted on a (a) linear and a (b) logarithmic scale. c,d) Simulated constant energy cuts of (a) and (b), respectively, overlaid with red, yellow and green circles to mark monolayer and bilayer primary cones within different valleys. e,f) Simulated constant energy cuts of (a) and (b), respectively, further overlaid with red, yellow and green circles surrounding replica cones within valley 1. Colours are assigned to different replica cones so as to match them with primary bands in different valleys that exhibit the same dark corridor orientation.
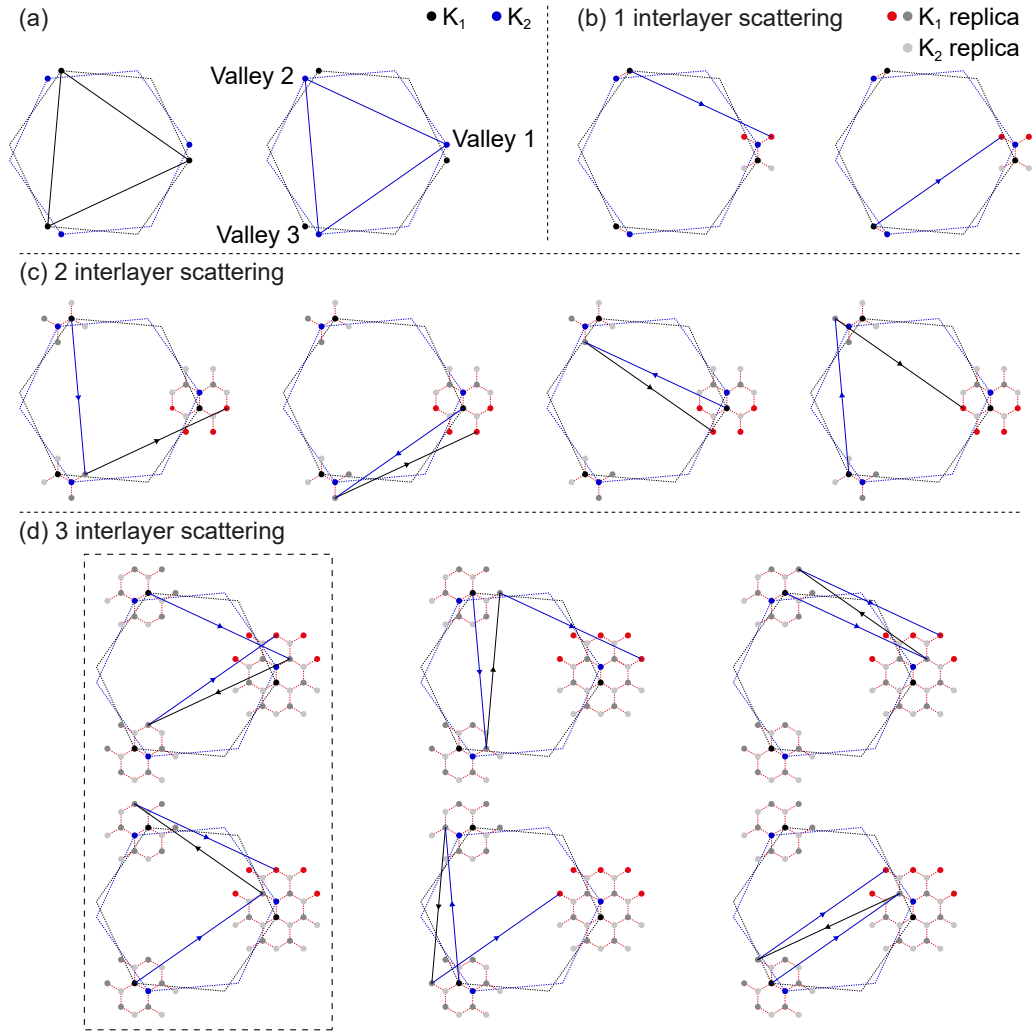
Figure 4.2: a) Schematic Brillouin zones for the top and bottom layers of twisted graphene. Solid lines show intervalley scattering vectors. b–d) Schematics of the interlayer scattering processes that give rise to the replicas observed in twisted graphene and the resulting mBZs.

When scattered by a reciprocal lattice vector, the graphene bands are known to conserve the orientation of their dark corridor [192]. The orientation of the replica cones thus reveals which primary band they originated from. This is demonstrated in Fig. 4.1, where the replicas surrounding the valley 1 **K** points have been matched with primary bands in valley 1 (red), valley 2 (yellow) and valley 3 (green) according to their dark corridor orientation. It is clear that many replicas originate from primary bands in different valleys.

By knowing which valley each replica must originate from, it is possible to

construct scattering pathways using the reciprocal lattice vectors of the individual graphene layers. The BZs for the two graphene layers are shown schematically in Fig. 4.2(a), where solid lines show the reciprocal vectors that connect equivalent $\mathbf{K}$ valleys of each BZ. In Figs. 4.2(b)–(d), these vectors have been used to construct scattering pathways to the different replicas of the $\mathbf{K_1}$ points. Starting with Fig. 4.2(b), the reciprocal vectors from the bottom layer scatter states from the $\mathbf{K_1}$ points in valley 2 (right) and valley 3 (left) to $\mathbf{K_1}$ replica positions in valley 1, in agreement with the valley assignment in Fig. 4.1. For future reference, these replicas will be described as primary replicas, requiring only a single scattering vector to reach from a primary $\mathbf{K}$ point. Similarly, one can imagine scattering vectors from the $\mathbf{K_1}$ point of valley 1 to $\mathbf{K_1}$ primary replicas in valleys 2 and 3, in addition to scattering vectors between valleys 2 and 3. In fact, these processes can be seen in Fig. 4.2(c), where there is now an additional scattering vector from these primary replicas to secondary replicas (2 scattering processes) around valley 1. Again, the $\mathbf{K_1}$ point of origin for each replica scattering pathway agrees with the dark corridor assignment in Fig. 4.1. Importantly, these scattering pathways consist of an initial scattering by a bottom layer vector followed by subsequent scattering by a top layer vector. This alternation between scattering vectors continues in Fig. 4.2(d), resulting in tertiary replicas that have come from secondary replicas scattered by a bottom layer vector. At this point the replicas become very faint, due to the finite scattering probability, and it is difficult to truly validate which $\mathbf{K}$ valley they originate from. Note the two scattering pathways in the dashed box that end at the same replica position. If the intensity of this replica was greater in Fig. 4.1, one would expect to observe a superposition of the dark corridor intensity distribution from valleys 2 and 3.

Though not explicitly shown here, similar scattering pathways exist for the $\mathbf{K_2}$ replicas; beginning from a $\mathbf{K_2}$ point and initially scattered by a top layer reciprocal vector. The scattering pathways described in Fig. 4.2 demonstrate the lowest order (shortest) pathways for each replica. Higher order scattering pathways can also be constructed, for example, by including scattering between replicas of the same rank (i.e. primary to primary, secondary to secondary, etc.). These contribute less to the observed intensity due to the greater number of scattering processes. The alternation between reciprocal vectors within the scattering pathways reflects the interlayer nature of the electron hopping processes in moiré systems. Bistritzer and MacDonald describe these as tunnelling processes, where the electrons in one layer are influenced by and tunnel into a neighbouring layer [100]. The processes in Fig. 4.2(b) demonstrate electrons originating in the top layer being scattering
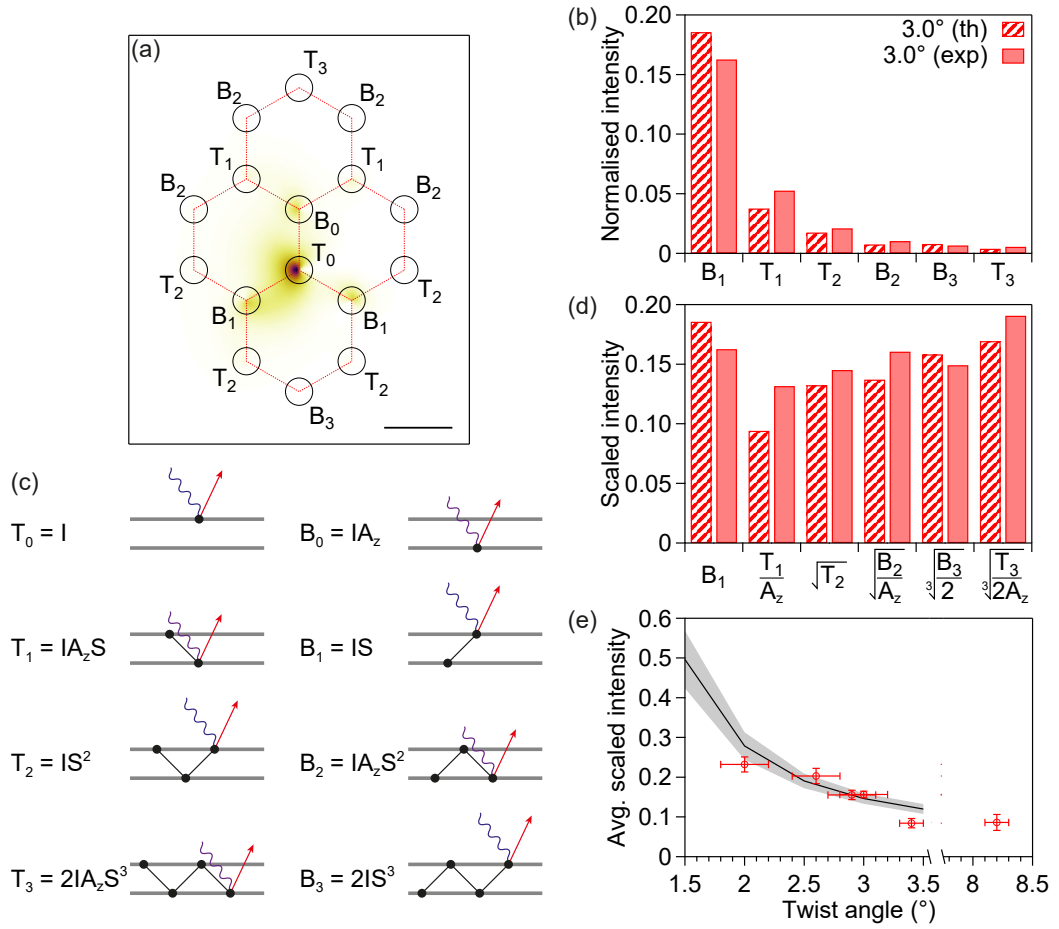
Figure 4.3: a) Simulated constant energy cut of 3.0° tBG at E_F overlaid with the mBZs in red. mBZ corners are labelled according to their scattering pathways. Scale bar is 0.1 Å^{-1}. b) Replica intensity of 3.0° tBG from simulation and experiment, taken from the circular regions in (a) and normalised by the intensity of T_0. c) Model of the scattering and photoemission processes that give rise to the different replica intensities. $A_z = 0.4$ is the attenuation factor and S is proportional to the scattering probability. d) Replica intensity of 3.0° tBG scaled according to the model in (c). e) Average scaled replica intensity of tBG as a function of twist angle. Data points are from experiment. The black line is the averaged value from simulations and the grey shading is the uncertainty.

by the bottom layer and tunnelling into it. Fig. 4.2(c) then shows these electrons tunnelling back into the top layer, and so on.

Replica intensities from experimental and simulated ARPES spectra were compared to help understand the influence of these interlayer scattering processes. Fig. 4.3(a) shows a simulated constant energy cut at E_F for 3.0° tBG. The primary and replica points have been labelled according to the scattering pathways outlined

in Fig. 4.2. T and B refer to top and bottom layer points, respectively, while the numbered index refers to the number of reciprocal vectors in the lowest order scattering pathway for each point. For example, the intensity at the primary Dirac points, $\mathbf{K_1}$ and $\mathbf{K_2}$, is thus given by T_0 and B_0, respectively. Similarly, T_1, T_2 and T_3 refer to the primary, secondary and tertiary replicas from the top layer, and the same for the bottom layer but with T replaced by B. The intensity of the replicas is plotted in Fig. 4.3(b), where the total intensity is taken from the circular regions marked in Fig. 4.3(a) and averaged over equivalent replica points, as well as being normalised by T_0. There is relatively good agreement between the plotted experimental and simulated intensities, suggesting the model introduced in Chapter 3 for describing the photoemission process is reliable. As expected, the intensity generally decreases for replicas with longer scattering pathways. It is noticeable, however, that B_1 is much greater than T_1. Similarly, T_2 is greater than B_2, despite the scattering distances being the same.

To explain the observed trends in intensity, we refer back to the interlayer nature of the scattering pathways. As described in our photoemission model, electrons emitted from the lower layers become attenuated by the layers above, reducing the photoemission intensity. Similarly, an electron that originated in the top layer but has tunnelled to the bottom will also be attenuated. From this, we have developed a simple model to describe the intensity of different replicas, shown schematically in Fig. 4.3(c). Electrons beginning at $\mathbf{K_1}$ and $\mathbf{K_2}$ points tunnel between layers as they scatter to replica sites, with a scattering probability proportional to S. These electrons are then photoemitted, where those being emitted from the lower layer are attenuated by a factor A_z. Assuming $A_z = 0.4$, as used in the previous Chapter, the only unknown is S. In Fig. 4.3(d), the replica intensities have been scaled so as to set them equal to S. Note, the additional factor of 2 for B_3 and T_3 is because the tertiary replicas considered in Fig. 4.3(a) have two equivalent scattering pathways (dashed box in Fig. 4.2(d)). The scaled intensities are roughly constant, indicating the simple model is a reasonable approximation to the data. The small differences seen can be expected to come from higher order scattering pathways that would renormalise these values.

Averaging these scaled intensities gives an estimate for S. This was repeated for tBG spectra from a range of twist angles and plotted in Fig. 4.3(e). Data points are calculated from experimental spectra at the determined twist angles. The black line is from discrete simulated spectra of twist angle $1.5° \leq \theta \leq 3.5°$ at $0.5°$ intervals. The average scaled intensity remains roughly constant at large twist angles, but increases significantly for $\theta < 3°$, indicative of an increase in the
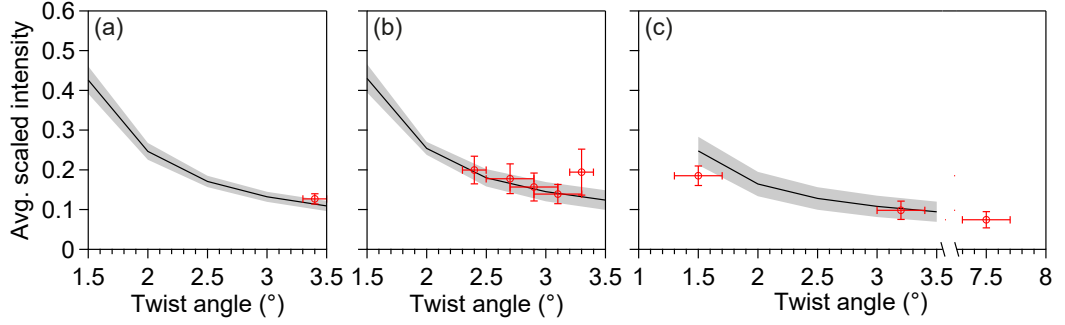
Figure 4.4: a–c) Average scaled replica intensities as a function of twist angle for (a) 1+2, (b) 2+1 and (c) 2+2 twisted graphene. Data points are from experiment. The black lines are averaged values from simulations and the grey shading is the uncertainty.

scattering probability. This likely comes from the decrease in the size of the mBZ and the distance of the replicas from their neighbouring primary **K** points, as scattering processes are more likely when scattering to states close to the **K** points [100].

Average scaled replica intensities were similarly calculated for 1+2, 2+1 and 2+2 twisted graphene as a function of twist angle, plotted in Fig. 4.4. In the case of 1+2 and 2+1 systems, both monolayer and bilayer replicas are present, which, due to their different dispersions, give different intensities at E_{F}. To allow a fair comparison between replicas, an additional scaling factor, η, was included in the analysis to adjust for this difference in intensity. For 1+2, this scales the bilayer intensities to be more 'monolayer-like', and vice versa for 2+1. η was calculated from the simulated constant energy cuts for 1+1 and 1+2 twisted graphene using the equation $\frac{\mathrm{B}_0^{1+1}}{\mathrm{T}_0^{1+1}} = \eta \frac{\mathrm{B}_0^{1+2}}{\mathrm{T}_0^{1+2}}$. Here, B_0^{1+1} is intensity from a bottom monolayer, B_0^{1+2} is intensity from a bottom bilayer, and η is their ratio. T_0^{1+1} and T_0^{1+2}, both intensity from a top monolayer, are included to account for any differences in total intensity. It was found η varies subtly with twist angle, so a new value was calculated for each simulated twist angle. For the experimental twist angles, η was calculated from an interpolation of the simulated values. η thus scales the bilayer intensities in the 1+2 data by the modification $\mathrm{B}^{1+2} \to \eta \mathrm{B}^{1+2}$, and similarly scales the monolayer intensities in 2+1 by $\mathrm{T}^{2+1} \to \frac{\mathrm{T}^{2+1}}{\eta}$. In addition to these changes in calculating the scaled replica intensities, the attenuation factor for 2+1 and 2+2 was changed from A_z to A_z^2 to account for the top layer being bilayer graphene.

The resulting average scaled replica intensities are shown in Fig. 4.4. Across all stacking arrangements, there is good agreement between experimental and simulated data. The observed trends are similar to that for tBG in Fig. 4.3(e), increasing

below 3°, but at a slower rate for systems with a greater number of layers. The minimum value at large twist angles is roughly the same between all cases, however, suggesting a regime that is independent of twist angle and number of layers. The 1+2 and 2+1 curves are also approximately the same across the investigated angular range. Though expected, as the scattering probability should be independent of stacking order, this consistency is highly encouraging and gives confidence in the chosen method.

The results presented here demonstrate a quantitative method of analysing replica intensities which can be directly compared to simulated ARPES spectra. We see good agreement between the experimental and simulated results, further validating the HkpTB model. This type of analysis would be highly applicable to other moiré systems that exhibit replicas in their ARPES spectra, which may provide further insight into the present interlayer coupling. Alternatively, this coupling can also be investigated through the magnitude of hybridisation gaps, which will be discussed in the next section.

4.3 Twist-dependent hybridisation gaps

As mentioned in Section 3.3, hybridisation gaps appear in the ARPES spectra of twisted graphene where the primary bands intersect. Anti-crossing effects such as this are common in layered structures of 2D materials, and are usually a result of the coupling between out-of-plane electron orbitals [118, 119, 199, 200]. Consequently, the size of the hybridisation gaps are dependent on the strength of this coupling. In the case of twisted graphene, the coupling is defined by the previously discussed SWM parameters. Measuring the size of the hybridisation gaps in twisted graphene thus provides a method to test the accuracy of these parameters.

We have measured hybridisation gaps across a range of twist angles for ARPES spectra acquired from tBG, tMBG and tDBG samples. Figs. 4.5(a)–(c) show example spectra for each of these systems that display clear hybridisation gaps between the primary bands. As stated previously (Section 3.3) the number of hybridisation gaps present increases with the number of layers. For tBG and tMBG, we have considered all hybridisation gaps (1 and 2 respectively) whereas for tDBG, we have only measured the lowest binding energy gap, as it was the most pronounced and could still be easily identified at small twist angles. To estimate the size of the hybridisation gaps, energy distribution curves (EDCs) were extracted from the ARPES spectra at the centre of the anti-crossings, as shown in Figs. 4.5(d)–(g). The peaks originating from the anti-crossing bands were fit to a
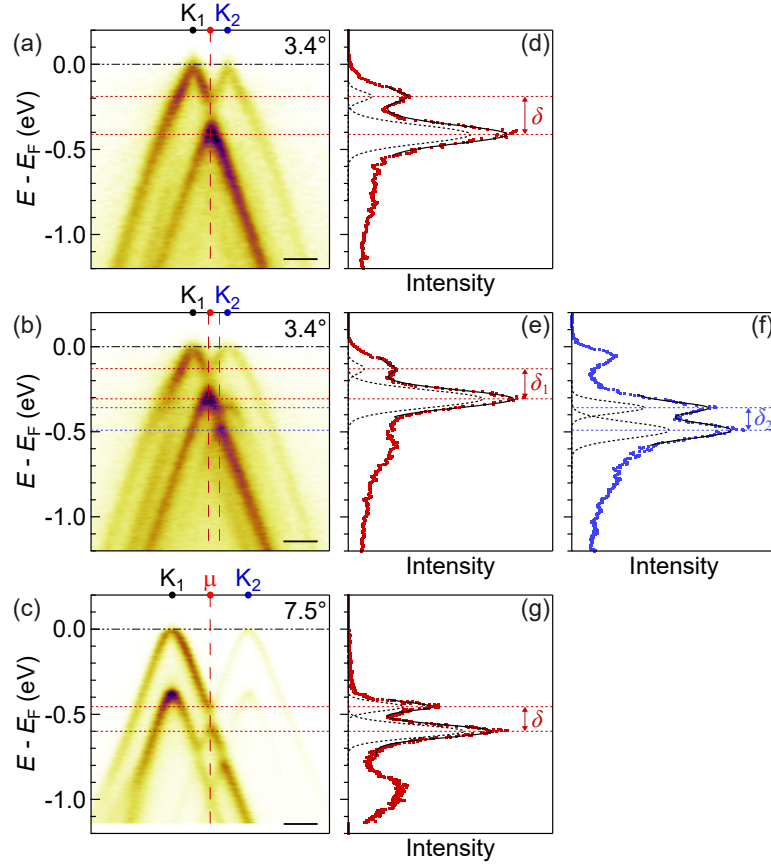
Figure 4.5: a–c) Energy-momentum cuts taken along the $\mathbf{K_1} \rightarrow \mathbf{K_2}$ direction of (a) tBG, (b) tMBG and (c) tDBG, respectively, at the specified twist angles. Scale bars are 0.1 Å^{-1}. d–g) EDCs extracted along the vertical dashed lines in (a)–(c). Solid black lines are fits to the data using a linear combination of two Gaussian functions. Dashed black lines show individual Gaussian peaks, whose separation (red and blue dashed lines) gives the hybridisation gap size, δ.

pair of Gaussian peaks, where the difference between the Gaussian peak positions provided the hybridisation gap size, δ.

The measured hybridisation gap sizes as a function of twist angle are plotted in Fig. 4.6 for the three twisted graphene systems . This is compared to the calculated gap sizes from the HkpTB model using the SWM parameters outlined in Table 3.1. Note, the same SWM parameters have been used for each twisted graphene system, without fitting to the experimental data. The observed agreement highlights the accuracy of the HkpTB model used, as well as reinforcing our choice of SWM parameter values. A more complete study of the size of the hybridisation gaps as a function of twist angle could be used to help refine the values for the
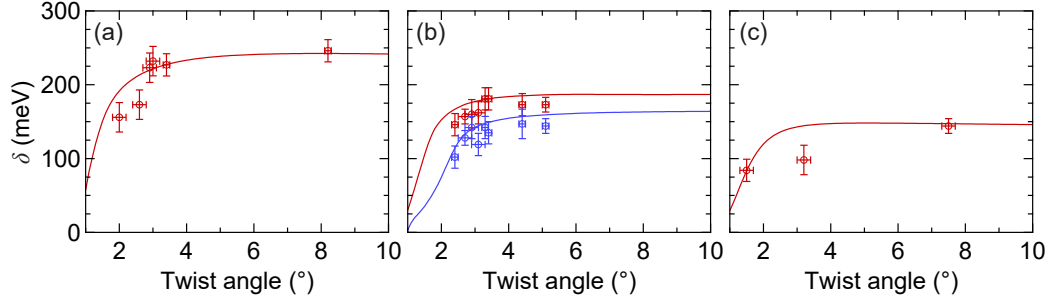
Figure 4.6: a–c) Plots of hybridisation gap size as a function of twist angle for (a) tBG, (b) tMBG and (c) tDBG, respectively. The solid lines correspond to gap sizes extracted from calculated band structures using the HkpTB model, and data points to those extracted from experimental ARPES spectra.

different coupling parameters, as there is still some variation in the literature [193].

For the three twisted graphene systems considered in Fig. 4.6, δ shows qualitatively similar behaviour as a function of twist angle, with only a reduction in magnitude for increased number of layers. For twist angles above $3°$, δ remains roughly constant. In this large angle regime, the anti-crossings occur at high binding energies and the system can be thought of as two weakly interacting graphene sheets, where the size of the hybridisation gaps comes solely from the magnitude of the SWM parameters. Below $3°$, δ shrinks with decreasing twist angle. In this regime, the hybridisation gaps are approaching both E_F and the Dirac points. The strong modification from the usual graphene dispersion and the close proximity to other bands may act to shrink the hybridisation gaps, resulting in the observed trend.

Measuring the size of the hybridisation gaps becomes increasingly difficult as the twist angle and mBZ size is reduced, increasing the number of bands and requiring ever improving energy and momentum resolution. At very small twist angles, the idea of a hybridisation gap is almost meaningless, with the low-energy electronic structure having little to no resemblance of the original graphene dispersion. Instead, the key feature in the twisted graphene band structure becomes the flat band at E_F. So far, gaps have been measured at or near the μ point, however, as will be shown in the next section, the more meaningful gap between the flat band and the next valence band states is at γ.
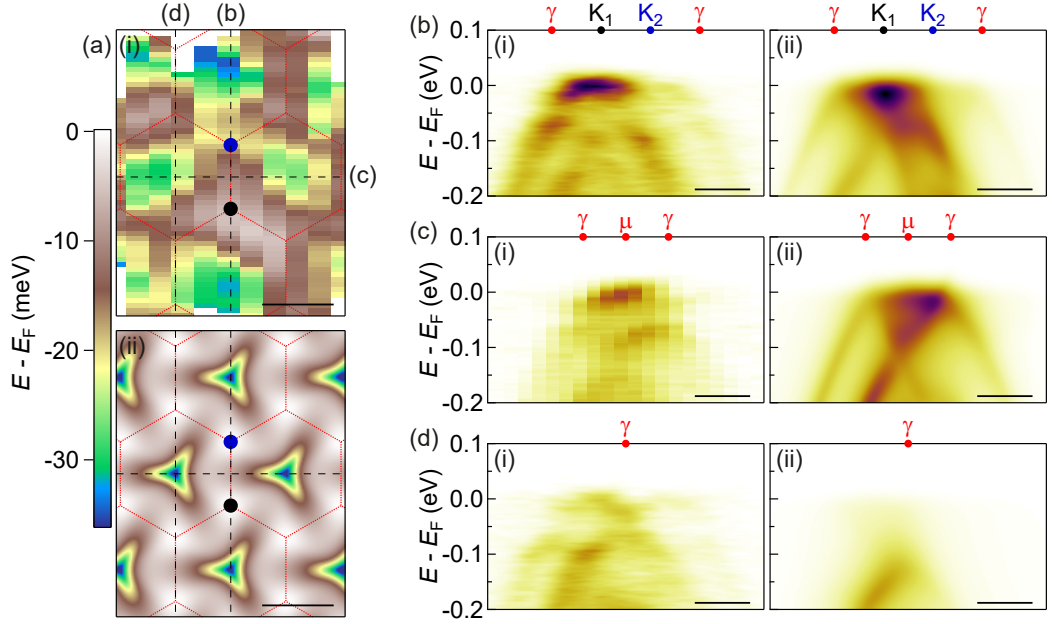
Figure 4.7: a) Energy of the flat band for 1.5° tDBG extracted from the (i) experimental ARPES data and (ii) calculated band structure using the HkpTB model, plotted in the $k_x - k_y$ plane, with the mBZs overlaid in red. b–d) (i) Experimental and (ii) simulated energy-momentum cuts taken along the black dashed lines in (a). The simulated broadening has been reduced to 40 meV to match the improved quality of the experimental spectra from this particular sample. Scale bars are 0.05 Å^{-1}.

4.4 Analysis of the tDBG flat band

The smallest twist angle measured here using μARPES was $1.5 \pm 0.2°$ from a tDBG sample, as seen in Fig. 3.8(c). Here, an intense, approximately-flat band is observed at E_F. At this twist angle, the mBZ has become so small that the usual replica features cannot be resolved in constant energy cuts at E_F. Instead, the mBZ is positioned using the flat band topology, shown in Fig. 4.7(a) panel (i). The dispersion of the flat band was determined by taking EDCs over an area in the $k_x - k_y$ plane and fitting the lowest energy peak to a Gaussian distribution. Though on the limit of the experimental resolution, a weak dispersion can be determined. Assuming the measured minima to be approximately at the γ point, as expected from theory (Fig. 4.7(a) panel (ii)), the mBZ was positioned as shown. This returns the aforementioned value for the twist angle, with the error bar coming from uncertainty in the position and size of the mBZ.

Figs. 4.7(b)–(d) show energy momentum cuts taken along different high symmetry directions of the mBZ. Panels (i) show the experimental spectra. In all cases,

a weakly dispersing band near E_F is visible, belonging to the flat band, which is clearly gapped from the next valence band states. However, in the case of the simulated spectra in panels (ii), this gap appears absent. This is seen more clearly in Fig. 4.8, where the experimental (black) and calculated (red) dispersions are compared directly. Here, the differences between the two cases for the top two valence bands become more apparent. For the experimental dispersion, the gap is maintained across the full mBZ, coming to a minimum around the γ point. We quantify this by fitting to EDCs at γ (Fig. 4.8(c)), in the same way as in Section 4.3, giving a value of $\Delta_h = 46 \pm 5$ meV. This is significantly greater than the gap predicted by the HkpTB model of $\Delta_h = 5$ meV, though there is agreement that the gap is a minimum at γ. The experimental and calculated dispersions also show agreement in the shape of the top valence band. This is quantified by a bandwidth, E_w, given by the difference between the band maximum and minimum. From experiment this was found to be $E_w = 31 \pm 5$ meV, while from the calculation the predicted value was $E_w = 33$ meV. This partial agreement shows that at least some of the experimental results are being captured in the simulations.

It is important to note that the HkpTB model does not take into account the effects of lattice relaxations, where the atoms of the individual layers reposition themselves to preferentially form domains of AB and BA stacking [202, 203]. This is expected to become significant at small twist angles close to the magic-angle and can affect the resulting electronic structure [194, 204]. For tDBG, Haddadi *et al.* found the gap at γ to increase dramatically when lattice relaxations were included in their calculations (Fig. 4.8(d)) [201]. At 1.5°, they predicted $\Delta_h \sim 40$ meV, consistent with our experimental value, while their value for the width of the flat band is also inline with the results stated here. This highlights limitations within the HkpTB model, where deviations from experiment can be expected for twist angles $\lesssim 2°$. Previously, it was also reported that a flat band in tDBG was only possible through application of a vertical displacement field [205], which these results directly disprove.

So far, the electronic structure of twisted graphene has been investigated under standard ARPES operating conditions. However, many reports in the literature integrate gate electrodes to tune the properties of twisted graphene through electrostatic doping [9, 10, 101, 102]. In the next section, we use ARPES with *in-situ* gating to directly measure the band structure of tMBG under these conditions and investigate changes with applied gate voltage.
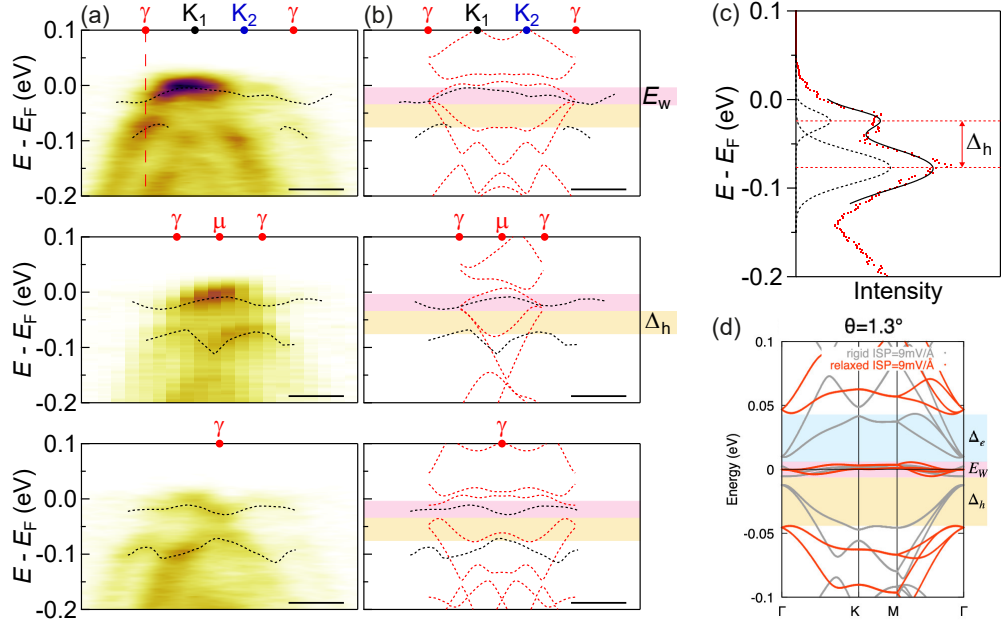
Figure 4.8: a) Energy-momentum cuts taken along the black dashed lines in Fig. 4.7(a), overlaid with the extracted experimental band dispersions (dashed black lines). b) Comparison between experimental (black) and calculated (red) band dispersions for 1.5° tDBG. Calculated band dispersions are from the HkpTB model. Scale bars are 0.05 Å^{-1}. c) EDC along the vertical dashed line in (a). Solid black line is a fit to the data using a linear combination of two Gaussian functions. Dashed black lines show individual Gaussian peaks, whose separation gives the gap size, Δ_{h}. d) Calculated band structure of 1.3° tDBG for a rigid and relaxed crystal lattice, taken from [201].

4.5   Gate-dependent electronic structure of tMBG

To investigate the gate dependence of the electronic band structure of twisted graphene, samples were fabricated with an integrated graphite back gate, performed by Astrid Weston at the National Graphene Institute, University of Manchester. This is shown schematically in Fig. 4.9(a). As outlined in Section 2.3.2, the hBN support layer is used as a dielectric, and separate gate and ground electrodes are deposited onto the graphite and twisted graphene layers, respectively. The metal deposition was patterned using a TEM grid shadow mask to eliminate contamination that can be introduced through the use of conventional lithography photoresists. The sample is mounted using a UHV compatible epoxy into an 8-leg chip carrier, as seen in Fig. 4.9(b). Wire bonds connect the gate and ground electrodes to contact pads of the chip carrier. The chip carrier can then be slotted into a custom-made sample plate that electrically connects the chip carrier legs to electrode blocks on
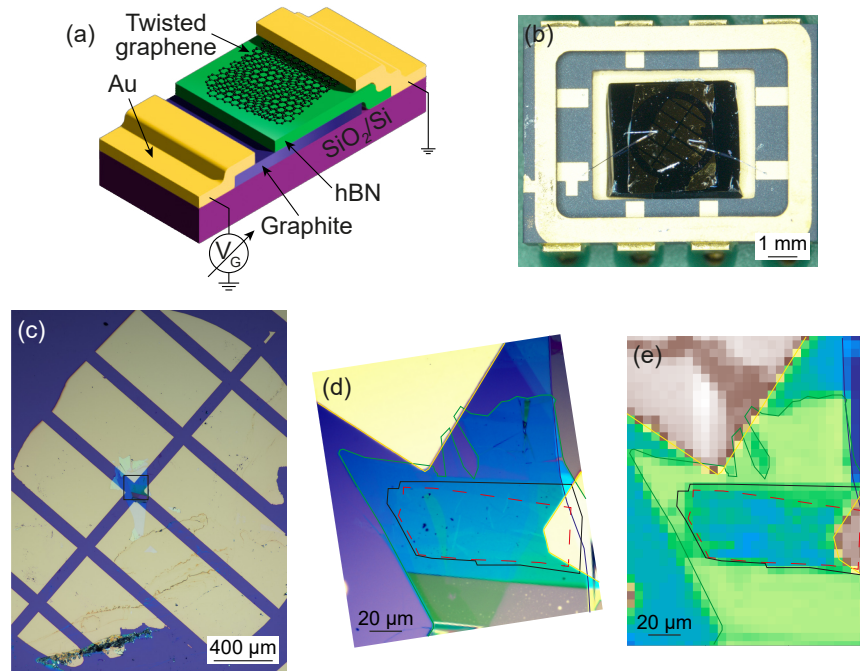
Figure 4.9: a) Schematic of a gated twisted graphene sample. b) Optical image of a gated sample mounted in a chip carrier with wire bonds between sample contacts and chip carrier pads. c) Low-magnification optical microscope image of the gated sample in (b). d) High-magnification optical microscope image from the black box region in (c). The graphene (black), Au contacts (yellow), hBN (green) and graphite back gate (indigo) regions have been outlined. The red dashed line marks the twisted graphene region. e) SPEM image of the sample region in (d).

the plate. These blocks contact the feed-through connections within the ARPES chamber, allowing the sample to be electrically biased *in situ*.

Figs 4.9(c) and (d) are optical images from an example gated tBG sample. The electrode at the top of Fig 4.9(d) is deposited on to the graphite back gate and is used as the gate electrode. The electrode on the right side contacts the twisted graphene region and is connected to ground. The large lateral size of the electrodes and their regular arrangement aids in finding the sample in ARPES, as the SPEM images can be easily interpreted (Fig 4.9(e)). Clearly, however, great care must be taken when positioning the shadow mask to prevent creation of a short. Even when the electrodes have been deposited correctly, shorts are still possible, as was the case for the sample shown here. This most likely comes from leakage through the hBN that was caused by accidental discharge through the sample, permanently damaging the dielectric.

One successful gated sample was that of $3.4 \pm 0.1°$ 1+2 twisted graphene.
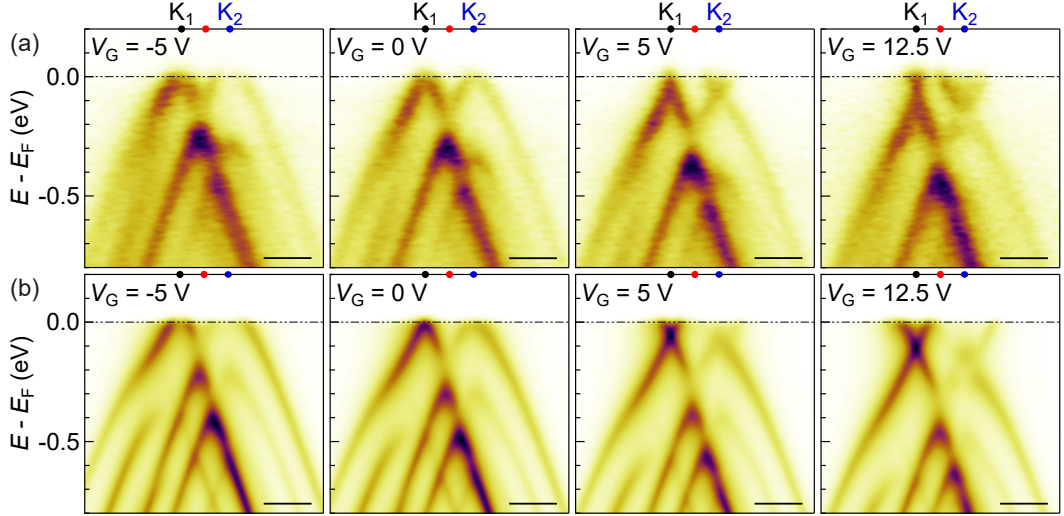
Figure 4.10: a) ARPES energy-momentum cuts of $3.4 \pm 0.1°$ 1+2 twisted graphene taken along the $\mathbf{K_1} \rightarrow \mathbf{K_2}$ direction at the labelled gate voltages. b) Simulated ARPES spectra of $3.4°$ 1+2 twisted graphene at the labelled gate voltages. Scale bars are 0.1 Å^{-1}.

The hBN dielectric thickness was $d = 26$ nm and the back gate voltage, V_G, was able to be varied between -5 V to 12.5 V. Selected ARPES spectra between this range are shown in Fig. 4.10(a). The bands can be seen to move relative to the chemical potential with applied gate voltage, shifting the Dirac points below E_F for $V_G > 0$ and populating the conduction band with electrons (n–doping). Similarly, the Dirac points shift above E_F for $V_G < 0$ and populate the valence band with holes (p–doping). The bilayer Dirac point can be seen to shift more than that of the monolayer, consistent with the bilayer being the bottom graphene layer and, hence, closer to the back gate. This also indicates partial screening of the back gate [206] and a displacement field across the graphene layers that opens a gap at the bilayer Dirac point [28, 207]. The change in the relative alignment of the monolayer and bilayer bands also affects the positions of the anti-crossings in energy and momentum, which can subtly change the hybridisation between the layers.

The effects of electrostatic gating can be incorporated into the HkpTB model by use of a self-consistent analysis of interlayer potentials [206]. An outline of this process for the case of 1+2 twisted graphene is as follows. The electric displacement field, D, can be calculated from the applied gate voltage using

$$D = \frac{V_G C_G}{2\varepsilon_0}, \tag{4.5.1}$$

where C_G is the back gate capacitance and ε_0 is the vacuum permittivity [102]. Similarly, the total charge density, n, is given by

$$n = \frac{\varepsilon_0 \varepsilon_{\mathrm{hBN}} V_G}{e d_{\mathrm{hBN}}}, \tag{4.5.2}$$

where $\varepsilon_{\mathrm{hBN}} = 4$ is the hBN dielectric constant [208], d_{hBN} is the hBN dielectric thickness and e is the electron charge, and is used to determine E_F. Starting with charge neutrality, the initial interlayer potentials, $u_{l,l'}$, where l and l' denote adjacent layers, are given by

$$u_{l,l'} = \frac{e d_{l,l'} D}{\varepsilon_0 \varepsilon_z}, \tag{4.5.3}$$

where $d_{l,l'}$ is the spacing between layers l and l' and ε_z is the out-of-plane dielectric susceptibility. For the case of 1+2 twisted graphene, there are three layer indices: t for the top layer, referring to the monolayer graphene, m for the middle layer, referring to the upper layer of the bilayer graphene, and b for the bottom layer, referring to the lower layer of the bilayer graphene. As taken from [206], we use the parameter set $d_{t,m} = 3.44$ Å, $d_{m,b} = 3.35$ Å, $\varepsilon_z = 2.5$ for the twisted interface and $\varepsilon_z = 2.6$ for the aligned interface. The interlayer potentials are then introduced into the Hamiltonian using

$$\mathcal{H}_{1+2} \to \mathcal{H}_{1+2} + \begin{pmatrix} 0 & 0 & 0 & 0 & 0 & 0 \\ 0 & 0 & 0 & 0 & 0 & 0 \\ 0 & 0 & -u_{t,m} & 0 & 0 & 0 \\ 0 & 0 & 0 & -u_{t,m} & 0 & 0 \\ 0 & 0 & 0 & 0 & -(u_{t,m} + u_{m,b}) & 0 \\ 0 & 0 & 0 & 0 & 0 & -(u_{t,m} + u_{m,b}) \end{pmatrix}. \tag{4.5.4}$$

The modified Hamiltonian provides a new set of wavefunctions, Ψ, whose amplitudes can be used to calculate charge densities on each layer, n_l, using the equation

$$n_l = 2 \int_{\mathrm{BZ}} \frac{d^2 k}{(2\pi)^2} \sum_\beta \left[(|\Psi_{l,A}^\beta(k)|^2 + |\Psi_{l,B}^\beta(k)|^2) f(E_\beta - E_F) - \frac{1}{2} \right], \tag{4.5.5}$$

where β is the band index, E_β is the energy of band β and $f(E_\beta - E_F)$ is the Fermi-Dirac function. New values for the interlayer potentials can then be calculated which

include these layer densities, as given by:

$$u_{t,m} = \frac{ed_{t,m}D}{\varepsilon_0\varepsilon_z} + \frac{ed_{t,m}}{\varepsilon_0\varepsilon_z}\left[\frac{e(n_t - n_m)}{2}\frac{1+\varepsilon_z}{2} - \frac{en_b}{2}\right],$$
$$u_{m,b} = \frac{ed_{m,b}D}{\varepsilon_0\varepsilon_z} + \frac{ed_{m,b}}{\varepsilon_0\varepsilon_z}\left[\frac{e(n_m - n_b)}{2}\frac{1+\varepsilon_z}{2} + \frac{en_t}{2}\right].$$

(4.5.6)

These new interlayer potentials are then put back into the Hamiltonian and the process is iterated until the parameters converge, giving a self-consistent approach to the effect of the applied gate voltage.

Fig. 4.10(b) shows simulated ARPES spectra at varying V_G that have been calculated using the self-consistent process, performed by Andrew McEllistrim at the National Graphene Institute, University of Manchester. These were calculated for the same sample geometries as the experimental data (3.4° 1+2 twisted graphene with a hBN thickness of $d_{hBN} = 26$ nm). There is good qualitative agreement between the two sets of spectra, with the Dirac point energy shifts being of similar magnitude across the different values of V_G.

To better quantify these changes with applied gate voltage, the band dispersions for the monolayer and bilayer cones close to the Dirac point were extracted for each measured gate voltage. This is summarised in Fig. 4.11(a). The band positions were measured by fitting MDCs to Lorentzian functions (Fig. 4.11(b)) over a small energy window close to E_F, so as to avoid parts of the spectra that show interaction effects. Fitting the extracted positions to the low-energy graphene dispersions provides the Dirac point energies, E_D^{ML} and E_D^{BL}, and charge carrier densities, n_{ML} and n_{BL}, for the monolayer and bilayer graphene, respectively, as demonstrated in Section 3.2. Additionally, the gap at the bilayer Dirac point, Δ, is extracted from an EDC at the $\mathbf{K_2}$ point by fitting of Gaussian functions (Fig. 4.11(c)) in the same way as the hybridisation gaps were measured in Section 4.3. The hybridisation gap sizes for tMBG, δ_1 and δ_2, were also determined here for the different gate voltages.

The mentioned quantities are summarised in Fig. 4.12(a). The plotted bands have been calculated using the HkpTB model, emphasising the main effects from the applied gate voltage. E_D^{ML} and E_D^{BL} shift relative to E_F due to electrostatic doping in the graphene layers. E_D^{BL} also shifts more relative to E_D^{ML}, indicating a displacement field between the layers. This change in relative alignment results in subtle changes in the size of the hybridisation gaps, δ_1 and δ_2. The field across the layers additionally opens a gap, Δ, at the Dirac point of the bilayer [28, 207].

The change in Dirac point energies relative to E_F are plotted in Fig. 4.12(b), where data points correspond to experimental values determined by fitting to the
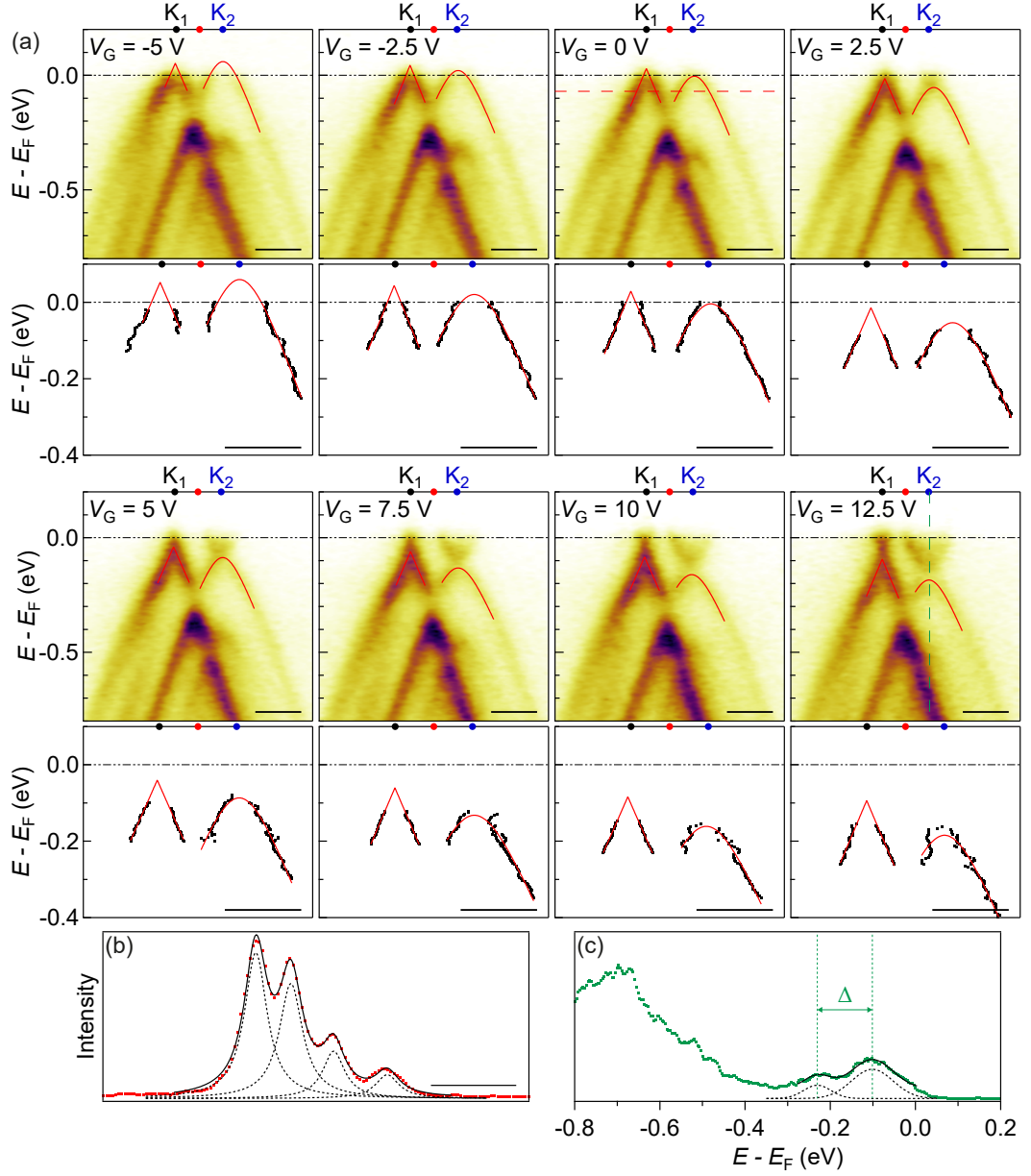
Figure 4.11: a) (Top panels) ARPES energy-momentum cuts of $3.4 \pm 0.1°$ 1+2 twisted graphene taken along the $\mathbf{K_1} \rightarrow \mathbf{K_2}$ direction and (bottom panels) extracted band positions (black points) for the monolayer and bilayer cones at the labelled gate voltages. Red lines are fits to the extracted band positions using the low-energy dispersion approximations for monolayer and bilayer graphene. b) MDC extracted along the horizontal red dashed line in the $V_G = 0$ V spectrum, fit to a linear combination of Lorentzian functions (solid black line). Scale bars are 0.1 Å^{-1}. c) EDC extracted along the vertical dashed green line in the $V_G = 12.5$ V spectra, fit to a linear combination of Gaussian functions. The separation between Gaussian peaks gives the bilayer gap size, Δ.
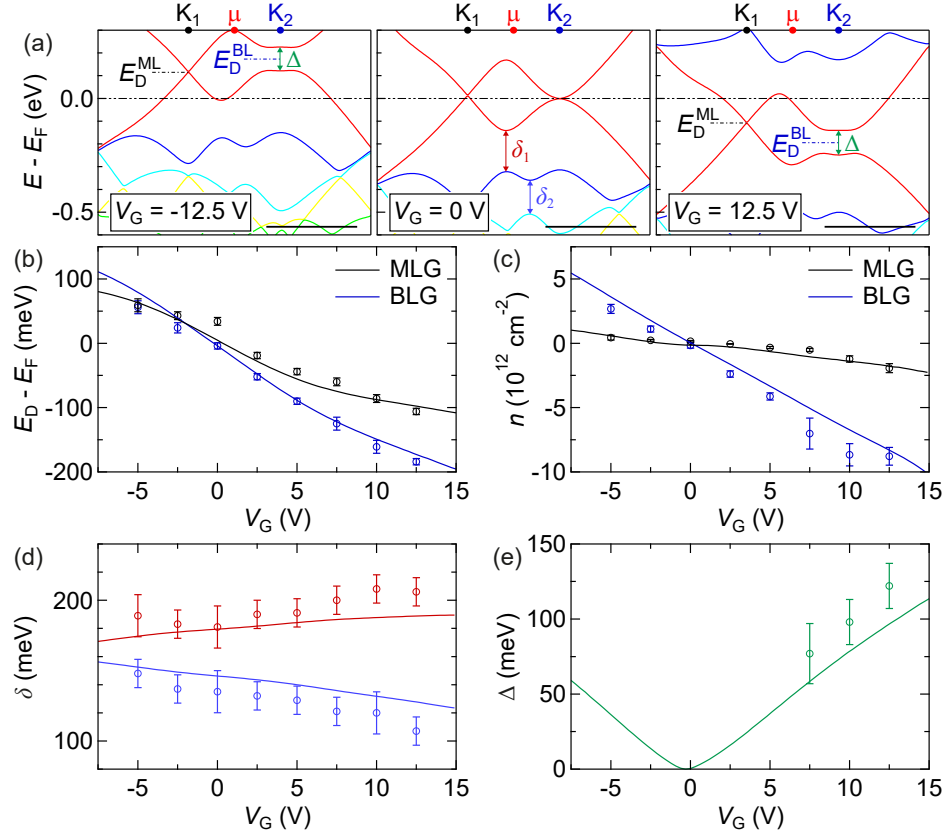
Figure 4.12: a) Band structure along the $\mathbf{K_1} \rightarrow \mathbf{K_2}$ direction at different V_G. Labels show the Dirac point energies, E_D, hybridisation gap sizes, δ, and bilayer gap size, Δ. Scale bars are 0.1 Å^{-1}. b,c) Dirac point energies, E_D, and carrier densities, n, respectively, for the monolayer (black) and bilayer (blue) Dirac cones as a function of V_G. d) Hybridisation gap sizes, δ_1 (red) and δ_2 (blue), as a function of V_G. e) Energy gap size, Δ, at the bilayer Dirac point as a function of V_G. Data points are experimental values extracted from the ARPES spectra, while solid lines are calculated values from the HkpTB model.

ARPES data (Fig. 4.11) and lines are from the simulations. The experimental behaviour is well replicated by the theory. In general, E_D shifts below E_F for positive gate voltage, corresponding to electron doping, while E_D shifts above E_F for negative gate voltage, corresponding to hole doping. Note, E_D^{ML} and E_D^{BL} do not pass through zero at $V_G = 0$ in the calculated values due to a nonzero value for γ_4, as well as inclusion of an on-site energy difference between A and B sites of 25 meV, which has the effect of adding electron-hole asymmetry at zero gate voltage [193]. E_D^{BL} shifts more than E_D^{ML}, where, at $V_G = 15$ V, there is almost a 100 meV difference between the two Dirac energies. For individual gated graphene layers under the same conditions, one would expect E_D^{ML} to shift more than E_D^{BL} due to

the increased density of states in bilayer graphene [17, 133, 183]. The reversal of this behaviour seen here indicates a screening of the back gate by the underlying bilayer graphene. This screening effect is also evidenced in the change in carrier densities for the two layers, shown in Fig. 4.12(c). Both n_{ML} and n_{BL} scale approximately linearly with V_G, but at a much faster rate in the bilayer graphene. At $V_G = 15$ V, the carrier density in the bilayer is roughly four times greater than that in the monolayer. The majority of the induced charge becomes localised in the bilayer, which then acts to screen the monolayer graphene from the back gate, resulting in the observed trend.

The variation in the size of the hybridisation gaps due to the applied gate voltage is plotted in Fig. 4.12(d). As mentioned, the shift of the bilayer cone relative to that of the monolayer results in a change of the position of the anti-crossings in reciprocal space. This can affect the interlayer coupling, which in turn changes the hybridisation gap sizes. Note, we believe this change in interlayer coupling to be due to a change in the overlap between particular wavefunctions, rather than due to changes in the SWM coupling parameters themselves. An additional energy gap opens at the bilayer Dirac point due to the displacement field, which varies roughly linearly with V_G (Fig. 4.12(e)) consistent with previous reports of a field-dependent band gap in bilayer graphene [28, 207]. Experimentally, this gap could only be resolved for $V_G \geq 7.5$ V. Across all band parameters, there is good agreement between the experimental results and the calculations, validating the model used.

These results highlight a potential challenge in using ARPES with *in-situ* gating to study filling-factor dependent phases in magic-angle systems. Transport measurements use both top and back gates to separately control the displacement field and doping in the system [101, 102]. A top gate is not possible to use in ARPES due to the surface sensitivity. As a result, a displacement field and electrostatic doping must be applied simultaneously through use of a back gate, limiting which parts of the phase diagram can be accessed. The band shifts observed in our results also bring into question how well a flat band is maintained when applying a back gate voltage, or if the change in band alignments would result in an increased bandwidth.

4.6   Summary

The results presented here show that high-resolution μARPES spectra, directly compared to simulated spectra, can give an effective and quantitative test of the electronic structure predictions for twisted graphene systems. By extracted key parameters from the spectra, such as hybridisation gaps, as a function of twist angle

and number of layers, we have tested the ability of the HkpTB model to describe different few-layer graphene structures. This has also provided insight into the nature of photoemission from these twisted systems and of the moiré interaction.

A simple model is proposed to explain the intensity hierarchy of replica bands. In reciprocal space, electrons scatter from the **K** points of one valley of the primary BZ to replica points around another valley. In real space, this causes a tunnelling of electrons from one layer to another, resulting in attenuation of particular replica intensities when the electron is localised in the lower layer. The replica intensities increase for $\theta < 3°$ due to an increase in the scattering probability, but remain relatively constant for larger twist angles. In addition to this, hybridisation gap sizes, δ, were extracted from EDCs as a quantifiable parameter in the electronic structure of twisted graphene, as well as a measure of the coupling strength. At large twist angles, δ was greatest in tBG, but decreased rapidly for $\theta < 3°$ in all stacking arrangements. Across all datasets, the experimental results were well reproduced by the simulations, validating the HkpTB model as well as our choice of values for the SWM parameters.

An approximately flat band was observed at E_{F} in 1.5° tDBG gapped from the lower lying valence band states. This exhibited a weak dispersion with minima at the γ points of the mBZ and a bandwidth of $E_{\mathrm{w}} = 31 \pm 5$ meV. This was in agreement with predictions from the HkpTB model, however, the calculations lacked a clear gap at γ between the flat band and the next valence band, which was clearly seen in the experimental ARPES data. We measured this gap to be $\Delta_{\mathrm{h}} = 46 \pm 5$ meV. This is inline with predictions by Haddadi *et al.* when lattice relaxations are included, increasing the gap to $\Delta_{\mathrm{h}} \sim 40$ meV for 1.5° tDBG [201]. This highlights the importance of lattice relaxations in the electronic structure of twisted systems at small twist angles.

Finally, we have explored changes in the electronic structure of 3.4° 1+2 twisted graphene with applied back gate voltage. The Dirac energy shifts relative to E_{F} as a function of V_{G}. Due to being closer to the back gate, the bilayer accumulates the majority of the induced charge and screens the applied field from the monolayer, resulting in a greater shift in $E_{\mathrm{D}}^{\mathrm{BL}}$ compared to $E_{\mathrm{D}}^{\mathrm{ML}}$ for a particular gate voltage. This also creates a displacement field across the layers which opens a gap at the bilayer Dirac point. Experimental results are compared to calculations through use of a self-consistent method of determining interlayer potentials. Quantitative agreement was achieved between experiment and theory without requiring fitting to the experimental data or modification of the SWM parameters.

These results demonstrate one of the most in-depth single studies of the

electronic structure of twisted graphene using ARPES. They provide excellent validation for the HkpTB model in predicting the band structure of different twisted graphene systems across a range of twist angles, while also revealing deviations at small twist angles. Resolution, both in reciprocal space and real space, is the key factor in being able to critically study these systems using ARPES. Advances in instrumentation and sample fabrication will improve present resolution limits, allowing electronic structure features in twisted graphene to be probed more accurately. This could provide further insight into the flat band topology and the effect of lattice relaxations at small twist angles, as well as revealing band renormalisations due to many-body effects [194]. On top of this, *in-situ* gating of magic-angle twisted graphene would be particularly interesting, despite the issues mentioned previously, and may be able to demonstrate flat band renormalisation effects coming from changes in band occupancy.

Chapter 5

Towards twist-dependent electronic structure measurements of CrSBr

5.1 Introduction

The study of 2D magnetic systems has become increasingly popular in recent years. The ability to maintain magnetic order down to the few-layer [40] or even monolayer limit [41–44] opens up a number of opportunities to manipulate the magnetic properties through application of external fields and fabrication into heterostructures [47, 48, 89], as well as offering the control of both charge and spin carriers to develop magnetic devices [87, 88]. As with any 2D material, there also exists the possibility of twisting magnetic layers relative to each other, producing a magnetic moiré system. These have been predicted to host exotic magnetic phases such as moiré skyrmions [209, 210] and non-collinear spin states [211]. Recently, moiré magnetism has been realised experimentally through twisted layers of CrI_3, which have displayed coexisting ferromagnetic and antiferromagnetic domains that can be tuned both by twist angle and electrostatic gating [110, 212–214]. It is expected that further moiré systems incorporating 2D magnetic layers will be reported in the near future.

As with early twisted graphene reports, theoretical input will be key to guiding experimental studies of twisted 2D magnets. This relies on a base understanding of the properties of the individual magnetic layers, including their electronic structures. Calculations of the electronic structures of 2D magnetic materials are far from trivial, however, and can be highly sensitive to the choice of approximation

scheme [215]. Comparison to experimental results is thus of great value, though high quality electronic structure measurements of 2D magnetic systems from ARPES are still lacking [63, 64, 135, 136]. Fabrication of few-layer flakes suitable for ARPES is particularly challenging due to many 2D magnetic materials having poor ambient stability [49, 50], requiring specialist fabrication and transfer methods. However, even measurements of bulk crystals come with their own set of problems. Semiconducting 2D magnets become highly insulating at the low temperatures required to reach the magnetically ordered states, meaning they are prone to charging effects during photoemission. As such, many ARPES reports of 2D magnets have focused on high temperature measurements within the paramagnetic state [63, 136, 137], and have been unable to investigate changes in the electronic structure on entering the magnetic phase.

In the past few years, CrSBr has presented itself as an exciting new addition to the family of 2D magnets due to its enhanced stability [51] and relatively high Néel temperature of $T_N = 132$ K in the bulk, with an even higher Curie temperature of $T_C \sim 150$ K expected in the monolayer limit [54], making it an ideal candidate for ARPES. Unsurprisingly, ARPES results of bulk CrSBr have already been reported by Bianchi *et al.*, however, they too suffered from considerable charging effects, unable to measure below $T \approx 170$ K and observe the electronic structure in the antiferromagnetic phase [63]. In this Chapter, we present a method to overcome these charging effects by exfoliating bulk CrSBr flakes onto a conductive gold surface. By finding flakes of optimal thickness where the resistance to ground is low, the bulk electronic structure of CrSBr can be measured at temperatures as low as $T \sim 30$ K, well below T_N, with negligible influence from charging.

We begin this Chapter with an overview of the sample fabrication method and resulting sample layout, followed by an explanation of how optimal flakes can be located and checked for charging effects at low temperatures. ARPES spectra from CrSBr in the antiferromagnetic phase are then presented as cuts along high symmetry directions, highlighting key features and how the appearance of these changes with photon energy and polarisation of light. The dimensionality of CrSBr, as well as its band gap, will also be discussed. Next, we investigate the temperature-dependence of the electronic structure, demonstrating changes related to the magnetic ordering, before finishing with an outline of future work surrounding band structure measurements of CrSBr.

5.2   Exfoliation of CrSBr flakes onto gold

Samples of CrSBr were prepared by exfoliation using a template-stripped gold method, introduced in Section 2.3.3. A summary of this is presented in Fig. 5.1(a). Templated-Au is glued to a silicon wafer using the Opti-tec 5054-1 two-part epoxy. This particular epoxy was chosen as it is UHV compatible and has a relatively high glass transition temperature, important for maintaining a flat gold surface during heating processes. Templates of both silicon and mica (panel (i)) were used. As the adhesion of the gold is stronger to the epoxy than to the template, the templated-Au preferentially cleaves at the gold-template interface, leaving a fresh surface of gold covering the epoxy (panel (ii)). A thin strip of Kapton tape is used to pick up bulk flakes of CrSBr before bringing them into contact with the gold surface (panel (iii)). The sample is then heated on a hot plate at 100°C for 5 minutes to remove contamination between the CrSBr flakes and Au surface, improving adhesion. All steps are performed within an argon filled glove box to avoid contamination by oxygen and water vapour and maintain a fresh gold surface for longer. Following this, samples are transferred through air from the glove box into the load lock of the nanoARPES endstation. After pumping to a pressure $< 1 \times 10^{-7}$ mbar, the Kapton tape is removed using a wobble stick, exfoliating the CrSBr *in situ*. This minimises surface contamination and removes the need to anneal the sample in vacuum.

The downside of this technique is that there is no prior knowledge of the location of exfoliated flakes before performing ARPES. Detailed photoemission mapping is required to find regions of interest, which can be time consuming. Though not shown here, an effective way to map a large area of an exfoliated CrSBr sample using SPEM is to image using the core levels of Cr, S or Br. For example, Br has shallow core levels around 69 eV and 70 eV [216]. Using a photon energy greater than the core level energy (and accounting for the work function) will excite photoelectrons from the core levels. These can be detected by the electron analyser and used to image the sample. In this way, only parts of the sample containing Br (i.e., the CrSBr flakes) will show up on the SPEM image, providing a simple way to easily pinpoint exfoliated flakes. Using this technique, a rough large scale image of the sample can be produced relatively quickly and used to identify regions of interest that may have promising flakes.

Fig. 5.1(b) shows a SPEM image of one particular region of interest containing a CrSBr flake. We can also confirm the region belonging to the CrSBr flake by analysing the individual ARPES spectra. Fig. 5.1(c) is the ARPES spectrum from a position on the CrSBr flake. The E_F reference on the energy scale has been

96
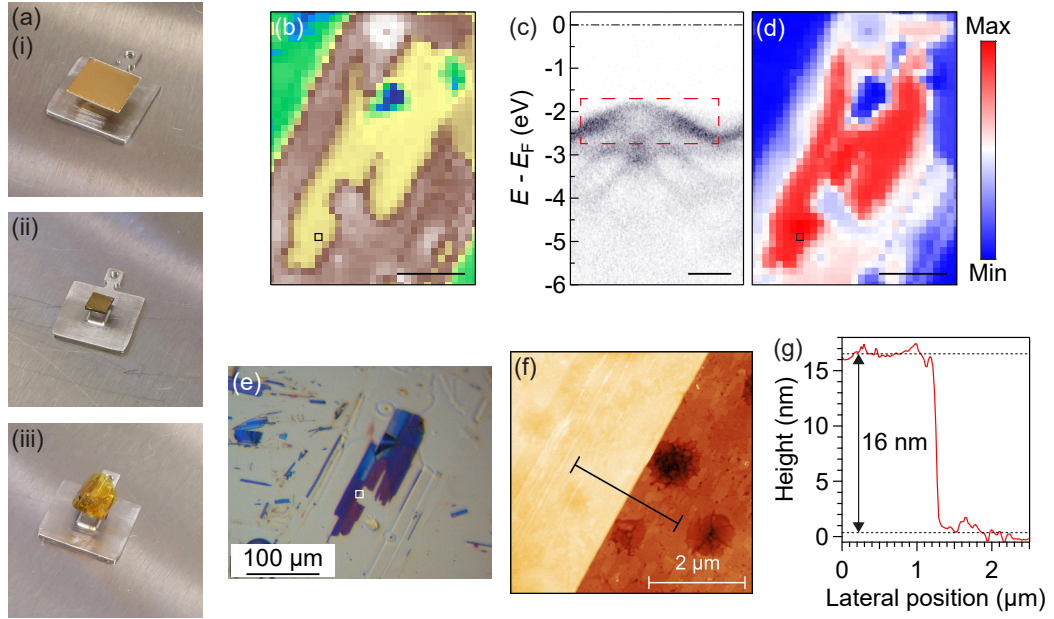
Figure 5.1: a) Photograph summary of the template-strip exfoliation method used to prepare samples of CrSBr. i) Mica coated with Au is glued using epoxy to a small Si wafer attached to a sample holder, with the exposed Au side in contact with the epoxy. ii) The mica is mechanically removed using a scalpel, leaving an exposed Au surface. iii) Kapton tape covered in bulk flakes of CrSBr is stuck to the Au surface. The Kapton tape is rolled into a loop to allow it to be removed within vacuum. All steps in (a) were performed within a glove box with an Ar atmosphere. b) SPEM image of an exfoliated CrSBr flake on Au. Scale bar is $50\,\mu\mathrm{m}$. c) ARPES spectrum from the point marked by the black box in (b). Scale bar is $0.5\ \mathrm{\mathring{A}}^{-1}$. d) SPEM image obtained by integrating over the red dashed box in (c). e) Optical image of the CrSBr flake in (b). f) AFM image taken from the white box region in (e). g) AFM height profile taken along the black line in (f).

determined from spectra from the gold surface which shows clear intensity up to the Fermi level. Integrating over an (E, k) region containing CrSBr bands (red dashed box) highlights the dimensions of the flake (Fig. 5.1(d)). Detailed SPEM images such as this are important for finding and characterising flakes after the ARPES measurement. An optical image of the CrSBr flake found from SPEM is shown in Fig. 5.1(e). Visible differences in colour signify variations in thickness across the flake, which are not visible within the SPEM image. The exact thickness can be confirmed by AFM (Fig. 5.1(f)), which revealed the thinnest regions of this flake to be 10–20 nm (Fig. 5.1(g)).

For these samples, the thickness of the CrSBr flake plays an important role in whether a particular region is suitable to measure from. Flakes which are too thin

are unsuitable for two reasons. The first is that the gold surface may not be perfectly flat. Thin flakes, particularly those of only a few atomic layers, will conform to this surface roughness. This results in random distortion of the local atomic structure, affecting the long range periodicity and blurring the ARPES spectrum. In thicker flakes, this distortion gets mechanically relaxed through the layers, meaning the top few layers measured by ARPES are unaffected. The second is that interactions between a clean and flat gold surface and the CrSBr can result in charge transfer and hybridisation effects that change the electronic structure [217, 218]. Though interesting, this is not what we are aiming to measure. Again, these effects are negligible at the top surface of thick flakes. As there is no information about the thickness of flakes prior to ARPES, whether a flake is suitable for measurement must be determined from the ARPES spectra. Generally, it is easy to tell if a flake is too thin because either the CrSBr bands will appear weak and broad due to the surface roughness, or interactions effects from the gold will be visible.

Similarly, the CrSBr flakes cannot be too thick due to charging effects [63]. At low temperatures, the resistivity of bulk semiconductors can be very high. If the distance to ground is long, the rate that emitted photoelectrons are re-populated can be slow, leading to a build-up of positive charge at the crystal surface. The resulting electrostatic forces effectively reduce the kinetic energy of the emitted photoelectrons, causing an energy shift of the measured valence bands, as well as additional broadening. By exfoliating onto gold, flakes of CrSBr with a range of thicknesses can be obtained, some of which will have a short enough distance to ground (the gold surface) that charging is negligible.

The optimal flake is on the order of 10s of nanometres thick. Flakes which are hundreds of nanometres can be easily recognised from ARPES, as charging results in a large clearly observable shift in the measured valence band energy. Intermediate thicknesses, however, where the charging is small, are more difficult to identify. One method of checking if a particular region is charging is to look for band shifts as a function of beam intensity. For the nanoARPES beamline, the intensity of the photon beam reaching the sample is controlled by the exit slit (Section 2.2.2). The exit slit clips the beam, allowing some proportion through a small opening. Adjusting the size of this opening allows control of the beam intensity. For a flake which is charging, a greater beam intensity produces more photoelectrons, increasing the build-up of charge and the amount the valence bands shift by. Hence, the valence bands should shift systematically as a function of exit slit size.

Using this knowledge, we can perform a simple check on any particular flake to see if it is charging. An example of this is shown in Fig. 5.2 for the flake in
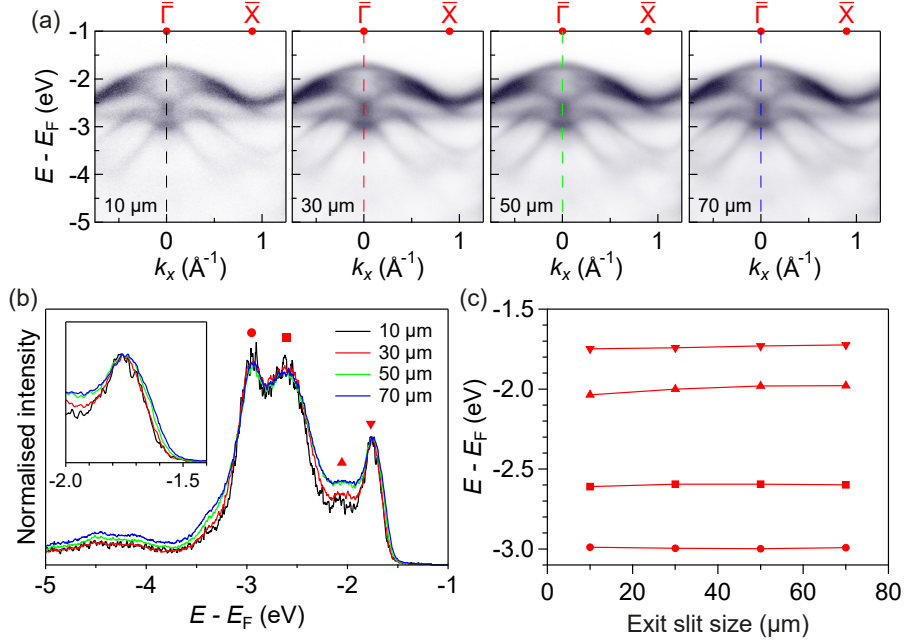
Figure 5.2: a) ARPES spectra of CrSBr along the $\overline{\Gamma} \rightarrow \overline{X}$ direction measured using LH polarised light at 53 eV and a sample temperature of 33 K for varying exit slit size. b) EDCs at $\overline{\Gamma}$ taken from the ARPES spectra in (a) (dashed lines). c) Gaussian peak positions extracted from fits to the EDCs in (b).

Fig. 5.1. Fig. 5.2(a) shows ARPES spectra of CrSBr. These were measured at 33 K from the same position on the sample, with increasing exit slit size. Band shifts due to charging can be quantified by fitting to EDCs at the $\overline{\Gamma}$ point (Fig. 5.2(b)). Each EDC is fit between the energy range -3 eV to -1 eV using a function comprised of four Gaussian peaks, which was the minimum number of peaks required for a good fit.

In general, it was found Gaussian functions gave a better fit to EDC line shapes than Lorentzian functions, suggesting an energy broadening primarily from inelastic scattering. We note a Voigt function would provide the most realistic line shape, however, accurate Voigt fitting can be difficult without a good starting estimate for the respective Gaussian and Lorentzian components. Additionally, an appropriate background function, such as a Shirley background, should be included for accurate fitting, though this can further complicate the fitting procedure, and is expected to only be a small contribution to the overall measured intensity. As such, Gaussian fitting was decided as the most efficient method of extracting the peak positions.

The extracted peak position of each Gaussian is plotted in Fig. 5.2(c). Across

the four spectra, there are no significant band shifts as a function of exit slit size, indicating negligible charging effects. The biggest overall shift is seen for the 2nd lowest energy peak of $\sim$60 meV. This is to be expected, as the 2nd peak is unresolved compared to the other three peaks (an argument could be made to say there is no peak there at all) and so there can be a large variation in the acceptable fit for the 2nd peak, in addition to significant starting bias. As such, a variation of 60 meV is entirely reasonable and it would not be unexpected for the fitting to the 2nd peak to have an error bar on the order of hundreds of meV. The error bars for the other peaks would be much less, however, particularly for the lowest energy peak, as their peak shape is much more defined, and this is clearly reflected in their reduced variation in Fig. 5.2(c).

Accordingly, the observed peak shifts as a function of exit slit are to be expected from a statistical point of view, in addition to possible shifting due to minor degradation of the CrSBr over time from the high intensity photon beam. With this in mind, we can conclude the flake position measured in Fig. 5.2 is not charging at low temperatures and is suitable for ARPES measurements of CrSBr.

CrSBr typically exfoliates as ribbon-like flakes with a preferential long-axis along the a-direction (Fig. 1.5), coming from an in-plane structural anisotropy [45, 56]. This allows the relative orientation of the crystal to be easily identified, which can be matched directly with the orientation in reciprocal space owing to the simple BZ of CrSBr (Fig. 1.5). Using this, flakes could be rotated to align different high symmetry directions with the vertical slit of the analyser (Section 2.2.2), allowing high statistics ARPES spectra to be obtained. The two main high symmetry directions are $\overline{\Gamma} \rightarrow \overline{X}$ and $\overline{\Gamma} \rightarrow \overline{Y}$. These directions are orthogonal to each other, requiring a 90° rotation to change from one measurement geometry to the other. This is beyond the limit of the azimuthal rotation of the sample manipulator, thus requiring different samples to access the two reciprocal space directions. Alternatively, the other high symmetry cut can be extracted from a Fermi surface map acquired through a polar rotation of the analyser, however, for the lower photon energies, this would require a large polar rotation and would be very time consuming. As such, in the next section, we have focused primarily on measurements along the $\overline{\Gamma} \rightarrow \overline{X}$ direction when aligned with the analyser slit, all taken from the same CrSBr flake, allowing us to acquire various spectra under different measurement conditions.
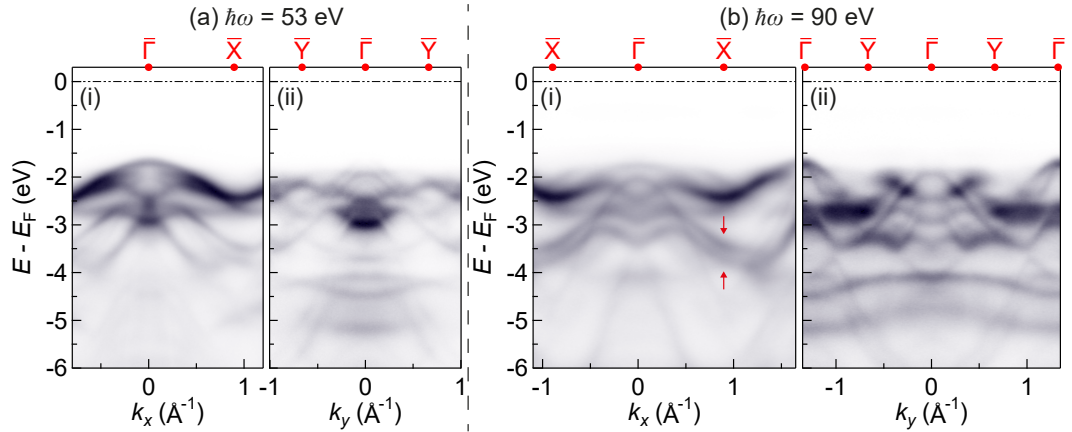
Figure 5.3: ARPES spectra of CrSBr using linear horizontal polarised light at a photon energy of (a) 53 eV and (b) 90 eV along the (i) $\overline{\Gamma} \rightarrow \overline{X}$ and (ii) $\overline{\Gamma} \rightarrow \overline{Y}$ directions, respectively. Sample temperature is 33 K.

5.3 Electronic structure measurements of CrSBr in the antiferromagnetic phase

We now move onto discussing the measured ARPES data from bulk exfoliated flakes of CrSBr in the antiferromagnetic phase. Fig. 5.3 shows ARPES spectra measured using linear horizontal (LH) polarised light along the $\overline{\Gamma} \rightarrow \overline{X}$ and $\overline{\Gamma} \rightarrow \overline{Y}$ directions at two photon energies, 53 eV and 90 eV, respectively. Though somewhat arbitrary, these two photon energies were chosen due to the different ARPES features they highlight. Focusing initially on the 53 eV data (Fig. 5.3(a)) a number of dispersing bands can be observed, which show similarities in their shape along the two recip-rocal space directions. The relative band intensities between panels (i) and (ii), however, are very different.

The major factor contributing to the measured intensity is the orientation of the sample relative to the polarisation of the light. As described in Section 2.2.2, for normal operation, the angle of incidence between the beam and the sample is ap-proximately 45°. In this case, LH polarised light will have electric field components both normal to and in the sample plane. As the sample is azimuthally rotated, the orientation of the in-plane component relative to the crystal lattice changes. Explic-itly, for the $\overline{\Gamma} \rightarrow \overline{X}$ measurements, the in-plane component of the light polarisation points along the b-axis of the crystal, while for the $\overline{\Gamma} \rightarrow \overline{Y}$ measurements it points along the a-axis. In the two cases, the light will couple differently to specific electron orbitals, which in turn affects the measured intensity of bands with that particular orbital character. For completeness, we also reiterate that linear vertical (LV) light

101

only has a component in the sample plane, which is at $90°$ to the in-plane component of LH, and thus, again, will affect the measured intensity of bands depending on their orbital character.

There is a striking difference between the two cases for the intensity of the low energy bands at $\overline{\Gamma}$ in the vicinity of the valence band maximum (VBM). For the $\overline{\Gamma} \to \overline{X}$ measurement there is a clear band reaching a maximum at $\overline{\Gamma}$, whereas for the $\overline{\Gamma} \to \overline{Y}$ measurement this band is highly suppressed. Note, we are careful not to refer to the band in Fig. 5.3(a) panel (i) as the VBM. In the results from Bianchi *et al.*, the VBM was clearest for cuts along $\overline{\Gamma} \to \overline{Y}$, but only from the 2nd BZ and was almost entirely suppressed at the 1st $\overline{\Gamma}$ point [63]. This effect appears reproduced here in the 90 eV data where the 2nd $\overline{\Gamma}$ point is visible and shows greater intensity around the VBM compared to the 1st $\overline{\Gamma}$ point (Fig. 5.3(b)). Bianchi *et al.* proposed this comes from sublattice interference effects, similar to that in graphene that suppresses the intensity of the σ band at Γ of the 1st BZ but not neighbouring BZs [219]. Accounting for the uncertainty imposed by these effects, we estimate the VBM to be at an energy of $E_{\mathrm{VBM}} - E_{\mathrm{F}} = -1.6 \pm 0.1$ eV. This is within error to the value reported by Bianchi *et al.* of -1.51 eV [63], though their measurements were performed at a temperature above T_{N} and may not be directly comparable.

Looking further at the 90 eV data in Fig. 5.3(b), we comment on the abnormal periodicity of certain bands crossing high symmetry points. In particular, the two bands marked by the red arrows at the $\overline{X}$ point of Fig. 5.3(b) panel (i). These bands would be expected to be symmetric about $\overline{X}$, however, the intensity appears to continue to higher binding energies in the next BZ. We hypothesise that this effect comes from a sublattice glide plane symmetry, which causes the observed spectral intensity for particular bands to follow a periodicity double that of the BZ [220]. As will be shown next, combining ARPES measurements of different polarisation reveals the full symmetry at the $\overline{X}$ point.

We next explore the polarisation dependence of the measured ARPES spectra in Fig. 5.4 through the use of linear and circular polarised light, where the energy scale is now referenced with respect to the VBM. Focusing initially on the linear polarisation measurements, The LV spectra is drastically different to that of the LH. Almost all the bands visible using LH are highly suppressed in the LV spectra, with the exception of the high intensity band near $\overline{X}$ at -0.75 eV. Likewise, many bands not present in the LH spectra can be seen clearly using LV, such as the highly dispersing band between -2 eV at $\overline{X}$ and -0.3 eV at $\overline{\Gamma}$ (red arrow), and the set of bands centred on $\overline{\Gamma}$ between -4 eV and -2 eV (red dashed box). This highlights a strong in-plane anisotropy and the requirement to measure using different polarisa-
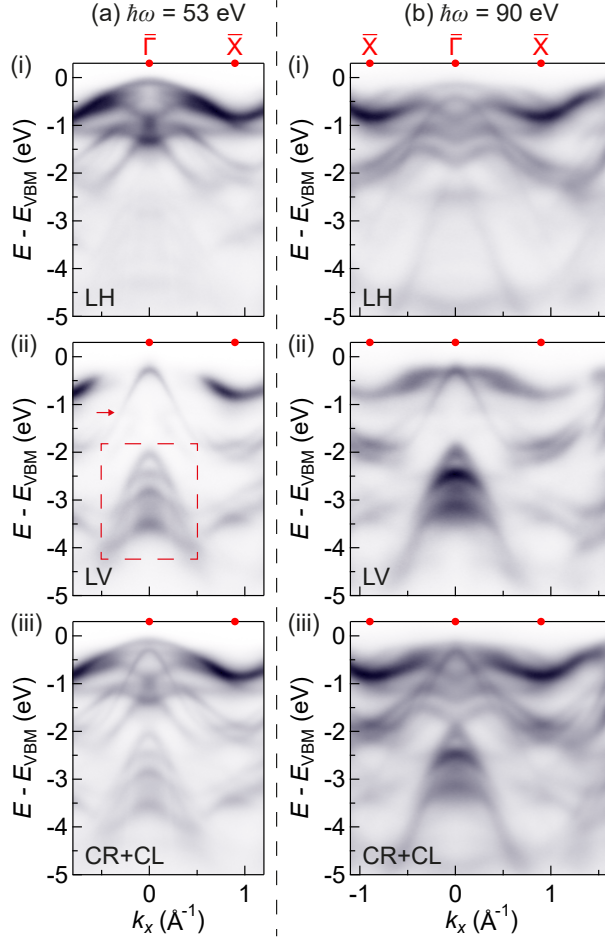
Figure 5.4: a) ARPES spectra of CrSBr along the $\overline{\mathbf{\Gamma}} \to \overline{\mathbf{X}}$ direction at a photon energy of (a) 53 eV and (b) 90 eV using (i) LH and (ii) LV polarised light, respectively. iii) Summation of ARPES spectra measured using circular right and circular left polarised light. Sample temperature is 33 K.

tions and sample geometries to observe the full electronic structure. In Section 5.5, we will briefly discuss how combining extracted band positions from different measurements can be used to build-up a detailed description of the band dispersions, which can be compared directly to theoretical calculations.

Panel (iii) shows the spectrum obtained through the summation of ARPES spectra measured using circular right and circular left polarised light. By combining the two polarisation measurements, more of the electronic structure becomes visible, and appears qualitatively similar to a superposition of the LH and LV measurements. Most notably, the bands around -2 eV at the $\overline{\mathbf{X}}$ point now show the expected symmetry that was absent in the individual LH and LV spectra.
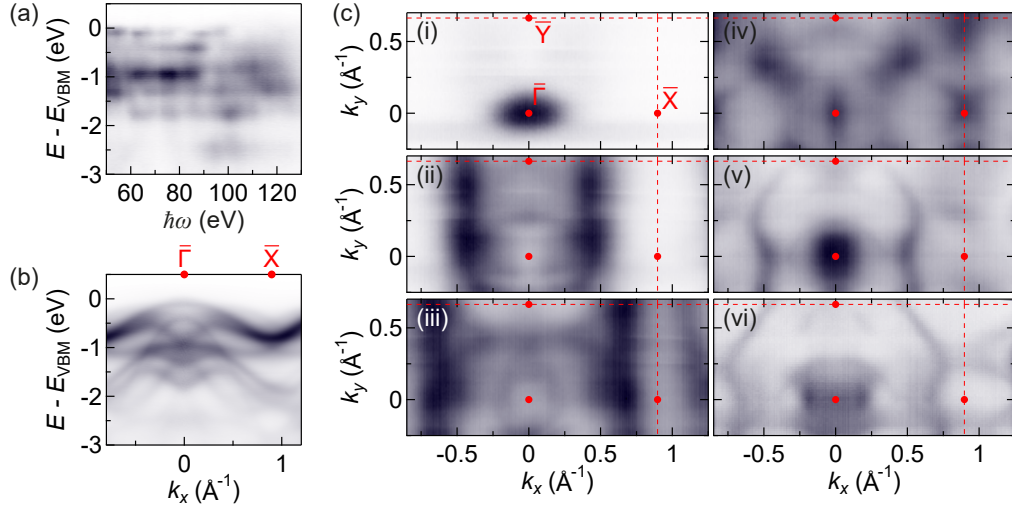
Figure 5.5: a) EDCs at the $\overline{\Gamma}$ point of CrSBr as a function of photon energy. b) Summation of energy-momentum cuts along $\overline{\Gamma} \to \overline{X}$ taken over the photon energy range 50–130 eV. c) Constant energy cuts of CrSBr using 53 eV LH polarised light at $E - E_{\text{VBM}} =$ (i) -100 meV, (ii) -400 meV, (iii) -700 meV, (iv) -1 eV, (v) -1.3 eV and (vi) -1.6 eV, averaged over ± 30 meV of the specified energy. Red dashed lines mark the BZ boundary. Sample temperature is 33 K.

The 53 eV and 90 eV spectra presented in Figs. 5.3 and 5.4 show many differences, demonstrating a clear photon energy dependence on the observed ARPES spectra. From the bulk nature of the measured CrSBr flakes, this could potentially come from a pronounced out-of-plane dispersion of the electronic structure. This is probed further through a systematic scanning of the photon energy from 50–130 eV by 1 eV increments. ARPES spectra were acquired at each photon energy using LH polarised light. EDCs extracted at the $\overline{\Gamma}$ point of each spectra are plotted as a 2D colour map in Fig. 5.5(a). As discussed in Section 2.1.1, varying the photon energy probes the k_z dispersion of a material, which would display as dispersive features in the EDCs at $\overline{\Gamma}$. However, the intensity in Fig. 5.5(a) appears primarily as horizontal streaks, signifying a minimal k_z dispersion. This is supported in Fig. 5.5(b), where, after summing together all spectra from the photon energy scan, clear bands are still observed. This indicates bulk CrSBr is a highly 2D material, with only weak coupling between layers. The changes with photon energy can therefore be attributed to matrix element effects [142]. Band structure calculations from Bianchi et al. also revealed minimal k_z dispersion in the antiferromagnetic phase, however, calculations for bulk ferromagnetic and paramagnetic CrSBr showed significant dispersion in k_z particularly along $\Gamma \to Z$ [63], suggesting the magnetic phase plays a role in the out-of-plane dispersion.

On the topic of dimensionality, some reports have claimed CrSBr to be a quasi-one-dimensional (1D) material [52, 53]. From an electronic structure point-of-view, this can be understood in the conduction band as calculations have shown the $\overline{\Gamma} \to \overline{X}$ bands close to the band edge to be highly non-dispersive [53, 60], in stark contrast to the steeply dispersive $\overline{\Gamma} \to \overline{Y}$ bands, giving it a quasi-1D character. From the perspective of the valence bands, however, CrSBr still shows predominantly 2D character, with bands dispersing in both k_x and k_y. We illustrate this in Fig. 5.5(c) by a series of constant energy cuts, where bands can be seen to disperse throughout the $k_x - k_y$ plane.

Overall, the electronic structure of CrSBr is highly complex, with a large number of dispersing valence bands within a relatively small energy window. Comparison with theory is necessary to fully appreciate the origins of these different bands and how they relate to the magnetic order. A collaboration with theorists is currently ongoing, but is outside the scope of this thesis. Thus, for simplicity, we will focus on only a few of the most notable bands when discussing the temperature dependence of CrSBr in Section 5.4.

5.3.1 What is the band gap of CrSBr?

An important parameter in the electronic structure of semiconductors is the band gap. The general consensus in the literature is that the band gap of CrSBr is around 1.5 eV [45, 53–55, 57]. This is supported by optical measurements that found photoluminescence peaks in the range 1.25–1.37 eV [45, 52–54, 56, 221] and a photoreflectance peak around 1.4 eV, corresponding to a direct optical transition [57]. Additionally, STS measurements reported a band gap of 1.5 ± 0.2 eV [53, 54], in line with the optical results. This is somewhat in conflict with the results presented here. Note, conventional ARPES does not measure the conduction band so cannot give a definitive value for the band gap, however, the position of the VBM relative to E_F sets a lower limit. If our estimate for the VBM is to be believed, the band gap of CrSBr must be larger than 1.6 ± 0.1 eV. Though within uncertainty with the STS measurements, it would put the value of the band gap at the upper limit of the tunnelling result, and place the chemical potential very close to the conduction band minimum (CBM). Bianchi *et al.*, who reported a VBM of 1.51 eV, also concluded that the band gap must be significantly larger than 1.5 eV due to the strong charging effects observed [63].

Transport measurements have reported a surprisingly small activation energy on the order of 100 meV [52, 54], supporting the idea of a small separation between the chemical potential and CBM. Additionally, Klein *et al.* have reported the exis-
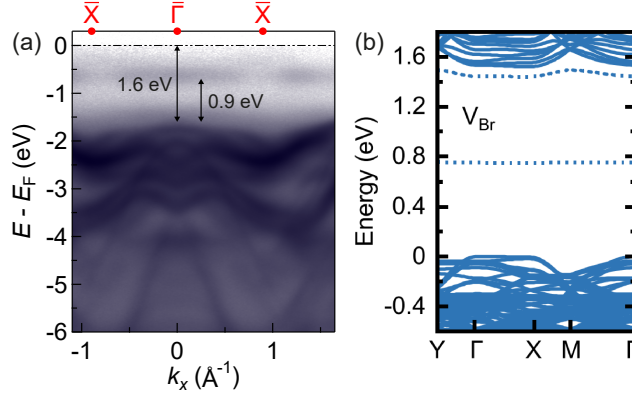
Figure 5.6: a) ARPES spectra of CrSBr along the $\overline{\Gamma} \to \overline{X}$ direction using 90 eV LH polarised light. Intensity is plotted on a logarithmic scale. Sample temperature is 33 K. b) Calculated electronic structure of CrSBr accounting for Br vacancies, taken from ref [221].

tence of optically active defects in CrSBr that result in energy states within the band gap [221]. We see possible evidence for these defect states in the ARPES data as a band of spectral intensity approximately 0.9 eV above the VBM (Fig. 5.6(a)). This is close to the predicted energy state for Br vacancies by Klein *et al.* of ∼0.75 eV (Fig. 5.6(b)), which they report is also the most energetically favourable defect compared to S and Cr vacancies [221]. The existence of these defect states could explain the pinning of the chemical potential close to the CBM, as well as cause complications in the interpretation of optical and STS measurements. With this in mind, we hypothesise that the band gap of CrSBr is somewhere in the range 1.6–2 eV, in agreement with recently reported *GW* calculations [56, 57, 63], though more work is required to determine its precise value.

5.4   Temperature-dependent electronic structure

So far, we have focused entirely on low-temperature ARPES measurements of CrSBr in the antiferromagnetic phase. However, investigating how the electronic structure changes with temperature, particularly when crossing the magnetic transition, can be highly informative and help reveal the magnetic interactions that give rise to the ordered phase [64, 135]. We begin with a systematic study of the temperature-dependence by slowly varying the sample temperature from base temperature to 200 K, while acquiring ARPES spectra. Selected ARPES spectra of CrSBr at different sample temperatures are shown in Fig. 5.7(a), measured using 53 eV LH polarised light. Clear changes can be seen for the bands at $\overline{\Gamma}$ in the energy range
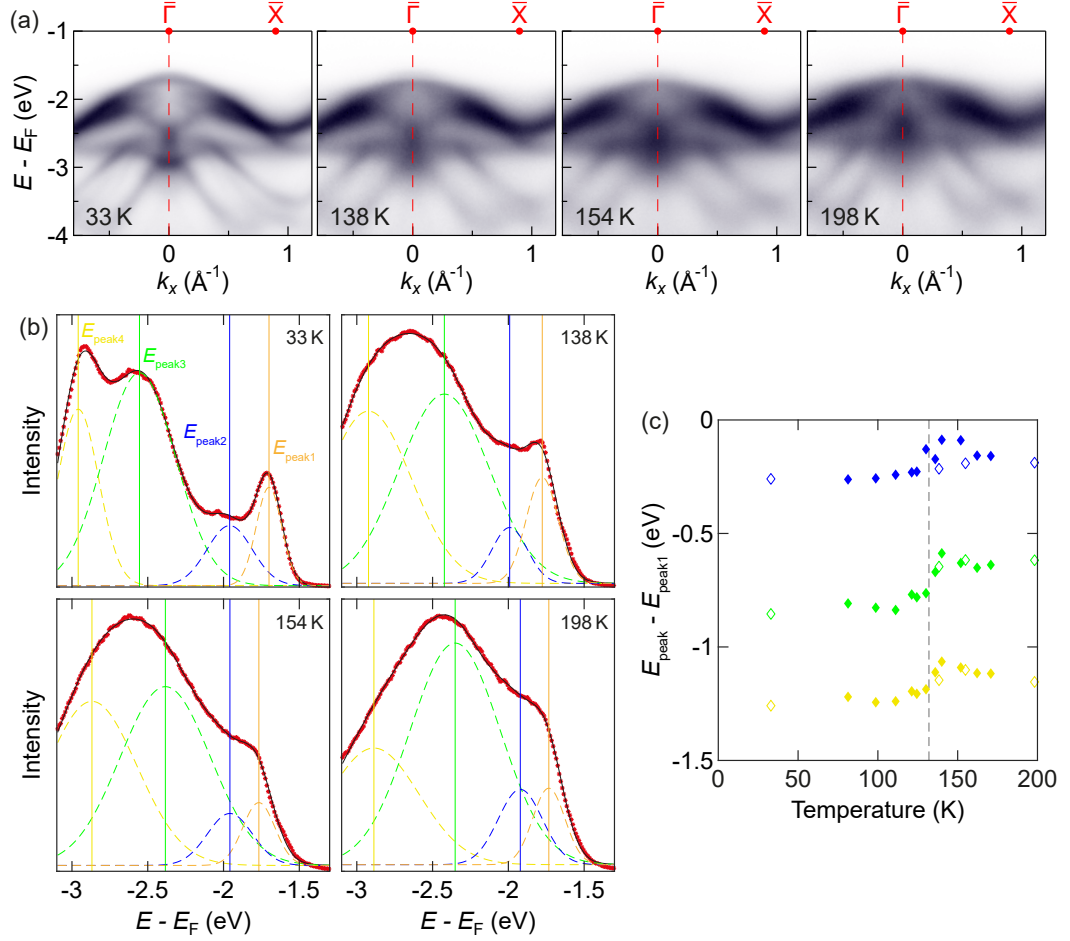
Figure 5.7: a) ARPES spectra of CrSBr along the $\overline{\Gamma} \to \overline{X}$ direction using 53 eV LH polarised light at the specified sample temperatures. b) EDCs from the spectra in (a) at the $\overline{\Gamma}$ point (red dashed lines). EDCs are fit to a function comprised of four Gaussian peaks. c) Gaussian peak positions relative to E_{peak1} extracted from ARPES spectra at different sample temperatures. Unfilled data points correspond to values extracted from the data in (b). The vertical dashed line marks T_N.

-3 eV to -1.7 eV relative to E_F, characterised by a shift of the band energies and an increase in the broadness.

This band shifting can be quantified by fitting to EDCs at $\overline{\Gamma}$, demonstrated in Fig. 5.7(b). The fitting follows the same procedure as that in Fig. 5.2 using a function comprised of four Gaussian peaks. The extracted peak positions relative to peak 1 are plotted in Fig. 5.7(c). The unfilled data points are from the spectra in Fig. 5.7, acquired from the same sample as used in Figs. 5.4 and 5.5, while the filled data points are from a different sample. This other sample suffered from a number of additional valence band shifts due to charging and beam damage effects. Plotting

the relative energy shifts, as opposed to the absolute, eliminates contributions from these effects, allowing the two data sets to be combined.

Looking closer at Fig. 5.7(c), the peak energies stay approximately constant while in the antiferromagnetic phase, but there is a sharp energy shift centred around T_N, particularly for the green and yellow data points. This indicates that changes with temperature originate primarily from the change in magnetic phase, rather than a smooth variation with temperature.

It should be mentioned, however, that a significant amount of uncertainty should be placed on the plotted data points, particularly for those above T_N. At higher temperatures, the EDCs line shapes become notably broader and it becomes difficult to resolve the separate peaks observed at low temperatures. As such, the high temperature fitting shown in Fig. 5.7(b) is not unique and a variety of acceptable fits are possible. This hence places a large amount of uncertainty on the extracted peak positions, which can explain the observed scatter in Fig. 5.7(c). This is particularly true for the blue data points which, even at low temperature, would be expected to have large error bars.

Accordingly, we note that the the extracted band shifts are meant only to illustrate a prominent change in the electronic structure of CrSBr at the onset of antiferromagnetic order, and not as an accurate determination of how much the bands at $\overline{\Gamma}$ shift with temperature. However, we believe accurate and meaningful values for the band shifts could be extracted by careful fitting. This may require more data points that are closely spaced in temperature to enable tracking of each band as they shift in energy, in addition to a more accurate fitting function (e.g., Voigt peaks with a background function), which is beyond the scope of this Thesis. Nonetheless, these results demonstrate a clear change in the electronic structure of CrSBr around T_N.

We explore these changes further in Fig. 5.8 by comparison of ARPES spectra measured below T_N at a base sample temperature of 33 K, and above T_N in the temperature range 150–155 K. Fig. 5.8(a) again shows spectra measured using 53 eV LH polarised light, referenced now with respect to the VBM. The extracted peak positions have been indicated following the colour convention in Fig. 5.7, where the solid lines come from the data in panel (i) and the dashed lines come from panel (ii). In general, heating above T_N causes a reduction in the bandwidth at $\overline{\Gamma}$ for the bands between -1.5 eV to 0 eV measured relative to the VBM. Whether E_{VBM} also shifts to higher binding energy is unclear from these spectra alone, and would require similar measurements along $\overline{\Gamma} \rightarrow \overline{Y}$ to determine.

Fig. 5.8(b) shows the corresponding spectra measured using 90 eV LH po-
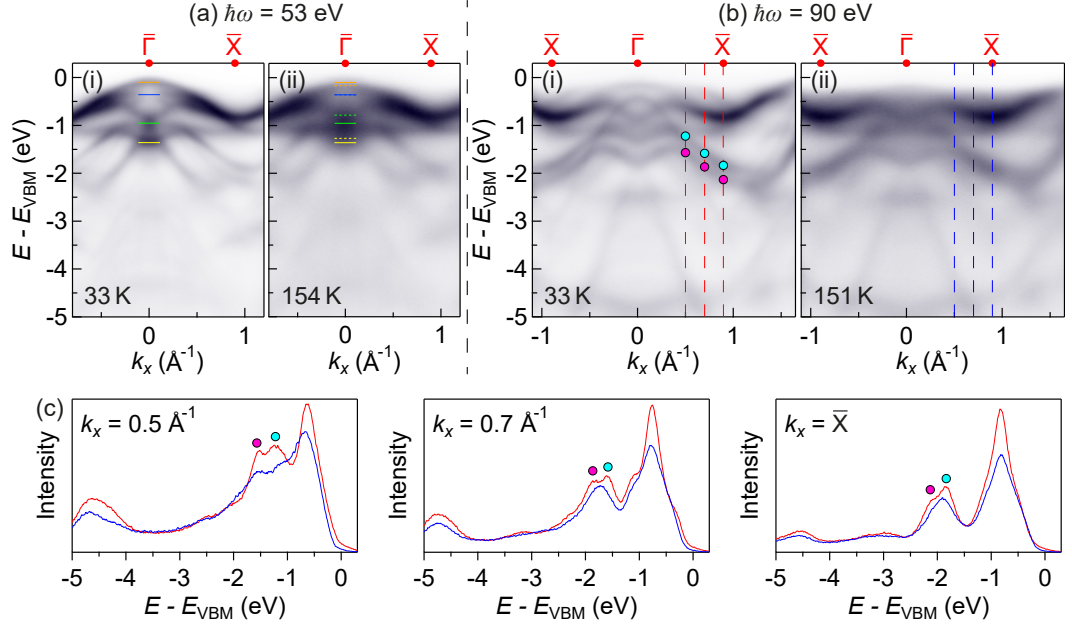
Figure 5.8: a,b) ARPES spectra of CrSBr along the $\overline{\mathbf{\Gamma}} \to \overline{\mathbf{X}}$ direction using (a) 53 eV and (b) 90 eV LH polarised light with a sample temperature (i) below and (ii) above T_N. Coloured lines in (a) mark the positions of Gaussian peaks fit to EDCs at $\overline{\mathbf{\Gamma}}$ following the convention in Fig. 5.7, where solid lines and dashed lines are from EDCs below and above T_N, respectively. c) EDCs from the spectra in (b) at the specified k_x positions (red and blue dashed lines). Round markers indicate the position of two bands present in the ARPES data below T_N.

larised light. Particular attention is focused on the bands at the $\overline{\mathbf{X}}$ point around -2 eV, which appear as a pair below T_N, but merge into a single band above T_N. This is evidenced more clearly in the EDCs (Fig. 5.8(c)). At the $\overline{\mathbf{X}}$ point, the EDC from the 33 K data shows a doublet peak in the intensity at -2 eV, whereas this appears as a single peak in the 151 K data. EDCs closer to $\overline{\mathbf{\Gamma}}$ still show hints of a double peak at 151 K, however, suggesting this effect is focused primarily at the $\overline{\mathbf{X}}$ point. The appearance of two bands below T_N is reminiscent of an exchange-like splitting [222]. Though bulk CrSBr is antiferromagnetic and has zero net magnetisation, each layer has ferromagnetic ordering. For weakly coupled layers, as suggested by the lack of k_z dispersion, one can imagine a case where individual layers experience a local net magnetic field, leading to a lifting of the spin degeneracy. Note, though within a single layer the bands would become spin polarised, the alternating magnetism between layers would lead to the bands remaining spin degenerate, i.e. each band has up and down spin contributions from alternating layers. Also, due to the spin ordering on the Cr atoms, any split bands are likely to possess primarily

Br or S orbital character. Input from theory can help to support this hypothesis, as well as provide further insight to the underlying exchange mechanisms.

A final feature to comment on is the observed increase in spectral broadening above T_{N}. Although some amount of temperature-dependent broadening is normal due to electron-phonon coupling, the increase displayed here is far greater than expected by regular scattering mechanisms. Similar effects have been observed in $CrGeTe_3$ [64], where it was suggested that the increased broadening above T_{C} is related to the magnetic disorder and enhanced spin-phonon coupling [223], which has been shown to also have a strong presence in CrSBr [224]. Additionally, the paramagnetic calculation by Bianchi *et al.* supports this idea of disorder enhanced broadening in CrSBr, as mentioned in Section 1.2.3. On top of this, Bianchi *et al.* also predicted a transition to a more pronounced k_z dispersion in the paramagnetic phase, which could further contribute to an apparent increase in broadening [63].

5.5   Future work

The results presented in this Chapter provide initial insights into the electronic structure of CrSBr and how this is influenced by the in-plane anisotropy and magnetic order. However, a number of ARPES measurements and subsequent analyses are still required to fully appreciate the mechanisms at play in this systems. First and foremost, ARPES spectra along the $\overline{\mathbf{\Gamma}} \to \overline{\mathbf{Y}}$ direction have been less studied so far. Measuring along this other high symmetry direction with different photon energies and polarisations will allow a full ARPES description of CrSBr to be built, as well as further probing the present in-plane orbital anisotropy and matrix element effects. Additionally, this may uncover an optimal measurement geometry for highlighting the VBM, providing a more precise determination of E_{VBM}. Temperature-dependent measurements along $\overline{\mathbf{\Gamma}} \to \overline{\mathbf{Y}}$ should also be repeated to look for further electronic structure differences between the different magnetic phases.

Following on from this, a plot of the electronic structure dispersion can be built by extracting the band positions from the different ARPES spectra. An initial plot of the band dispersions from the low-temperature ARPES data is presented in Fig. 5.9, extracted by Cephise Cacho at Diamond Light Source. Here, the plotted dispersions have been developed by combining extracted values from ARPES spectra of different photon energy and polarisation. For example, Fig. 5.9(a) consists of data points collated from four different spectra, consisting of combinations of the photon energies 53 eV and 90 eV and LH and LV polarisations (Fig. 5.4 panels (i) and (ii)). Overlapping data points from different spectra are merged to give an average
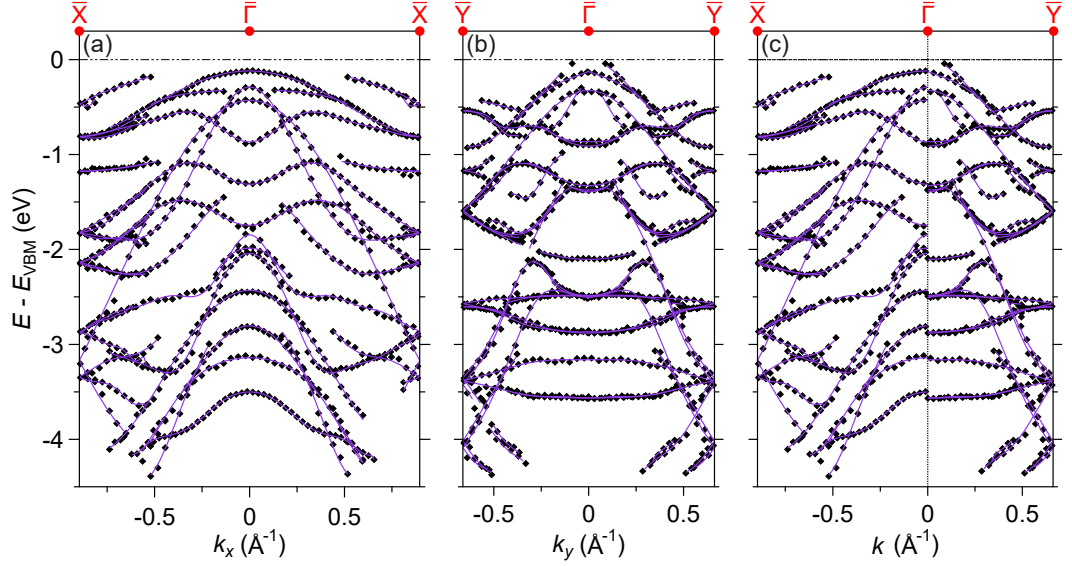
Figure 5.9: a) Extracted band dispersions along the $\overline{\Gamma} \to \overline{X}$ direction from ARPES spectra of CrSBr using 53/90 eV LH/LV polarised light at 33 K. Data points are taken from ARPES spectra, while lines are polynomial fits mimicking the different band dispersions. b) Extracted band dispersions along $\overline{\Gamma} \to \overline{Y}$ from ARPES spectra using 53/90 eV LH polarised light at 33 K. c) Combined band dispersions from (a) and (b) giving an $\overline{X} \to \overline{\Gamma} \to \overline{Y}$ cut through the CrSBr BZ.

value for the band position. Additionally, bands that continue into the 2nd BZ are backfolded, which helps reveal the full dispersion of certain bands whose intensity is either partially or completely suppressed in the 1st BZ. This method results in a highly detailed description of the electronic structure along different high symmetry directions. Note, the $\overline{\Gamma} \to \overline{Y}$ dispersions in Fig. 5.9(b) are only from LH data, meaning a number of bands may be missing that are primarily visible when using LV light. This is the reason some of the $\overline{\Gamma} \to \overline{X}$ bands disappear at $\overline{\Gamma}$ in Fig. 5.9(c), and further supports the need for additional ARPES measurements along $\overline{\Gamma} \to \overline{Y}$.

Due to the large number of bands and variety of changes that happen around T_{N}, comparison with theory is vital to gain a proper understanding. The extracted dispersions can be directly compared with calculations from theory, allowing a better assignment of extracted positions to particular bands, as well as helping to refine the theoretical model itself. In return, the calculations can provide additional information about the different bands such as their orbital character. This can help to explain the observed matrix element effects, as well as revealing the electron orbitals involved with the temperature-dependent electronic structure.

As mentioned previously, a collaboration with theorists is currently in
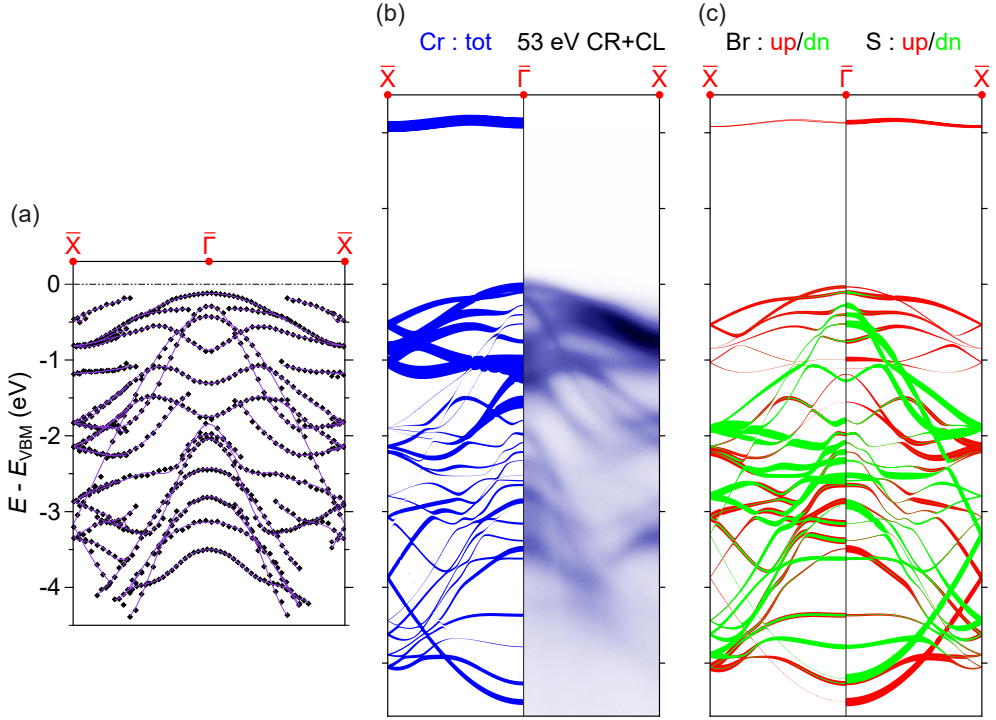
Figure 5.10: a) Extracted band dispersions along the $\overline{\mathbf{\Gamma}} \to \overline{\mathbf{X}}$ direction from ARPES spectra of CrSBr using 53/90 eV LH/LV polarised light at 33 K. b) (left) calculated band structure of CrSBr using a $QSG\hat{W}+BSE$ model, weighted by Cr orbital character, and (right) summation of ARPES spectra of CrSBr measured using circular right and circular left polarised light at 53 eV, plotted along the $\overline{\mathbf{\Gamma}} \to \overline{\mathbf{X}}$ direction. c) Calculated band structure of CrSBr using a $QSG\hat{W}+BSE$ model, weighted by (left) Br and (right) S orbital character, and additionally coloured coded according to spin, plotted along the $\overline{\mathbf{\Gamma}} \to \overline{\mathbf{X}}$ direction. Atomic weights are projected within a single CrSBr layer.

progress to explore these ideas. Fig. 5.10 shows some preliminary calculations of CrSBr in the antiferromagnetic state, performed using a $QSG\hat{W} + BSE$ model by Swagata Acharya and Mark van Shilfgaarde at the National Renewable Energy Laboratory, USA. This is similar to the calculations presented by Bianchi *et al.* [63], but with the inclusion of BSE corrections. First and foremost, the calculations show an excellent agreement with the experimental ARPES data and extracted band positions, able to reproduce almost all visible features. Furthermore, the atomic weights are projected within a single layer of CrSBr (not averaged across the full AFM unit cell) which allows the identification of exchange-split pairs of bands around the X points. This is as previously predicted, and the atomic weights indeed show predominately Br and S character, as hypothesised. It is hoped this

collaboration will be able to further build on the data presented in this Chapter, with the aim of publishing the results in the near future.

5.6   Summary

At the beginning of this Chapter, we presented a method of exfoliating bulk van der Waals flakes on to a clean gold surface, with the aim of minimising charging effects in low-temperature ARPES measurements. This has proven hugely successful when applied to CrSBr, able to measure ARPES spectra at temperatures far below T_N with negligible valence band shifts from charging, confirmed through a systematic variation of the beam intensity. This method of preparing bulk 2D materials for ARPES would be highly applicable to other semiconducting systems, particularly in the family of 2D magnets, that have proven difficult to measure in their bulk form due to charging effects.

ARPES measurements of bulk CrSBr have highlighted pronounced matrix elements effects coming from the strong in-plane anisotropy. Out-of-plane, the layers are weakly coupled, leading to a minimal k_z dispersion. Despite this, the incident photon energy plays an important role in the intensity of certain bands and should be carefully considered, in addition to the polarisation of light and measurement geometry, when looking to highlight particular spectral features. A number of changes with temperature were also observed, occurring at the antiferromagnetic transition temperature, T_N. By comparison to theory, it may be possible to link these changes to specific magnetic interactions within the system.

In the future, it would be desirable to perform ARPES on twisted stacks of 2D magnets. The ribbon-like exfoliation of CrSBr makes it particularly suited to fabricating twisted samples, as the relative orientating of different flakes can be easily known. Inherently, however, fabrication of twisted samples requires transfer of at least one flake onto another. This does not align well with the gold exfoliation method presented here, as the large adhesion between the gold and 2D material prohibits subsequent transfer. Furthermore, transfer of 2D flakes is predominately performed using polymer stamps (Section 2.3.1) which can leave residue on the sample surface, requiring annealing to high temperatures that will degrade many 2D magnetic materials. Instead, new fabrication methods of 2D homo- and heterostructures are being developed to overcome these issues, which we will discuss in the next Chapter.

Chapter 6

Conclusions

In this thesis, we have used µARPES to measure the electronic structure of twisted graphenes and 2D semiconducting magnets. The high quality of data acquired allowed a direct comparison of measured spectral features to theoretical predictions, providing insight into the interlayer interactions present in these materials.

In Chapter 3, we presented a comparison between few-layer aligned and twisted graphene, demonstrating the changes in electronic structure that are introduced at a twisted interface. Beginning with aligned graphene, particular attention was given to monolayer and bilayer graphene in terms of the appearance of their ARPES spectra and how this can be analysed through band fitting. Importantly, this revealed that band renormalisations due to many-body interactions were minimal in our graphene samples, meaning their electronic structure could be accurately predicted using a tight-binding or HkpTB model, validating their later use in modelling twisted graphene

For twisted graphene, we considered the three stacking arrangements tBG, tMBG and tDBG. Their ARPES spectra exhibited characteristic features of twisted systems, such as hybridisation gaps due to interlayer interactions and replica bands from the moiré potential. Additionally, the degree with which these features were present was shown to be dependent on the twist angle. At large twist angles, the electronic structure primarily resembles that of the individual graphene layers, with only weak replica band intensities and hybridisation gaps at high binding energies. At small twist angles, the electronic structure becomes highly modified due to the large number of interacting bands occupying a small region in reciprocal space, eventually forming a flat band at E_F. Direct comparison of these results to the HkpTB model was enabled through simulation of the ARPES spectra, which gave qualitative agreement to the experimental data.

Before moving on, we also discussed the validity of our twisted graphene results and reported twist angle values. A method of determining the twist angle directly from the ARPES spectra was presented, which used alignment of the mBZ with the primary and replica band intensities at E_F. Twist angles determined from this method were compared to those calculated from LEED patterns taken from the same samples. The agreement between the two methods provided confidence in our quoted values, while also highlighting the disordered nature of twisted samples and the many different twist angle domains that can arise. A simple qualitative analysis of the measured SPEM images was used to confirm the uniformity of particular sample regions from which ARPES spectra were acquired.

In Chapter 4, we performed a thorough quantitative test of predictions from the HkpTB model against key band parameters and spectral features in the ARPES data of twisted graphene as a function of twist angle, number of layers and applied gate voltage. Replica band intensities and hybridisation gap sizes, δ, were chosen as quantifiable parameters that could be directly compared to calculations from the HkpTB model, demonstrating excellent agreement across all measured systems. As part of this, a simple model was proposed to explain the observed replica band intensity hierarchy, providing further insight into the nature of the moiré interaction. In tMBG specifically, the gate-dependence of the electronic structure was explored and compared to theoretical predictions through a self-consistent method, achieving quantitative agreement without fitting to the data. This demonstrated simultaneous charge injection and displacement fields across the graphene layers, resulting in both band shifts and the opening of an energy gap at the bilayer Dirac point.

Despite the good agreement between the HkpTB model and measured ARPES spectra for large and intermediate twist angles, a discrepancy was observed in 1.5° tDBG through characterisation of a flat band. Though the flat band width, E_w, agreed with predictions from the HkpTB model, the energy gap between the flat band minimum and the next valence band states was much larger in the experimental data. Comparing to predictions from Haddadi *et al.* suggested this was due to lattice relaxation effects that become important at small twist angles [201].

In Chapter 5, we measured the electronic structure of bulk CrSBr in different magnetic phases. This was enabled through exfoliation onto a fresh template-stripped gold surface that effectively grounded the CrSBr flake, minimising charging effects at low temperatures. In the antiferromagnetic phase, CrSBr displays a rich electronic valence band structure of primarily 2D character, while also exhibiting pronounced matrix element effects due to a strong in-plane anisotropy. The VBM was estimated to be 1.6 eV below E_F, suggesting a larger band gap than previously

reported by tunnelling and optical measurements. The presence of in-gap states due to Br vacancies may explain this discrepancy. On heating above T_N, a number of band shifts at $\overline{\mathbf{\Gamma}}$, as well as the collapse of split bands at $\overline{\mathbf{X}}$, were observed, occurring at the loss of long-range out-of-plane magnetic order. A collaboration with theorists is ongoing to link these changes to specific magnetic interactions within the crystal.

Overall, these results push forward our understanding of the interlayer and correlated interactions present in 2D materials and structures. Acquiring high resolution μARPES data has allowed for a thorough comparison with theoretical predictions, enabling refinement of the current models and appreciation of when they are valid. In return, this provides insight into the observed phenomena and interactions present in these systems and how they may be manipulated for future purposes and the design of next generation quantum devices.

Moving forward, a number of open questions still remain. We have already mentioned the query of how the magnetic order affects the electronic structure in CrSBr, which we are hoping to address in the future. This requires input from theory, which, conversely, benefits from experimental input. Further ARPES studies of CrSBr and other 2D magnets in general can aid in our theoretical understanding of these materials and how best to model the different magnetic phases. Application of the gold exfoliation method presented in this thesis may help in this regard, offering a simple method of preparing semiconducting 2D crystals for ARPES.

For twisted graphenes, detailed measurements of the flat band dispersion as a function of twist angle, number of layers and applied back gate voltage are still lacking [225]. As discussed at the end of Chapter 4, this is primarily due to limitations in the resolution offered by current instrumentation and sample fabrication methods. Returning to the latter at the end of this Chapter, an initial step could be to fabricate capillary mirror optics with spatial resolution comparable to that of zone plates. This would allow higher energy resolution studies from smaller uniform regions. Additionally, further improvements in energy resolution would also be desirable, aiming to match that offered by conventional ARPES which can achieve a resolution of only a few meV. Advancements in beamline design and technology may facilitate these improvements.

Expanding beyond the twisted structures presented in this thesis, twisted graphene systems with multiple twisted interfaces are beginning to grow in popularity. In the simplest case, these consist of stacks of single graphene layers with alternating twist angles, such that odd (even) layers are aligned. Interestingly, these alternating twisted graphene structures exhibit superconductivity similar to that in magic-angle tBG, which appears to be a universal trait of magic-angle stacks of

single graphene layers [107, 226, 227]. In the more general case, twisted trilayer graphene with different twist angles at the two interfaces has also been explored. Combining of the two differing moiré patterns produces a quasicrystal potential that highly modifies the low-energy electronic structure [228]. Attempts may be made in the near future to visualise these effects using ARPES.

Another interesting twistronic phenomenon recently revealed from µARPES is moiré proximity effects. In heterostructures of graphene on 2° twisted WS_2/WSe_2, replicas of the graphene Dirac cone were observed surrounding the primary Dirac cone, with a separation equal to that of the moiré reciprocal lattice vector of the underlying twisted TMD heterobilayer [229]. Here, the electronic structure of the graphene is modulated by the underlying moiré potential, demonstrating a route to engineer a material through proximity to a moiré superlattice. Similar effects would be expected for other 2D materials placed on twisted structures, which could also be studied using µARPES.

Finally, to return to the comment on fabrication methods, the polymer-based transfer techniques widely used for the fabrication of 2D homo- and heterostructures have many drawbacks and limitations. Their use of polymers naturally results in residues left on and between the surfaces of 2D layers, and they can only be used in ambient pressure environments which are prone to contamination from hydrocarbons. To produce samples of higher quality, an alternative transfer method compatible with low pressure environments must be developed. Recently, researchers at the National Graphene Institute have realised a fully inorganic UHV compatible transfer method [230]. 2D materials are exfoliated *in situ* onto adhesive metal alloys, similar to exfoliation on gold. Likewise, coating of these alloys on transparent SiN cantilevers allows for the temperature-controlled pickup and drop-down of exfoliated flakes, all situated within a UHV environment. In this way, pristine 2D structures can be fabricated with almost no contamination, providing the highest possible sample quality to date. The UHV environment also makes the technique highly compatible with air sensitive materials such as the 2D magnets, offering a route to integrate these materials into heterostructures. Once fabricated, samples can be transferred using vacuum suitcases to other UHV systems, maintaining their cleanliness and eliminating the need to anneal samples to remove adsorbates. This advancement in fabrication opens up a number of opportunities for µARPES to study 2D materials and devices previously thought impossible, which will undoubtedly further progress our understanding of these systems.

Bibliography

1. Novoselov, K. S. *et al.* Electric field effect in atomically thin carbon films. *Science* **306,** 666–669. doi:`10.1126/science.1102896` (2004).

2. Geim, A. K. & Novoselov, K. S. The rise of graphene. *Nature Materials* **6,** 183–191. doi:`10.1038/nmat1849` (2007).

3. Choi, W. *et al.* Recent development of two-dimensional transition metal dichalcogenides and their applications. *Materials Today* **20,** 116–130. doi:`10.1016/j.mattod.2016.10.002` (2017).

4. Miró, P., Audiffred, M. & Heine, T. An atlas of two-dimensional materials. *Chemical Society Reviews* **43,** 6537–6554. doi:`10.1039/C4CS00102H` (2014).

5. Ajayan, P., Kim, P. & Banerjee, K. Two-dimensional van der Waals materials. *Physics Today* **69,** 38–44. doi:`10.1016/j.mattod.2016.10.002` (2016).

6. Lin, Z. *et al.* 2D materials advances: from large scale synthesis and controlled heterostructures to improved characterization techniques, defects and applications. *2D Materials* **3,** 042001. doi:`10.1088/2053-1583/3/4/042001` (2016).

7. Geim, A. K. & Grigorieva, I. V. Van der Waals heterostructures. *Nature* **499,** 419–425. doi:`10.1038/nature12385` (2013).

8. Novoselov, K. S., Mishchenko, A., Carvalho, A. & Castro Neto, A. H. 2D materials and van der Waals heterostructures. *Science* **353,** aac9439. doi:`10.1126/science.aac9439` (2016).

9. Cao, Y. *et al.* Correlated insulator behaviour at half-filling in magic-angle graphene superlattices. *Nature* **556,** 80–84. doi:`10.1038/nature26154` (2018).

10. Cao, Y. *et al.* Unconventional superconductivity in magic-angle graphene superlattices. *Nature* **556,** 43–50. doi:`10.1038/nature26160` (2018).

11. Hennighausen, Z. & Kar, S. Twistronics: a turning point in 2D quantum materials. *Electronic Structure* **3,** 014004. doi:`10.1088/2516-1075/abd957` (2021).

12. Gibertini, M., Koperski, M., Morpurgo, A. F. & Novoselov, K. S. Magnetic 2D materials and heterostructures. *Nature Nanotechnology* **14,** 408–419. doi:`10.1038/s41565-019-0438-6` (2019).

13. Zhang, W., Wong, P. K. J., Zhu, R. & Wee, A. T. S. Van der Waals magnets: wonder building blocks for two-dimensional spintronics? *InfoMat* **1,** 479–495. doi:`10.1002/inf2.12048` (2019).

14. Warner, J. H., Schaffel, F., Rummeli, M. & Bachmatiuk, A. *Graphene: Fundamentals and emergent applications* doi:`10.1016/C2011-0-05169-4` (Elsevier, 2013).

15. Partoens, B. & Peeters, F. M. From graphene to graphite: Electronic structure around the K point. *Physical Review B* **74,** 075404. doi:`10.1103/PhysRevB.74.075404` (2006).

16. Mazzola, F. *et al.* Kinks in the σ band of graphene induced by electron-phonon coupling. *Physical Review Letters* **111,** 216806. doi:`10.1103/PhysRevLett.111.216806` (2013).

17. McCann, E. & Koshino, M. The electronic properties of bilayer graphene. *Reports on Progress in Physics* **76,** 056503. doi:`10.1088/0034-4885/76/5/056503` (2013).

18. Castro Neto, A. H., Guinea, F., Peres, N. M. R., Novoselov, K. S. & Geim, A. K. The electronic properties of graphene. *Reviews of Modern Physics* **81,** 109–162. doi:`10.1103/RevModPhys.81.109` (2009).

19. Katsnelson, M. I. Graphene: carbon in two dimensions. *Materials Today* **10,** 20–27. doi:`10.1016/S1369-7021(06)71788-6` (2007).

20. Novoselov, K. S. *et al.* Two-dimensional gas of massless Dirac fermions in graphene. *Nature* **438,** 197–200. doi:`10.1038/nature04233` (2005).

21. Slonczewski, J. C. & Weiss, P. R. Band structure of graphite. *Physical Review* **109,** 272–279. doi:`10.1103/PhysRev.109.272` (1958).

22. McClure, J. W. Band structure of graphite and de Haas-van Alphen effect. *Physical Review* **108,** 612–618. doi:`10.1103/PhysRev.108.612` (1957).

23. McClure, J. W. Theory of diamagnetism of graphite. *Physical Review* **119,** 606–613. doi:`10.1103/PhysRev.119.606` (1960).

24. Taychatanapat, T., Watanabe, K., Taniguchi, T. & Jarillo-Herrero, P. Quantum Hall effect and Landau-level crossing of Dirac fermions in trilayer graphene. *Nature Physics* **7,** 621–625. doi:`10.1038/nphys2008` (2011).

25. Pykal, M., Jurečka, P., Karlickỳ, F. & Otyepka, M. Modelling of graphene functionalization. *Physical Chemistry Chemical Physics* **18,** 6351–6372. doi:`10.1039/C5CP03599F` (2016).

26. Mucha-Kruczyński, M. *et al.* Characterization of graphene through anisotropy of constant-energy maps in angle-resolved photoemission. *Physical Review B* **77,** 195403. doi:`10.1103/PhysRevB.77.195403` (2008).

27. Ohta, T., Bostwick, A., Seyller, T., Horn, K. & Rotenberg, E. Controlling the electronic structure of bilayer graphene. *Science* **313,** 951–954. doi:`10.1126/science.1130681` (2006).

28. Zhang, Y. *et al.* Direct observation of a widely tunable bandgap in bilayer graphene. *Nature* **459,** 820–823. doi:`10.1038/nature08105` (2009).

29. Gu, Y., Zheng, M., Liu, Y. & Xu, Z. Low-temperature synthesis and growth of hexagonal boron-nitride in a lithium bromide melt. *Journal of the American Ceramic Society* **90,** 1589–1591. doi:`10.1111/j.1551-2916.2007.01551.x` (2007).

30. Watanabe, K., Taniguchi, T. & Kanda, H. Direct-bandgap properties and evidence for ultraviolet lasing of hexagonal boron nitride single crystal. *Nature Materials* **3,** 404–409. doi:`10.1038/nmat1134` (2004).

31. Cassabois, G., Valvin, P. & Gil, B. Hexagonal boron nitride is an indirect bandgap semiconductor. *Nature Photonics* **10,** 262–266. doi:`10.1038/nphoton.2015.277` (2016).

32. Elias, C. *et al.* Direct band-gap crossover in epitaxial monolayer boron nitride. *Nature Communications* **10,** 2639. doi:`10.1038/s41467-019-10610-5` (2019).

33. Wickramaratne, D., Weston, L. & Van de Walle, C. G. Monolayer to bulk properties of hexagonal boron nitride. *The Journal of Physical Chemistry C* **122,** 25524–25529. doi:`10.1021/acs.jpcc.8b09087` (2018).

34. Dean, C. R. *et al.* Boron nitride substrates for high-quality graphene electronics. *Nature Nanotechnology* **5,** 722–726. doi:`10.1038/nnano.2010.172` (2010).

35. Jang, S. K., Youn, J., Song, Y. J. & Lee, S. Synthesis and characterization of hexagonal boron nitride as a gate dielectric. *Scientific Reports* **6,** 30449. doi:`10.1038/srep30449` (2016).

36. Kretinin, A. V. *et al.* Electronic properties of graphene encapsulated with different two-dimensional atomic crystals. *Nano Letters* **14,** 3270–3276. doi:`10.1021/nl5006542` (2014).

37. Burch, K. S., Mandrus, D. & Park, J.-G. Magnetism in two-dimensional van der Waals materials. *Nature* **563,** 47–52. doi:`10.1038/s41586-018-0631-z` (2018).

38. Yang, S., Zhang, T. & Jiang, C. van der Waals magnets: Material family, detection and modulation of magnetism, and perspective in spintronics. *Advanced Science* **8,** 2002488. doi:`10.1002/advs.202002488` (2021).

39. Mermin, N. D. & Wagner, H. Absence of ferromagnetism or antiferromagnetism in one-or two-dimensional isotropic Heisenberg models. *Physical Review Letters* **17,** 1133–1136. doi:`10.1103/PhysRevLett.17.1133` (1966).

40. Gong, C. *et al.* Discovery of intrinsic ferromagnetism in two-dimensional van der Waals crystals. *Nature* **546,** 265–269. doi:`10.1038/nature22060` (2017).

41. Huang, B. *et al.* Layer-dependent ferromagnetism in a van der Waals crystal down to the monolayer limit. *Nature* **546,** 270–273. doi:`10.1038/nature22391` (2017).

42. Zhang, Z. *et al.* Direct photoluminescence probing of ferromagnetism in monolayer two-dimensional CrBr3. *Nano Letters* **19,** 3138–3142. doi:`10.1021/acs.nanolett.9b00553` (2019).

43. Fei, Z. *et al.* Two-dimensional itinerant ferromagnetism in atomically thin Fe3GeTe2. *Nature Materials* **17,** 778–782. doi:`10.1038/s41563-018-0149-7` (2018).

44. Lee, J.-U. *et al.* Ising-type magnetic ordering in atomically thin FePS3. *Nano Letters* **16,** 7433–7438. doi:`10.1021/acs.nanolett.6b03052` (2016).

45. Lee, K. *et al.* Magnetic order and symmetry in the 2D semiconductor CrSBr. *Nano Letters* **21,** 3511–3517. doi:`10.1021/acs.nanolett.1c00219` (2021).

46. Jiang, S., Shan, J. & Mak, K. F. Electric-field switching of two-dimensional van der Waals magnets. *Nature Materials* **17,** 406–410. doi:`10.1038/s41563-018-0040-6` (2018).

47. Jiang, S., Li, L., Wang, Z., Mak, K. F. & Shan, J. Controlling magnetism in 2D CrI3 by electrostatic doping. *Nature Nanotechnology* **13,** 549–553. doi:`10.1038/s41565-018-0135-x` (2018).

48. Deng, Y. *et al.* Gate-tunable room-temperature ferromagnetism in two-dimensional Fe3GeTe2. *Nature* **563,** 94–99. doi:`10.1038/s41586-018-0626-9` (2018).

49. Liu, Y. *et al.* The environmental stability characterization of exfoliated few-layer CrXTe3 (X= Si, Ge) nanosheets. *Applied Surface Science* **511,** 145452. doi:`10.1016/j.apsusc.2020.145452` (2020).

50. Shcherbakov, D. *et al.* Raman spectroscopy, photocatalytic degradation, and stabilization of atomically thin chromium tri-iodide. *Nano Letters* **18,** 4214–4219. doi:`10.1021/acs.nanolett.8b01131` (2018).

51. Torres, K. *et al.* Probing Defects and Spin-Phonon Coupling in CrSBr via Resonant Raman Scattering. *Advanced Functional Materials* **33,** 2211366. doi:`10.1002/adfm.202211366` (2023).

52. Wu, F. *et al.* Quasi-1D Electronic Transport in a 2D Magnetic Semiconductor. *Advanced Materials* **34,** 2109759. doi:`10.1002/adma.202109759` (2022).

53. Klein, J. *et al.* The bulk van der Waals layered magnet CrSBr is a quasi-1D material. *ACS Nano* **17,** 5316–5328. doi:`10.1021/acsnano.2c07316` (2023).

54. Telford, E. J. *et al.* Layered antiferromagnetism induces large negative magnetoresistance in the van der Waals semiconductor CrSBr. *Advanced Materials* **32,** 2003240. doi:`10.1002/adma.202003240` (2020).

55. Telford, E. J. *et al.* Coupling between magnetic order and charge transport in a two-dimensional magnetic semiconductor. *Nature Materials* **21,** 754–760. doi:`10.1038/s41563-022-01245-x` (2022).

56. Wilson, N. P. *et al.* Interlayer electronic coupling on demand in a 2D magnetic semiconductor. *Nature Materials* **20,** 1657–1662. doi:`10.1038/s41563-021-01070-8` (2021).

57. Linhart, W. *et al.* Optical markers of magnetic phase transition in CrSBr. *Journal of Materials Chemistry C* **11,** 8423–8430. doi:`10.1039/D3TC01216F` (2023).

58. Bae, Y. J. *et al.* Exciton-coupled coherent magnons in a 2D semiconductor. *Nature* **609,** 282–286. doi:`10.1038/s41586-022-05024-1` (2022).

59. Wang, H., Qi, J. & Qian, X. Electrically tunable high Curie temperature two-dimensional ferromagnetism in van der Waals layered crystals. *Applied Physics Letters* **117,** 083102. doi:`10.1063/5.0014865` (2020).

60. Yang, K., Wang, G., Liu, L., Lu, D. & Wu, H. Triaxial magnetic anisotropy in the two-dimensional ferromagnetic semiconductor CrSBr. *Physical Review B* **104,** 144416. doi:`10.1103/PhysRevB.104.144416` (2021).

61. López-Paz, S. A. *et al.* Dynamic magnetic crossover at the origin of the hidden-order in van der Waals antiferromagnet CrSBr. *Nature Communications* **13,** 4745. doi:`10.1038/s41467-022-32290-4` (2022).

62. Liu, W. *et al.* A three-stage magnetic phase transition revealed in ultrahigh-quality van der Waals bulk magnet CrSBr. *ACS Nano* **16,** 15917–15926. doi:`10.1021/acsnano.2c02896` (2022).

63. Bianchi, M. *et al.* Paramagnetic electronic structure of CrSBr: Comparison between ab initio G W theory and angle-resolved photoemission spectroscopy. *Physical Review B* **107,** 235107. doi:`10.1103/PhysRevB.107.235107` (2023).

64. Watson, M. D. *et al.* Direct observation of the energy gain underpinning ferromagnetic superexchange in the electronic structure of CrGeTe3. *Physical Review B* **101,** 205125. doi:`10.1103/PhysRevB.101.205125` (2020).

65. Li, M.-Y., Chen, C.-H., Shi, Y. & Li, L.-J. Heterostructures based on two-dimensional layered materials and their potential applications. *Materials Today* **19,** 322–335. doi:`10.1016/j.mattod.2015.11.003` (2016).

66. Rivera, P. *et al.* Observation of long-lived interlayer excitons in monolayer MoSe2–WSe2 heterostructures. *Nature Communications* **6,** 6242. doi:`10.1038/ncomms7242` (2015).

67. Yankowitz, M. *et al.* Emergence of superlattice Dirac points in graphene on hexagonal boron nitride. *Nature Physics* **8,** 382–386. doi:`10.1038/nphys2272` (2012).

68. Frisenda, R. *et al.* Recent progress in the assembly of nanodevices and van der Waals heterostructures by deterministic placement of 2D materials. *Chemical Society Reviews* **47,** 53–68. doi:`10.1039/C7CS00556C` (2018).

69. Zomer, P., Guimarães, M., Brant, J. C., Tombros, N. & Van Wees, B. J. Fast pick up technique for high quality heterostructures of bilayer graphene and hexagonal boron nitride. *Applied Physics Letters* **105,** 013101. doi:`10.1063/1.4886096` (2014).

70. Haigh, S. J. *et al.* Cross-sectional imaging of individual layers and buried interfaces of graphene-based heterostructures and superlattices. *Nature Materials* **11,** 764–767. doi:`10.1038/nmat3386` (2012).

71. Uwanno, T., Hattori, Y., Taniguchi, T., Watanabe, K. & Nagashio, K. Fully dry PMMA transfer of graphene on h-BN using a heating/cooling system. *2D Materials* **2,** 041002. doi:`10.1088/2053-1583/2/4/041002` (2015).

72. Rosenberger, M. R. *et al.* Nano-"squeegee" for the creation of clean 2D material interfaces. *ACS applied materials & interfaces* **10,** 10379–10387. doi:`10.1021/acsami.8b01224` (2018).

73. Cai, Z., Liu, B., Zou, X. & Cheng, H.-M. Chemical vapor deposition growth and applications of two-dimensional materials and their heterostructures. *Chemical Reviews* **118,** 6091–6133. doi:`10.1021/acs.chemrev.7b00536` (2018).

74. Lin, Y.-C. *et al.* Atomically thin heterostructures based on single-layer tungsten diselenide and graphene. *Nano Letters* **14,** 6936–6941. doi:`10.1021/nl503144a` (2014).

75. Jiao, L. *et al.* Molecular-beam epitaxy of monolayer MoSe2: growth characteristics and domain boundary formation. *New Journal of Physics* **17,** 053023. doi:`10.1088/1367-2630/17/5/053023` (2015).

76. Nakano, M., Wang, Y., Kashiwabara, Y., Matsuoka, H. & Iwasa, Y. Layer-by-layer epitaxial growth of scalable WSe2 on sapphire by molecular beam epitaxy. *Nano Letters* **17,** 5595–5599. doi:`10.1021/acs.nanolett.7b02420` (2017).

77. Zhang, Y. *et al.* Recent progress in CVD growth of 2D transition metal dichalcogenides and related heterostructures. *Advanced Materials* **31,** 1901694. doi:`10.1002/adma.201901694` (2019).

78. Fan, Y. *et al.* Recent Advances in Growth of Large-Sized 2D Single Crystals on Cu Substrates. *Advanced Materials* **33,** 2003956. doi:`10.1002/adma.202003956` (2021).

79. Yang, T. *et al.* Van der Waals epitaxial growth and optoelectronics of large-scale WSe2/SnS2 vertical bilayer p–n junctions. *Nature Communications* **8,** 1906. doi:`10.1038/s41467-017-02093-z` (2017).

80. Zhang, K. *et al.* Visualizing van der Waals epitaxial growth of 2D heterostructures. *Advanced Materials* **33,** 2105079. doi:`10.1002/adma.202105079` (2021).

81. Liu, Y. *et al.* Toward barrier free contact to molybdenum disulfide using graphene electrodes. *Nano Letters* **15,** 3030–3034. doi:`10.1021/nl504957p` (2015).

82. Cao, Y. *et al.* Quality heterostructures from two-dimensional crystals unstable in air by their assembly in inert atmosphere. *Nano Letters* **15,** 4914–4921. doi:`10.1021/acs.nanolett.5b00648` (2015).

83. Wang, L. *et al.* One-dimensional electrical contact to a two-dimensional material. *Science* **342,** 614–617. doi:`10.1126/science.1244358` (2013).

84. Lee, C.-H. *et al.* Atomically thin p–n junctions with van der Waals heterointerfaces. *Nature Nanotechnology* **9,** 676–681. doi:`10.1038/nnano.2014.150` (2014).

85. Withers, F. *et al.* Light-emitting diodes by band-structure engineering in van der Waals heterostructures. *Nature Materials* **14,** 301–306. doi:`10.1038/nmat4205` (2015).

86. Roy, T. *et al.* Field-effect transistors built from all two-dimensional material components. *ACS Nano* **8,** 6259–6264. doi:`10.1021/nn501723y` (2014).

87. Song, T. *et al.* Giant tunneling magnetoresistance in spin-filter van der Waals heterostructures. *Science* **360,** 1214–1218. doi:`10.1126/science.aar4851` (2018).

88. Wang, Z. *et al.* Tunneling spin valves based on Fe3GeTe2/hBN/Fe3GeTe2 van der Waals heterostructures. *Nano Letters* **18,** 4303–4308. doi:`10.1021/acs.nanolett.8b01278` (2018).

89. Zhong, D. *et al.* Van der Waals engineering of ferromagnetic semiconductor heterostructures for spin and valleytronics. *Science Advances* **3,** e1603113. doi:`10.1126/sciadv.1603113` (2017).

90. Mogi, M. *et al.* Large anomalous Hall effect in topological insulators with proximitized ferromagnetic insulators. *Physical Review Letters* **123,** 016804. doi:`10.1103/PhysRevLett.123.016804` (2019).

91. Mishchenko, A. *et al.* Twist-controlled resonant tunnelling in graphene/boron nitride/graphene heterostructures. *Nature Nanotechnology* **9,** 808–813. doi:`10.1038/nnano.2014.187` (2014).

92. Luo, D. *et al.* Twist-angle-dependent ultrafast charge transfer in MoS2-graphene van der Waals heterostructures. *Nano Letters* **21,** 8051–8057. doi:`10.1021/acs.nanolett.1c02356` (2021).

93. Choi, J. *et al.* Twist angle-dependent interlayer exciton lifetimes in van der Waals heterostructures. *Physical Review Letters* **126,** 047401. doi:`103/PhysRevLett.126.047401` (2021).

94. Choi, Y. *et al.* Electronic correlations in twisted bilayer graphene near the magic angle. *Nature Physics* **15,** 1174–1180. doi:`10.1038/s41567-019-0606-5` (2019).

95. McGilly, L. J. *et al.* Visualization of moiré superlattices. *Nature Nanotechnology* **15,** 580–584. doi:`10.1038/s41565-020-0708-3` (2020).

96. Gargiulo, F. & Yazyev, O. V. Structural and electronic transformation in low-angle twisted bilayer graphene. *2D Materials* **5,** 015019. doi:`10.1088/2053-1583/aa9640` (2017).

97. Yoo, H. *et al.* Atomic and electronic reconstruction at the van der Waals interface in twisted bilayer graphene. *Nature Materials* **18,** 448–453. doi:`10.1038/s41563-019-0346-z` (2019).

98. Ponomarenko, L. A. *et al.* Cloning of Dirac fermions in graphene superlattices. *Nature* **497,** 594–597. doi:`10.1038/nature12187` (2013).

99. Li, G. *et al.* Observation of Van Hove singularities in twisted graphene layers. *Nature Physics* **6,** 109–113. doi:`10.1038/nphys1463` (2010).

100. Bistritzer, R. & MacDonald, A. H. Moiré bands in twisted double-layer graphene. *Proceedings of the National Academy of Sciences* **108,** 12233–12237. doi:`10.1073/pnas.1108174108` (2011).

101. Chen, S. *et al.* Electrically tunable correlated and topological states in twisted monolayer–bilayer graphene. *Nature Physics* **17,** 374–380. doi:`10.1038/s41567-020-01062-6` (2021).

102. Xu, S. *et al.* Tunable van Hove singularities and correlated states in twisted monolayer–bilayer graphene. *Nature Physics* **17,** 619–626. doi:`10.1038/s41567-021-01172-9` (2021).

103. Cao, Y. *et al.* Tunable correlated states and spin-polarized phases in twisted bilayer–bilayer graphene. *Nature* **583,** 215–220. doi:`10.1038/s41586-020-2260-6` (2020).

104. Shen, C. *et al.* Correlated states in twisted double bilayer graphene. *Nature Physics* **16,** 520–525. doi:`10.1038/s41567-020-0825-9` (2020).

105. Liu, X. *et al.* Spectroscopy of a tunable moiré system with a correlated and topological flat band. *Nature Communications* **12,** 2732. doi:`10.1038/s41467-021-23031-0` (2021).

106. Zhang, C. *et al.* Visualizing delocalized correlated electronic states in twisted double bilayer graphene. *Nature Communications* **12,** 2516. doi:`10.1038/s41467-021-22711-1` (2021).

107. Park, J. M., Cao, Y., Watanabe, K., Taniguchi, T. & Jarillo-Herrero, P. Tunable strongly coupled superconductivity in magic-angle twisted trilayer graphene. *Nature* **590,** 249–255. doi:`10.1038/s41586-021-03192-0` (2021).

108. Zhang, Z. *et al.* Flat bands in twisted bilayer transition metal dichalcogenides. *Nature Physics* **16,** 1093–1096. doi:`10.1038/s41567-020-0958-x` (2020).

109. Seyler, K. L. *et al.* Signatures of moiré-trapped valley excitons in MoSe2/WSe2 heterobilayers. *Nature* **567,** 66–70. doi:`10.1038/s41586-019-0957-1` (2019).

110. Song, T. *et al.* Direct visualization of magnetic domains and moiré magnetism in twisted 2D magnets. *Science* **374,** 1140–1144. doi:`10.1126/science.abj7478` (2021).

111. Bostwick, A., Ohta, T., Seyller, T., Horn, K. & Rotenberg, E. Quasiparticle dynamics in graphene. *Nature Physics* **3,** 36–40. doi:`10.1038/nphys477` (2007).

112. Ohta, T. *et al.* Interlayer interaction and electronic screening in multilayer graphene investigated with angle-resolved photoemission spectroscopy. *Physical Review Letters* **98,** 206802. doi:`10.1103/PhysRevLett.98.206802` (2007).

113. Bostwick, A. *et al.* Renormalization of graphene bands by many-body interactions. *Solid State Communications* **143,** 63–71. doi:`10.1016/j.ssc.2007.04.034` (2007).

114. Siegel, D. A. *et al.* Many-body interactions in quasi-freestanding graphene. *Proceedings of the National Academy of Sciences* **108,** 11365–11369. doi:`10.1073/pnas.1100242108` (2011).

115. Yuan, H. *et al.* Evolution of the valley position in bulk transition-metal chalcogenides and their monolayer limit. *Nano Letters* **16,** 4738–4745. doi:`10.1021/acs.nanolett.5b05107` (2016).

116. Jin, W. *et al.* Direct measurement of the thickness-dependent electronic band structure of MoS2 using angle-resolved photoemission spectroscopy. *Physical Review Letters* **111,** 106801. doi:`10.1103/PhysRevLett.111.106801` (2013).

117. Hamer, M. J. *et al.* Indirect to direct gap crossover in two-dimensional InSe revealed by angle-resolved photoemission spectroscopy. *ACS Nano* **13,** 2136–2142. doi:`10.1021/acsnano.8b08726` (2019).

118. Coy Diaz, H. *et al.* Direct observation of interlayer hybridization and Dirac relativistic carriers in graphene/MoS2 van der Waals heterostructures. *Nano Letters* **15,** 1135–1140. doi:`10.1021/nl504167y` (2015).

119. Wilson, N. R. *et al.* Determination of band offsets, hybridization, and exciton binding in 2D semiconductor heterostructures. *Science Advances* **3,** e1601832. doi:`10.1126/sciadv.1601832` (2017).

120. Wang, E. *et al.* Gaps induced by inversion symmetry breaking and second-generation Dirac cones in graphene/hexagonal boron nitride. *Nature Physics* **12,** 1111–1115. doi:`10.1038/nphys3856` (2016).

121. Ulstrup, S. *et al.* Direct observation of minibands in a twisted graphene/WS2 bilayer. *Science Sdvances* **6,** eaay6104. doi:`10.1126/sciadv.aay6104` (2020).

122. Stansbury, C. H. *et al.* Visualizing electron localization of WS2/WSe2 moiré superlattices in momentum space. *Science Advances* **7,** eabf4387. doi:`10.1126/sciadv.abf4387` (2021).

123. Jones, A. J. H. *et al.* Visualizing band structure hybridization and superlattice effects in twisted MoS2/WS2 heterobilayers. *2D Materials* **9,** 015032. doi:`10.1088/2053-1583/ac3feb` (2021).

124. Peng, H. *et al.* Substrate doping effect and unusually large angle van Hove singularity evolution in twisted bi-and multilayer graphene. *Advanced Materials* **29,** 1606741. doi:`10.1002/adma.201606741` (2017).

125. Thompson, J. J. P. *et al.* Determination of interatomic coupling between two-dimensional crystals using angle-resolved photoemission spectroscopy. *Nature Communications* **11,** 3582. doi:`10.1038/s41467-020-17412-0` (2020).

126. Iimori, T. *et al.* Electronic structure of 3°-twisted bilayer graphene on 4H-SiC (0001). *Physical Review Materials* **5,** L051001. doi:`10.1103/PhysRevMaterials.5.L051001` (2021).

127. Lisi, S. *et al.* Observation of flat bands in twisted bilayer graphene. *Nature Physics* **17,** 189–193. doi:`10.1038/s41567-020-01041-x` (2021).

128. Utama, M. I. B. *et al.* Visualization of the flat electronic band in twisted bilayer graphene near the magic angle twist. *Nature Physics* **17,** 184–188. doi:`10.1038/s41567-020-0974-x` (2021).

129. Zhang, Y. *et al.* Direct observation of the transition from indirect to direct bandgap in atomically thin epitaxial MoSe2. *Nature Nanotechnology* **9,** 111–115. doi:`10.1038/nnano.2013.277` (2014).

130. Riley, J. M. *et al.* Negative electronic compressibility and tunable spin splitting in WSe2. *Nature Nanotechnology* **10,** 1043–1047. doi:`10.1038/nnano.2015.217` (2015).

131. Zhang, Y. *et al.* Electronic structure, surface doping, and optical response in epitaxial WSe2 thin films. *Nano Letters* **16,** 2485–2491. doi:`10.1021/acs.nanolett.6b00059` (2016).

132. Nguyen, P. V. *et al.* Visualizing electrostatic gating effects in two-dimensional heterostructures. *Nature* **572,** 220–223. doi:`10.1038/s41586-019-1402-1` (2019).

133. Joucken, F. *et al.* Visualizing the effect of an electrostatic gate with angle-resolved photoemission spectroscopy. *Nano Letters* **19,** 2682–2687. doi:`10.1021/acs.nanolett.9b00649` (2019).

134. Jones, A. J. *et al.* Observation of electrically tunable van Hove singularities in twisted bilayer graphene from NanoARPES. *Advanced Materials* **32,** 2001656. doi:`10.1002/adma.202001656` (2020).

135. Xu, X. *et al.* Signature for non-Stoner ferromagnetism in the van der Waals ferromagnet Fe3GeTe2. *Physical Review B* **101,** 201104. doi:`10.1103/PhysRevB.101.201104` (2020).

136. De Vita, A. *et al.* Influence of orbital character on the ground state electronic properties in the van der Waals transition metal iodides VI3 and CrI3. *Nano Letters* **22,** 7034–7041. doi:`10.1021/acs.nanolett.2c01922` (2022).

137. Niu, W. *et al.* Probing the atomic-scale ferromagnetism in van der Waals magnet CrSiTe3. *Applied Physics Letters* **119,** 172402. doi:`10.1063/5.0069885` (2021).

138. Hu, C. *et al.* A van der Waals antiferromagnetic topological insulator with weak interlayer magnetic coupling. *Nature Communications* **11,** 97. doi:`10.1038/s41467-019-13814-x` (2020).

139. Mazzola, F. *et al.* Observation of Termination-Dependent Topological Connectivity in a Magnetic Weyl Kagome Lattice. *Nano Letters* **23,** 8035–8042. doi:`10.1021/acs.nanolett.3c02022` (2023).

140. Damascelli, A. Probing the electronic structure of complex systems by ARPES. *Physica Scripta* **2004,** 61. doi:`10.1238/Physica.Topical.109a00061` (2004).

141. Hüfner, S. *Photoelectron Spectroscopy: Principles and Applications* doi:`10.1007/978-3-662-09280-4` (Springer, 2003).

142. Moser, S. An experimentalist's guide to the matrix element in angle resolved photoemission. *Journal of Electron Spectroscopy and Related Phenomena* **214,** 29–52. doi:`10.1016/j.elspec.2016.11.007` (2017).

143. Wadati, H. *et al.* Angle-resolved photoemission spectroscopy of perovskite-type transition-metal oxides and their analyses using tight-binding band structure. *Phase Transitions* **79,** 617–635. doi:`10.1080/01411590600826672` (2006).

144. Mahan, G. D. Theory of photoemission in simple metals. *Physical Review B* **2,** 4334–4350. doi:`10.1103/PhysRevB.2.4334` (1970).

145. Pendry, J. B. Theory of photoemission. *Surface Science* **57,** 679–705. doi:`10.1016/0039-6028(76)90355-1` (1976).

146. Feibelman, P. J. & Eastman, D. E. Photoemission spectroscopy–Correspondence between quantum theory and experimental phenomenology. *Physical Review B* **10,** 4932–4947. doi:`10.1103/PhysRevB.10.4932` (1974).

147. Gadzuk, J. W. & Šunjić, M. Excitation energy dependence of core-level x-ray-photoemission-spectra line shapes in metals. *Physical Review B* **12,** 524–530. doi:`10.1103/PhysRevB.12.524` (1975).

148. Damascelli, A., Hussain, Z. & Shen, Z.-X. Angle-resolved photoemission studies of the cuprate superconductors. *Reviews of Modern Physics* **75,** 473–541. doi:`10.1103/RevModPhys.75.473` (2003).

149. Bansil, A. & Lindroos, M. Importance of matrix elements in the ARPES spectra of BISCO. *Physical Review Letters* **83,** 5154–5157. doi:`10.1103/PhysRevLett.83.5154` (1999).

150. Seah, M. P. l. & Dench, W. A. Quantitative electron spectroscopy of surfaces: A standard data base for electron inelastic mean free paths in solids. *Surface and Interface Analysis* **1,** 2–11. doi:`10.1002/sia.740010103` (1979).

151. Suga, S. & Sekiyama, A. *Photoelectron Spectroscopy: Bulk and Surface Electronic Structures* doi:`10.1007/978-3-642-37530-9` (Springer, 2014).

152. Balerna, A. & Mobilio, S. in *Synchrotron Radiation: Basics, Methods and Applications* 3–28 (Springer, 2015). doi:`10.1007/978-3-642-55315-8_1`.

153. Margaritondo, G. in *Synchrotron Radiation: Basics, Methods and Applications* 29–63 (Springer, 2015). doi:`10.1007/978-3-642-55315-8_2`.

154. Wang, H. *et al.* Complete polarization analysis of an APPLE II undulator using a soft X-ray polarimeter. *Journal of Synchrotron Radiation* **19,** 944–948. doi:`10.1107/S0909049512034851` (2012).

155. Hoesch, M. *et al.* A facility for the analysis of the electronic structures of solids and their surfaces by synchrotron radiation photoelectron spectroscopy. *Review of Scientific Instruments* **88,** 013106. doi:`10.1063/1.4973562` (2017).

156. Rösner, B., Dudin, P., Bosgra, J., Hoesch, M. & David, C. Zone plates for angle-resolved photoelectron spectroscopy providing sub-micrometre resolution in the extreme ultraviolet regime. *Journal of Synchrotron Radiation* **26,** 467–472. doi:`10.1107/S1600577519000869` (2019).

157. Koch, R. J. *et al.* Nano focusing of soft X-rays by a new capillary mirror optic. *Synchrotron Radiation News* **31,** 50–52. doi:`10.1080/08940886.2018.1483660` (2018).

158. Avila, J. & Asensio, M. C. First NanoARPES user facility available at SOLEIL: an innovative and powerful tool for studying advanced materials. *Synchrotron Radiation News* **27,** 24–30. doi:`10.1080/08940886.2014.889549` (2014).

159. Pizzocchero, F. *et al.* The hot pick-up technique for batch assembly of van der Waals heterostructures. *Nature Communications* **7,** 11894. doi:`10.1038/ncomms11894` (2016).

160. Kim, K. *et al.* van der Waals heterostructures with high accuracy rotational alignment. *Nano Letters* **16,** 1989–1995. doi:`10.1021/acs.nanolett.5b05263` (2016).

161. Desai, S. B. *et al.* Gold-mediated exfoliation of ultralarge optoelectronically-perfect monolayers. *Advanced Materials* **28,** 4053–4058. doi:`10.1002/adma.201506171` (2016).

162. Huang, Y. *et al.* Universal mechanical exfoliation of large-area 2D crystals. *Nature Communications* **11,** 2453. doi:`10.1038/s41467-020-16266-w` (2020).

163. Velicky, M. *et al.* Mechanism of gold-assisted exfoliation of centimeter-sized transition-metal dichalcogenide monolayers. *ACS Nano* **12,** 10463–10472. doi:`10.1021/acsnano.8b06101` (2018).

164. Vogel, N., Zieleniecki, J. & Köper, I. As flat as it gets: ultrasmooth surfaces from template-stripping procedures. *Nanoscale* **4,** 3820–3832. doi:`10.1039/c2nr30434a` (2012).

165. Hegner, M., Wagner, P. & Semenza, G. Ultralarge atomically flat template-stripped Au surfaces for scanning probe microscopy. *Surface Science* **291,** 39–46. doi:`10.1016/0039-6028(93)91474-4` (1993).

166. Wagner, P., Hegner, M., Guentherodt, H.-J. & Semenza, G. Formation and in situ modification of monolayers chemisorbed on ultraflat template-stripped gold surfaces. *Langmuir* **11,** 3867–3875. doi:`10.1021/la00010a043` (1995).

167. Heyl, M. *et al.* Thermally Activated Gold-Mediated Transition Metal Dichalcogenide Exfoliation and a Unique Gold-Mediated Transfer. *Physica Status Solidi (RRL)–Rapid Research Letters* **14,** 2000408. doi:`10.1002/pssr.202000408` (2020).

168. Heyl, M. *et al.* Low Temperature Heating of Silver-Mediated Exfoliation of MoS2. *Advanced Materials Interfaces* **9,** 2200362. doi:`10.1002/admi.202200362` (2022).

169. Wang, L. *et al.* Correlated electronic phases in twisted bilayer transition metal dichalcogenides. *Nature Materials* **19,** 861–866. doi:`10.1038/s41563-020-0708-6` (2020).

170. Barman, P. K. *et al.* Twist-dependent tuning of excitonic emissions in bilayer WSe2. *ACS Omega* **7,** 6412–6418. doi:`10.1021/acsomega.1c07219` (2022).

171. Alexeev, E. M. *et al.* Resonantly hybridized excitons in moiré superlattices in van der Waals heterostructures. *Nature* **567,** 81–86. doi:`10.1038/s41586-019-0986-9` (2019).

172. Lau, C. N., Bockrath, M. W., Mak, K. F. & Zhang, F. Reproducibility in the fabrication and physics of moiré materials. *Nature* **602,** 41–50. doi:`10.1038/s41586-021-04173-z` (2022).

173. Voit, J. *et al.* Electronic structure of solids with competing periodic potentials. *Science* **290,** 501–503. doi:`10.1126/science.290.5491.501` (2000).

174. Partoens, B. & Peeters, F. M. Normal and Dirac fermions in graphene multilayers: Tight-binding description of the electronic structure. *Physical Review B* **75,** 193402. doi:`10.1103/PhysRevB.75.193402` (2007).

175. Berciaud, S., Potemski, M. & Faugeras, C. Probing electronic excitations in mono-to pentalayer graphene by micro magneto-Raman spectroscopy. *Nano Letters* **14,** 4548–4553. doi:`10.1021/nl501578m` (2014).

176. Lui, C. H. *et al.* Imaging stacking order in few-layer graphene. *Nano Letters* **11,** 164–169. doi:`10.1021/nl1032827` (2011).

177. Wirth, K. G. *et al.* Experimental observation of ABCB stacked tetralayer graphene. *ACS Nano* **16,** 16617–16623. doi:`10.1021/acsnano.2c06053` (2022).

178. García-Ruiz, A., Slizovskiy, S., Mucha-Kruczynski, M. & Fal'ko, V. I. Spectroscopic signatures of electronic excitations in Raman scattering in thin films of rhombohedral graphite. *Nano Letters* **19,** 6152–6156. doi:`10.1021/acs.nanolett.9b02196` (2019).

179. McEllistrim, A., Garcia-Ruiz, A., Goodwin, Z. A. H. & Fal'ko, V. I. Spectroscopic signatures of tetralayer graphene polytypes. *Physical Review B* **107,** 155147. doi:`10.1103/PhysRevB.107.155147` (2023).

180. Yin, J. *et al.* Dimensional reduction, quantum Hall effect and layer parity in graphite films. *Nature Physics* **15,** 437–442. doi:`10.1038/s41567-019-0427-6` (2019).

181. Park, C.-H., Giustino, F., Spataru, C. D., Cohen, M. L. & Louie, S. G. Angle-resolved photoemission spectra of graphene from first-principles calculations. *Nano Letters* **9,** 4234–4239. doi:`10.1021/nl902448v` (2009).

182. Siegel, D. A., Regan, W., Fedorov, A. V., Zettl, A. & Lanzara, A. Charge-carrier screening in single-layer graphene. *Physical Review Letters* **110,** 146802. doi:`10.1103/PhysRevLett.110.146802` (2013).

183. Muzzio, R. *et al.* Momentum-resolved view of highly tunable many-body effects in a graphene/hBN field-effect device. *Physical Review B* **101,** 201409. doi:`10.1103/PhysRevB.101.201409` (2020).

184. González, J., Guinea, F. & Vozmediano, M. A. H. Non-Fermi liquid behavior of electrons in the half-filled honeycomb lattice (A renormalization group approach). *Nuclear Physics B* **424,** 595–618. doi:`10.1016/0550-3213(94)90410-3` (1994).

185. Hwang, C. *et al.* Fermi velocity engineering in graphene by substrate modification. *Scientific reports* **2,** 590. doi:`10.1038/srep00590` (2012).

186. Evtushinsky, D. V. *et al.* Unadulterated spectral function of low-energy quasiparticles in Bi2Sr2CaCu2O8+δ. *Physical Review B* **74,** 172509. doi:`10.1103/PhysRevB.74.172509` (2006).

187. González, J., Guinea, F. & Vozmediano, M. A. H. Unconventional quasiparticle lifetime in graphite. *Physical Review Letters* **77,** 3589–3592. doi:`10.1103/PhysRevLett.110.146802` (1996).

188. Kuemmeth, F. & Rashba, E. I. Giant spin rotation under quasiparticle-photoelectron conversion: Joint effect of sublattice interference and spin-orbit coupling. *Physical Review B* **80,** 241409. doi:`10.1103/PhysRevB.80.241409` (2009).

189. Shirley, E. L., Terminello, L. J., Santoni, A. & Himpsel, F. J. Brillouin-zone-selection effects in graphite photoelectron angular distributions. *Physical Review B* **51,** 13614. doi:`10.1103/PhysRevB.51.13614` (1995).

190. Gierz, I., Henk, J., Höchst, H., Ast, C. R. & Kern, K. Illuminating the dark corridor in graphene: Polarization dependence of angle-resolved photoemission spectroscopy on graphene. *Physical Review B* **83,** 121408. doi:`10.1103/PhysRevB.83.121408` (2011).

191. Strocov, V. N. Intrinsic accuracy in 3-dimensional photoemission band mapping. *Journal of Electron Spectroscopy and Related Phenomena* **130,** 65–78. doi:`10.1016/S0368-2048(03)00054-9` (2003).

192. Polley, C. M. *et al.* Origin of the π-band replicas in the electronic structure of graphene grown on 4H-SiC(0001). *Physical Review B* **99,** 115404. doi:`10.1103/PhysRevB.99.115404` (2019).

193. Garcia-Ruiz, A., Deng, H.-Y., Enaldiev, V. V. & Fal'ko, V. I. Full Slonczewski-Weiss-McClure parametrization of few-layer twistronic graphene. *Physical Review B* **104,** 085402. doi:`10.1103/PhysRevB.104.085402` (2021).

194. Zhu, J., Shi, J. & MacDonald, A. H. Theory of angle-resolved photoemission spectroscopy in graphene-based moiré superlattices. *Physical Review B* **103,** 235146. doi:`10.1103/PhysRevB.103.235146` (2021).

195. Hamer, M. J. *et al.* Moiré Superlattice Effects and Band Structure Evolution in Near-30-Degree Twisted Bilayer Graphene. *ACS Nano* **16,** 1954–1962. doi:`10.1021/acsnano.1c06439` (2022).

196. Majchrzak, P. *et al.* In Operando Angle-Resolved Photoemission Spectroscopy with Nanoscale Spatial Resolution: Spatial Mapping of the Electronic Structure of Twisted Bilayer Graphene. *Small Science* **1,** 2000075. doi:`10.1002/smsc.202000075` (2021).

197. Ohta, T. *et al.* Evidence for interlayer coupling and moiré periodic potentials in twisted bilayer graphene. *Physical Review Letters* **109,** 186807. doi:`10.1103/PhysRevLett.109.186807` (2012).

198. Yu, K. *et al.* Gate tunable optical absorption and band structure of twisted bilayer graphene. *Physical Review B* **99,** 241405. doi:`10.1103/PhysRevB.99.241405` (2019).

199. Pierucci, D. *et al.* Band alignment and minigaps in monolayer MoS2-graphene van der Waals heterostructures. *Nano Letters* **16,** 4054–4061. doi:`10.1021/acs.nanolett.6b00609` (2016).

200. Graham, A. J. *et al.* Ghost anti-crossings caused by interlayer umklapp hybridization of bands in 2D heterostructures. *2D Materials* **8,** 015016. doi:`10.1088/2053-1583/abc13e` (2020).

201. Haddadi, F., Wu, Q., Kruchkov, A. J. & Yazyev, O. V. Moiré flat bands in twisted double bilayer graphene. *Nano Letters* **20,** 2410–2415. doi:`10.1021/acs.nanolett.9b05117` (2020).

202. Nam, N. N. T. & Koshino, M. Lattice relaxation and energy band modulation in twisted bilayer graphene. *Physical Review B* **96,** 075311. doi:`10.1103/PhysRevB.96.075311` (2017).

203. Zhang, K. & Tadmor, E. B. Structural and electron diffraction scaling of twisted graphene bilayers. *Journal of the Mechanics and Physics of Solids* **112,** 225–238. doi:`10.1016/j.jmps.2017.12.005` (2018).

204. Carr, S., Fang, S. & Kaxiras, E. Electronic-structure methods for twisted moiré layers. *Nature Reviews Materials* **5,** 748–763. doi:`10.1038/s41578-020-0214-0` (2020).

205. Lee, J. Y. *et al.* Theory of correlated insulating behaviour and spin-triplet superconductivity in twisted double bilayer graphene. *Nature Communications* **10,** 5333. doi:`10.1038/s41467-019-12981-1` (2019).

206. Slizovskiy, S. *et al.* Out-of-plane dielectric susceptibility of graphene in twistronic and Bernal bilayers. *Nano Letters* **21,** 6678–6683. doi:`10.1021/acs.nanolett.1c02211` (2021).

207. McCann, E. Asymmetry gap in the electronic band structure of bilayer graphene. *Physical Review B* **74,** 161403. doi:`10.1103/PhysRevB.74.161403` (2006).

208. Laturia, A., Van de Put, M. L. & Vandenberghe, W. G. Dielectric properties of hexagonal boron nitride and transition metal dichalcogenides: from monolayer to bulk. *NPJ 2D Materials and Applications* **2,** 6. doi:`10.1038/s41699-018-0050-x` (2018).

209. Akram, M. & Erten, O. Skyrmions in twisted van der Waals magnets. *Physical Review B* **103,** L140406. doi:`10.1103/PhysRevB.103.L140406` (2021).

210. Akram, M. *et al.* Moiré skyrmions and chiral magnetic phases in twisted CrX3 (X= I, Br, and Cl) bilayers. *Nano Letters* **21,** 6633–6639. doi:`10.1021/acs.nanolett.1c02096` (2021).

211. Hejazi, K., Luo, Z.-X. & Balents, L. Noncollinear phases in moiré magnets. *Proceedings of the National Academy of Sciences* **117,** 10721–10726. doi:`10.1073/pnas.2000347117` (2020).

212. Xu, Y. *et al.* Coexisting ferromagnetic–antiferromagnetic state in twisted bilayer CrI3. *Nature Nanotechnology* **17,** 143–147. doi:`10.1038/s41565-021-01014-y` (2022).

213. Xie, H. *et al.* Twist engineering of the two-dimensional magnetism in double bilayer chromium triiodide homostructures. *Nature Physics* **18,** 30–36. doi:`10.1038/s41567-021-01408-8` (2022).

214. Xie, H. *et al.* Evidence of non-collinear spin texture in magnetic moiré superlattices. *Nature Physics* **19,** 1150–1155. doi:`10.1038/s41567-023-02061-z` (2023).

215. Chittari, B. L. *et al.* Electronic and magnetic properties of single-layer MPX3 metal phosphorous trichalcogenides. *Physical Review B* **94,** 184428. doi:`10.1103/PhysRevB.94.184428` (2016).

216. Cardona, M. & Ley, L. *Photoemission in Solids I: General Principles* doi:`10.1007/3-540-08685-4` (Springer, 1978).

217. Dendzik, M. *et al.* Substrate-induced semiconductor-to-metal transition in monolayer WS2. *Physical Review B* **96,** 235440. doi:`10.1103/PhysRevB.96.235440` (2017).

218. Bianchi, M. *et al.* Charge transfer-induced Lifshitz transition and magnetic symmetry breaking in ultrathin CrSBr crystals. doi:`10.48550/arXiv.2307.12675` (2023).

219. Mazzola, F. *et al.* Strong electron-phonon coupling in the σ band of graphene. *Physical Review B* **95,** 075430. doi:`10.1103/PhysRevB.95.075430` (2017).

220. Tomić, M., Jeschke, H. O. & Valentí, R. Unfolding of electronic structure through induced representations of space groups: Application to Fe-based superconductors. *Physical Review B* **90,** 195121. doi:`10.1103/PhysRevB.90.195121` (2014).

221. Klein, J. *et al.* Sensing the local magnetic environment through optically active defects in a layered magnetic semiconductor. *ACS Nano* **17,** 288–299. doi:`10.1021/acsnano.2c07655` (2022).

222. Estyunin, D. A. *et al.* Signatures of temperature driven antiferromagnetic transition in the electronic structure of topological insulator MnBi2Te4. *APL Materials* **8,** 021105. doi:`10.1063/1.5142846` (2020).

223. Tian, Y., Gray, M. J., Ji, H., Cava, R. J. & Burch, K. S. Magneto-elastic coupling in a potential ferromagnetic 2D atomic crystal. *2D Materials* **3,** 025035. doi:`10.1088/2053-1583/3/2/025035` (2016).

224. Xu, X. *et al.* Strong Spin-Phonon Coupling in Two-Dimensional Magnetic Semiconductor CrSBr. *The Journal of Physical Chemistry C* **126,** 10574–10583. doi:`10.1021/acs.jpcc.2c02742` (2022).

225. Jiang, Z. *et al.* Revealing flat bands and hybridization gaps in a twisted bilayer graphene device with microARPES. *2D Materials* **10,** 045027. doi:`10.1088/2053-1583/acf775` (2023).

226. Hao, Z. *et al.* Electric field–tunable superconductivity in alternating-twist magic-angle trilayer graphene. *Science* **371,** 1133–1138. doi:`10.1126/science.abg0399` (2021).

227. Park, J. M. *et al.* Robust superconductivity in magic-angle multilayer graphene family. *Nature Materials* **21,** 877–883. doi:`10.1038/s41563-022-01287-1` (2022).

228. Uri, A. *et al.* Superconductivity and strong interactions in a tunable moiré quasicrystal. *Nature* **620,** 762–767. doi:`10.1038/s41586-023-06294-z` (2023).

229. Graham, A. J. *et al.* Revealing the conduction band and pseudovector potential in 2D moiré semiconductors. doi:`10.48550/arXiv.2309.10964` (2023).

230. Wang, W. *et al.* Ultra-clean assembly of van der Waals heterostructures. doi:`10.48550/arXiv.2308.13484` (2023).